ISSN : 0025-0422

JOURNAL OF THE MAHARAJA SAYAJIRAO UNIVERSITY OF BARODA: SCIENCE & TECHNOLOGY

VOL. 57
2023

सत्यं शिवं सुन्दरम्
Estd. 1949
Accredited Grade A+ by NAAC

Published by
The Maharaja Sayajirao University of Baroda
Vadodara, Gujarat, India

JOURNAL
OF
THE MAHARAJA SAYAJIRAO UNIVERSITY OF BARODA:
SCIENCE & TECHNOLOGY

Editorial Board

JOURNAL
OF
THE MAHARAJA SAYAJIRAO UNIVERSITY OF BARODA: SCIENCE & TECHNOLOGY

VOL. 57
2023

EDITOR
Prof. P. K. Jha

Accredited Grade A+ by NAAC

Published by
The Maharaja Sayajirao University of Baroda
Vadodara, Gujarat, India

ISSN : 0025-0422

Printed by Shri Jatin H. Somani, Manager, The Maharaja Sayajirao University of Baroda Press (Sadhana Press), Near Palace Gate, Palace Road, Vadodara, and Edited by **Prof. P. K. Jha,** Editor (Science & Technology) at the Maharaja Sayajirao University of Baroda, Vadodara - 390 002, (India), 2023.

CONTENTS

Journal of the Maharaja Sayajirao University of Baroda: Science & Technology
Vol. 57, 2023, pp. 1-5

Fatigue Crack Growth Analysis in Compact Tension Specimen of Aluminium Alloy 6061-T6 and 7075-T6

Krishna Nair and J. D. Rathod

Applied Mechanics Department, Faculty of Technology and Engineering, The Maharaja Sayajirao University of Baroda, Vadodara – 390001 kgnair-appmech@msubaroda.ac.in jdrathod-appmech@msubaroda.ac.in

Aluminium has become ideal for lowering cost of aircraft manufacturing while upholding stringent specifications like excellent corrosion resistance, high specific strength and good machinability characteristics. Finite element analysis technique using CASCA mesh generation and FRANC2D software is used to simulate compact tension test specimen to reveal the fracture properties of aluminium alloy 6061-T6 and 7075-T6 with their fatigue behaviour. Crack growth rate was determined from Paris Law which is considered to be one of the significant methods for crack growth analysis. Results are useful for estimating the fatigue life of the material for a given crack length during its service life. Results show that the fatigue life of Al 6061-T6 is higher than Al 7075-T6 for 10 mm crack length.

Keywords: Aluminium Alloy, CASCA, FRANC2D, Fatigue, Crack growth rate.

Introduction

Aluminium has been used in the aerospace industry ever since the Wright brothers built their first plane. Although, original plane structures were made of wood, engine crank cases were formed from aluminium. Civilians were encouraged to donate scrap aluminium to the war effort during World War II. Today, like many industries, aerospace makes wide use of aluminium manufacturing.

Aluminium alloy 6061-T6 (Al 6061-T6) has good mechanical properties and is easily welded. Al 6061-T6 finds various usage as a structural material. It is a common alloy in general and aerospace applications in particular for wing and fuselage structures. According to empirical observations, majority of failures in practice can be attributed to fatigue. Scientist and researchers have found that a torn fracture in the Al 6061-T6 material takes place due to fatigue only. Evaluation of the fatigue behaviour of Al 6061-T6 helps to predict the life of the component through fatigue crack growth rate graph [1]. Al 6061-T6 is considered as potential material for automobile and aerospace sectors because of its high strength with reduced weight and high crack arrest capabilities.

Aluminium Alloy 7075-T6 (Al 7075-T6), on the other hand, is one of the strongest aluminium alloys available with higher cost when strength and toughness are crucial [2]. Zinc is the main alloying element with strength similar to that of many types of steel. It has good machinability and fatigue strength properties. It was originally used in the Mitsubishi A6M Zero fighter planes during World War II, and is still used in aviation. Hence, this material has been widely used in important components subjected to mechanical fatigue loading conditions which makes it necessary to study its fatigue behaviour [3].

Al 6061-T6 has less zinc than the Al 7075-T6 materials, which provides superior welding abilities and workability over to Al 6061-T6. However, it is to be noted that Al 6061 doesn't possess high strength and stress resistance as Al 7075 offers. C. M. Hudson and J. T. Scardina (1967), carried out axial load v/s fatigue crack propagation tests on 12 inch (307 mm) wide sheet specimens made of Al 7075-T6 to study the effects of stress ratio on fatigue crack growth. The fatigue crack growth was analysed using Paris stress intensity factor [4]. M. Matur (2015) obtained stress intensity factor (SIF) values by the numerical simulation for the single edge notch bend (SENB) specimen which showed a good agreement with the results obtained by photo elastic technique. Outcome of the study showed that the dependency of crack

*Corresponding author.
Email: mehta_kamlesh1@gtu.edu.in

propagation is on the stress intensity range [5].

S. Patel (2016) carried out fatigue analysis and crack propagation in a 52 kg standard rail section used for broad gauge tracks in Indian Railways under the axle load of 28.56 tonnes (maximum axle load for broad gauge) with the help of CASCA and FRANC2D. Results are useful for estimating the fatigue life of the rail and to estimate the length of the crack at the end of the life [6]. H. A. Ghulman (2017) studied the finite element model for compact tension specimen of thin sheets Al 6061-T6 of 1 mm and 1.6 mm thickness to measure energy release rate (GIC). Further, this work investigates the effect of sheet thickness on the fracture toughness which is very important and dominant fracture property [7].

In this paper a Fracture Mechanics based approach is adopted for the determination of the crack length v/s number of cycles using Paris' Law [8]. FRANC2D is adopted for the computational simulation of crack growth. The aim of study is to estimate the fatigue life and length of the crack at the end of the life for the Al 6061- T6 and 7075- T6. CASCA is used for the creating the meshes as a pre-processor for generating initial input files for FRANC2D in this work.

Materials and Methods

Details and Geometry of Compact Tension (CT) Specimen:

The specimen of dimension 67 mm x 69 mm x 9 mm is adopted as per American Society for Testing and Materials (ASTM) E 399 standard compact tension (CT) specimen [9]; its shape and dimensions are shown in Fig. 1. The FRANC2D is a finite element-based simulator for curvilinear crack propagation in planar (plane stress, plane strain, and axisymmetric) structures. CASCA here is used for creating the meshes and generating initial input files for FRANC2D.

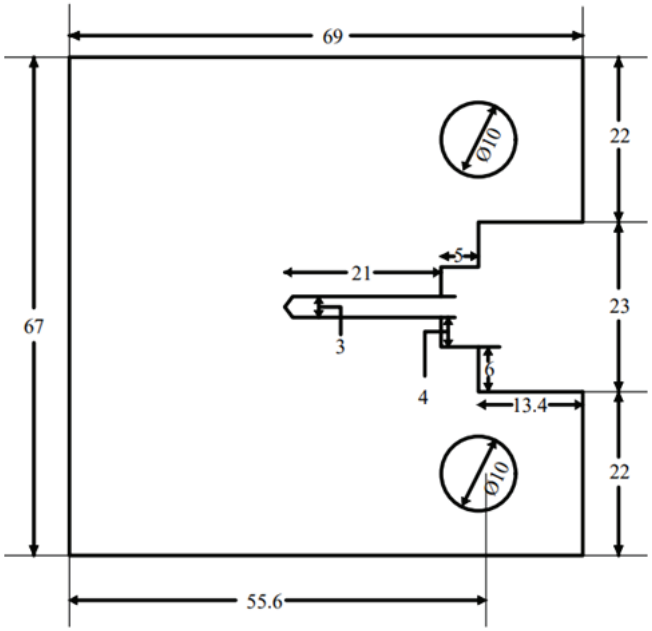

Fig. 1 Dimension of the model.

Table 1: Material Properties of Al 6061-T6 and Al 7075-T6.

Properties	Al 6061-T6	Al 7075-T6
Modulus of Elasticity	68.9 GPa	70-80 GPa
Poisson's Ratio	0.33	0.33
Density	2.7 g/cm^3	2.8 g/cm^3
Coefficient of Thermal Expansion	23.4 * 10^{-6} °C^{-1} 13.2 * 10^{-1} °F^{-1}	23.2 * 10^{-6} °C^{-1} 13.0 * 10^{-1} °F^{-1}
Thickness	9 mm	9 mm

Simulation Procedure

Experimental results show that the fatigue failure in aluminium alloys can occur beyond 10^7 and even at 10^9 cycles without any pre-notch in them and no endurance limit could be seen in the alloys until then [10]. Combination of CASCA and FRANC 2D was used to stimulate the fatigue life cycles of this specimen geometry and it was found to be 10^8 cycles. Hence, a mesh generating program CASCA, which is distributed with FRANC2D, is used to create the initial mesh configuration for simulations in the present study. Also, the same simulation procedure was conducted for compact tension specimen for SS316L steel model with initial crack for fatigue life analysis using Paris Law [11].

Tensile load is assumed to act uniformly on the specimen perpendicular to crack propagation. The chronological procedure for creating a mesh is as illustrated in the Figures 2-6. Outline is first created followed by the division of the sub regions within the problem boundary. Prior to assigning the type of elements to each of the sub regions, the boundaries for all the sub regions are divided into the required number of segments as shown in Fig. 2.

Fig. 3 shows one of the meshes used in the present study which comprises bilinear four-sided elements and the boundary conditions are specified by fixing lower half hole by FIX EDGE X option [13]. Fig. 4 shows the resulting mesh for the present simulation after applying the boundary conditions.

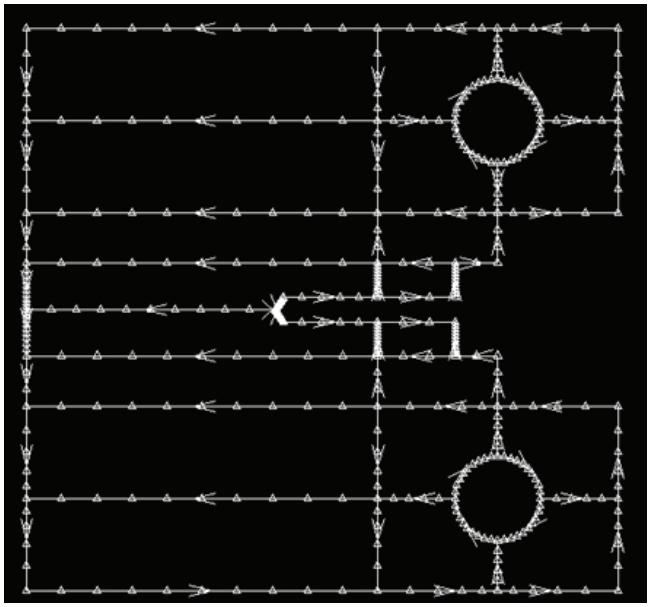

Fig. 2. Sub-regions divided into number of segments.

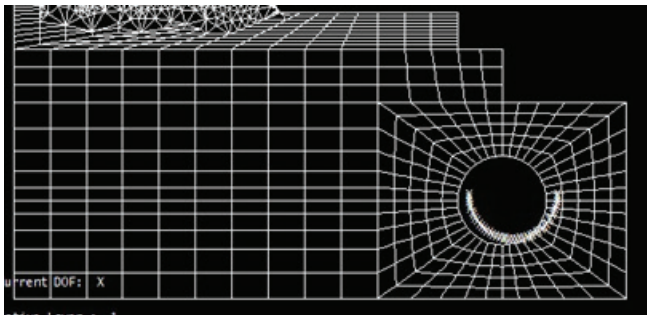

Fig. 3. Fixing of lower half of hole.

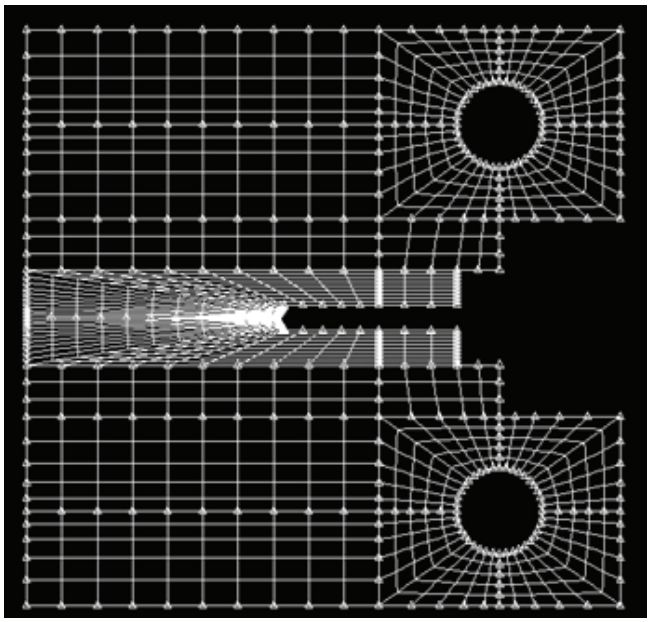

Fig. 4. Resulting mesh of present simulation.

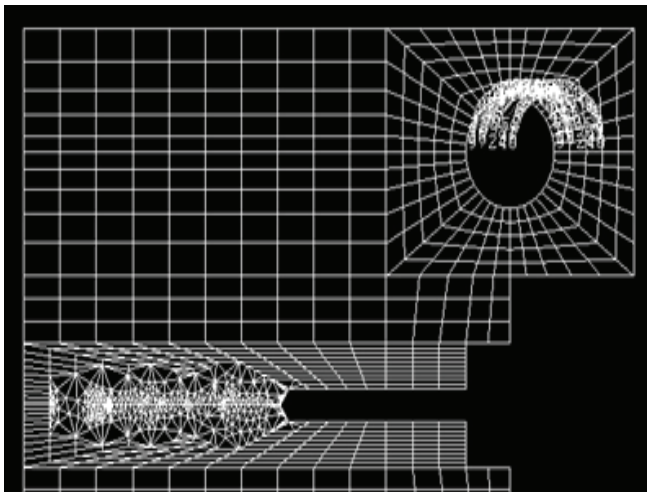

Fig. 5. – Load distribution on upper half of hole

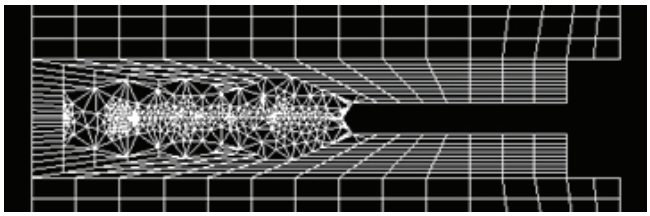

Fig. 6. – Crack propagation due to application of load

Modelling is done considering the pin as an axial load over a portion of the surface of hole. Upon different options of load distribution, pin loading can be the best modelled by a quadratic load distribution over one half of pin hole as shown in Fig. 5. Uniform distribution of total load is taken as 0.1 kN.

In order to simulate the crack growth, an initial non cohesive crack was placed at the notch tip, where it was predicted to have the critical tensile stress. Since, the location of crack is specified, the direction in which the crack would propagate can be predicted. Prior to performing the quasistatic crack propagation, it is necessary to specify the crack tip, after which the crack propagation due to fatigue loading can be performed using standard method. Fig. 6. shows the crack propagation after application of load. After finalizing the location, initial crack of length 1 mm was introduced at the location. The crack propagation simulation is carried up to crack length of 21 mm.

Results and Discussion

The computed test data, fatigue crack growth rate and stress intensity factor range for Al 6061- T6 and Al 7075-T6 are listed in Table 2 and 3 respectively. Paris constants are in agreement from published result

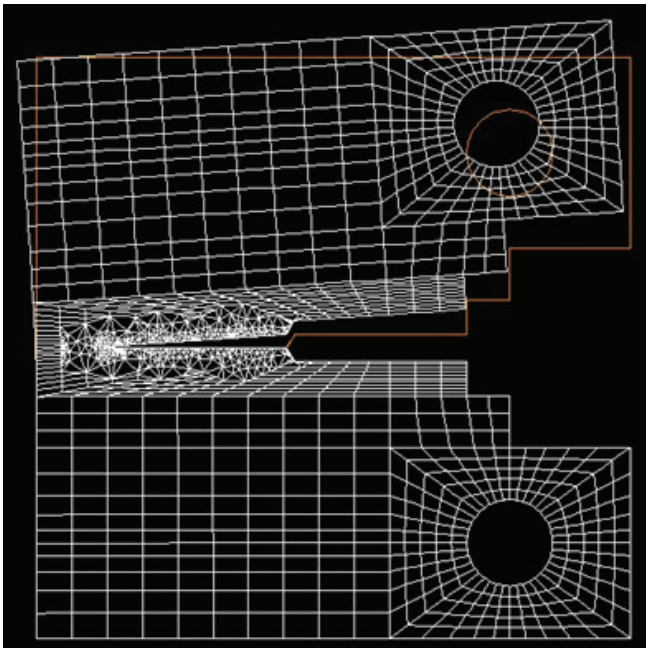

Fig. 7. Deformed mesh after crack propagation.

for used in numerical solution i.e., C = 7.88E-09, m = 3.97 for Al 6061-T6 [7] and C = 6.85E-08, m = 3.21 for Al 7075-T6 [4]. The deformed specimen as shown in Fig. 7 indicates that meshing becomes more degenerated with increase in crack growth in the material.

From the results, it has been observed that, fatigue crack growth behaviour depends mainly on threshold stress intensity factor ΔK and stress intensity factor K_I, respectively. Stress intensity range describes the fatigue damage behaviour of the material and maximum SIF indicates the crack tip widening under the applied load. At low ΔK values, crack propagation is extremely slow. Convince ably there is a threshold stress intensity value at ΔK_{th} below which there is no fatigue crack growth. At high stress intensities, crack growth rates are extremely high and little fatigue life is ensured. The crack growth rate accelerates as the maximum stress intensity factor approaches the fracture toughness of the material. At the crack length equal to 10 mm, ΔK value is found to be 2.23052 MPa $mm^{1/2}$ and 2.23064 MPa $mm^{1/2}$, respectively for Al 6061-T6 and Al 7075- T6 which could be considered to be the threshold value below which the stress

Table 2 Fatigue crack growth rate data for Al 6061-T6.

Crack Length	K_I	da (mm)	ΔK (MPa $mm^{1/2}$)	da/dN (mm/cycle)	dN	N (Cycle)
0	1219.947	0	0	0	0	0
1	1219.947	1	1.219946767	1.74E-08	5.76E+07	5.76E+07
2	1322.755	2	1.271350525	2.04E-08	4.89E+07	1.07E+08
3	1411.247	3	1.367000916	2.73E-08	3.67E+07	1.43E+08
4	1502.295	4	1.456771057	3.51E-08	2.85E+07	1.72E+08
5	1584.351	5	1.54332312	4.41E-08	2.27E+07	1.94E+08
6	1714.379	6	1.649365356	5.74E-08	1.74E+07	2.12E+08
7	1832.448	7	1.773413818	7.66E-08	1.31E+07	2.25E+08
8	1982.311	8	1.907379883	1.02E-07	9.78E+06	2.35E+08
9	2137.019	9	2.059664978	1.39E-07	7.21E+06	2.42E+08
10	2324.022	10	2.230520386	1.90E-07	5.25E+06	2.47E+08
11	2535.145	11	2.429583741	2.67E-07	3.74E+06	2.51E+08
12	2778.062	12	2.656603638	3.81E-07	2.62E+06	2.53E+08
13	3064.875	13	2.921468628	5.56E-07	1.80E+06	2.55E+08
14	3389.671	14	3.227273071	8.25E-07	1.21E+06	2.56E+08
15	3785.964	15	3.587817261	1.26E-06	7.96E+05	2.57E+08
16	4219.303	16	4.002633179	1.94E-06	5.15E+05	2.58E+08
17	4834.991	17	4.527146729	3.16E-06	3.16E+05	2.58E+08
18	5538.96	18	5.186975342	5.43E-06	1.84E+05	2.58E+08
19	6460.406	19	5.999682862	9.68E-06	1.03E+05	2.58E+08
20	7438.938	20	6.949671875	1.73E-05	5.77E+04	2.58E+08
21	9140.575	21	8.289756592	3.49E-05	2.86E+04	2.58E+08

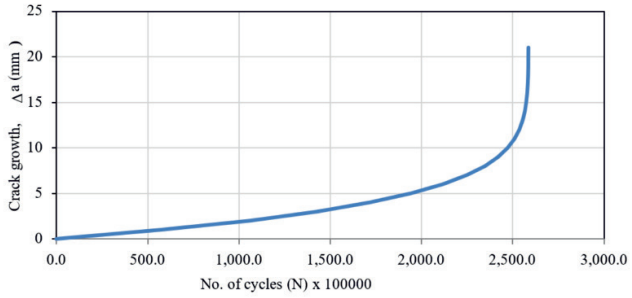

Fig. 8. Crack growth v/s number of cycles for Al 6061-T6.

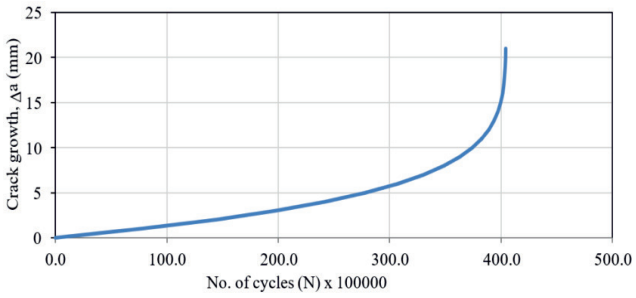

Fig. 9. Crack growth v/s number of cycles for Al 7075-T6.

intensity factor and crack growth rate are extremely slow and after which there is a rapid increase in the crack growth. Hence, at 10 mm length of crack for Al 6061-T6 and Al 7075- T6 fatigue life cycles could be 25×10^7 cycles and 37.4×10^7 cycles, respectively as indicated in Fig. 8 and Fig. 9. Al 6061-T6 has higher cyclic hardening property than Al 7075-T6 under fatigue loading and the same fact is supported by strain-controlled experiments performed on the material [1]. In case of Al 7075-T6, it has been observed that the crack initiation and propagation can be easily induced making it relatively faster which makes it less stable and this is because it has more voids coalescence compared to Al 6061-T6 during fatigue loading [3].

Conclusion

Fracture mechanics principles helps to predict fatigue life of the material for various crack length present into it. It also gives permissible crack length into material up to which design fatigue life is accepted. CASCA mesh model implemented into FRANC2D package is very useful tool to achieve the simulation of fracture and fatigue crack growth. The obtained results reveal that Al 6061- T6 and Al 7075- T6 can be stressed up to 10 mm crack length for acceptable design life. The fatigue life of Al 6061-T6 is higher than Al 7075-T6 alloy at the threshold crack length of 10 mm.

Table 3 Fatigue crack growth rate data for Al 7075-T6.

Crack Length	K_I	da (mm)	ΔK (MPa $mm^{1/2}$)	da/dN (mm/cycle)	dN	N (Cycle)
0	1219.811	0	0	0	0	0
1	1219.811	1	1.219811401	1.30E-07	7.71E+06	7.71E+06
2	1322.748	2	1.271279663	1.48E-07	6.76E+06	1.45E+07
3	1411.253	3	1.367000489	1.87E-07	5.35E+06	1.98E+07
4	1502.245	4	1.456749268	2.29E-07	4.36E+06	2.42E+07
5	1584.593	5	1.543419128	2.76E-07	3.62E+06	2.78E+07
6	1714.427	6	1.649510071	3.42E-07	2.93E+06	3.07E+07
7	1832.178	7	1.773302857	4.31E-07	2.32E+06	3.31E+07
8	1981.291	8	1.906734558	5.44E-07	1.84E+06	3.49E+07
9	2138.496	9	2.059893555	6.97E-07	1.44E+06	3.63E+07
10	2322.796	10	2.230646241	9.00E-07	1.11E+06	3.74E+07
11	2540.598	11	2.431697144	1.19E-06	8.42E+05	3.83E+07
12	2764.842	12	2.652720215	1.57E-06	6.37E+05	3.89E+07
13	3072.458	13	2.918650391	2.13E-06	4.69E+05	3.94E+07
14	3344.847	14	3.20865271	2.89E-06	3.46E+05	3.97E+07
15	3787.413	15	3.566130005	4.06E-06	2.46E+05	4.00E+07
16	4238.593	16	4.013003174	5.93E-06	1.69E+05	4.02E+07
17	4802.812	17	4.520702637	8.69E-06	1.15E+05	4.03E+07
18	5567.006	18	5.18490918	1.35E-05	7.41E+04	4.03E+07
19	6464.084	19	6.015545411	2.17E-05	4.60E+04	4.04E+07
20	7420.89	20	6.942487305	3.44E-05	2.90E+04	4.04E+07
21	9134.146	21	8.277517823	6.06E-05	1.65E+04	4.04E+07

References

1 B. Mohammad, Zulhani, H. Supriadi, Low cycle fatigue properties of extruded 6061-T6 aluminum alloy, *J. Phy. Con*. 1198(3), 032002*,* 2019.

2 S. C. Forth, C. W. Wright, W. M. Johnston Jr., 7075-T6 and 2024-T351 Aluminium alloy fatigue crack growth rate data, *NASA/TM*, 213907, 2005.

3 F. Lei, D. Heng, L. Hui, L. Lin, Low-cycle fatigue behaviour of 7075-T6 aluminium alloy at different strain amplitudes, *Mat. Exp.,* 10(6), 2020.

4 C. M. Hudson and J. T. Scardina, Effect of stress ratio on fatigue-crack growth in 7075-T6 aluminium-alloy sheet, *Nat. Symp. Fract. Mech.,* 1967.

5 M. Matur, V. Krishnan, P. Dinesh, Study on fatigue crack growth behavior of aluminium alloy in the presence of notch: an FEA approach, *IOSR J. Mech. Civil Engg.,* 12(5), 68-74, 2015.

6 S. Patel, B. Thakkar, Fatigue analysis on steel rail section, *Int. J. Adv. Res. Sci. and Engg.,* 5(4), 2016.

7 Hamza A. Ghulman, Ductile fracture simulation of aluminium 6061-T6 thin sheet, *Int. J. Sci. Engg. Res.*, 8(5), 2017.

8 N. Pungo, M. Ciavarella, P. Cornetti, A. Carpinteri, A generalized paris' law for fatigue crack growth, *J. Mech. Phy. Sol.*, 54, 1333, 2005.

9 Y. Mohammed, K. Mohamed, A. Hashem, Finite element computational approach of fracture toughness in composite compact-tension specimen, *Int. J. Mech. Mecha. Engg.*, 12(4), 57, 2010.

10 Q. Y. Wang, N. Kawagoishi, Q. Che, Fatigue and fracture behaviour of structural Al-alloys up to very long-life regimes, *Int. J. Fati*., 28, 1572, 2006.

11 Y. O. Busari, A. Ariri1, Y. H. P. Manurung, Prediction of Crack Propagation Rate and Stress Intensity Factor of Fatigue and Welded Specimen with a Two-Dimensional Finite Element Method, *IOP Conf. Sr.: Mat. Sci. Engg.,* 012008, 834, 2020.

12 Cornell Fracture Group, "FRANC2D; A two-dimensional crack propagation simulator", Tutorial and User's guide*,* Version 2.7*,* 1995.

13 [13] J. R. Mohanty, A. Joni, P. K. Ray, B. B. Verma, Determination of crack coefficients for a single edge- notch tension specimen using FRANC2D program, *Rec. Tr. Mecha., Nano. Rob.*, 2006.

Journal of the Maharaja Sayajirao University of Baroda: Science & Technology
Vol. 57, 2023, pp. 6-13

Neglected Tropical Crops in India: Modern Perspectives

Suman Singh[1] and Madhu Prakash Srivastava[2*]

[1]Central Institute of Medicinal and Aromatic Plants, Lucknow
[2]Department of Botany, Maharishi University of Information Technology, Lucknow

Neglected or underutilized crops species are generally native traditional crop species which are currently used at small scale within the local and national communities. They have potential contribution in nutritional supplements and mix food preparation but are under threatening conditions due to negligence in research, marketing and production areas. Therefore, due to in some way non competitive with major crops less exploited from economic point of view. Moreover, decline use of these crops may reduce the genetic base and prevent the use of distinctive useful characters in crop adaptation and improvement. This article pointed towards contribution of neglected crops in food security as well as major contribution for generating income for poor. Major crops may face environmental challenges in near future and therefore to reduce over dependence on these crops it is important to use neglected crops as a part of progress in the direction of attaining food security. Scientific researches and release of funding from government are necessary to encourage the use and cultivate these species to combat hidden hunger. These neglected plants contribute in dietary diversification, food and agricultural interventions including fortification focusing towards sustainable development in agriculture. Thus, reducing the challenging task of ever-growing population with a healthy balanced diet and the threats faced by agricultural crops due to changing climate highlight the immediate requirement to exploit the beneficial attributes of neglected crops.

Keywords: Modern Perspectives, Crops, native traditional crop

Introduction

Agriculture plays an important role in boosting the economy of India by achieving the food demand of emergent population and also supplies necessary food or raw material globally enhancing the financial status of our country. The overall GDP of around 15.87% contributed by agriculture have been reported in our country (Himani, 2014). Category of crops can be divided in a number of ways such as a particular season, soil conditions, cultivation region, cultivation processes and economic value of crops etc (Table 1). On the basis of seasons, the crops in India are divided into three types: rabi, kharif and Zaid (Table 2) (NCERT).

Tropical climates are normally hot or worm all year round. Many tropical areas have dry and wet season depending on the location. The plants growing in tropical climates are categorised as “tropical crops”. Main crops cultivated in India can be categorised in to four groups, for instance, Food grains (Rice, Wheat, Maize, Millets and Pulses), Cash Crops (Cotton, Jute, Sugarcane, Tobacco, and Oilseeds), Plantation Crops (Tea, Coffee, Coconut and, Rubber) and Horticulture crops such as Fruits and Vegetables (Table 2). Tropical plants are quite hardy, growing relatively well as in more northern climates (NCERT).

Due to adverse environmental conditions such as drought, radiation, temperature, low consumption of fertilizers, and the prevalence of pests and diseases crop yields are low in the tropics (Chang, 1977). In Asia, notably India, the per capita accessibility of “coarse grains” (millets) has undergone through relative neglect. Various cereals, legumes and many other local foods from India also faced ignorance among people. These foods have many traditional uses based on indigenous faith of health benefits with very little relations to research outputs. Although many literatures are available concerning these crops but owing to lack of support by research it was not promoted extensively. Since this trend has coincided with the total decline in intake of cereals, the net effect is a 50 percent decrease in the diet’s fibre content. The resulting distortion in the productivity of neglected crops such as millets has in turn been reflected in the relative market prices of these food grains. (Bhattacharjee *et al,* 2005).

*Corresponding author.
Email: madhusrivastava2010@gmail.com

Table 1 – Indian crop categories

Types of crops	Category	Major Producing region in India
Food grains		
Rice	Kharif	West Bengal, Uttar Pradesh, Andhra Pradesh, Punjab, Bihar, Orissa, Chhattisgarh, Assam, Tamil Nadu, Haryana
Wheat	Rabi	Uttar Pradesh, Punjab, Haryana, Rajasthan, Bihar, Gujarat, Maharastra, West Bengal, Uttarakhand
Coarse Cereals / Millets		
Jowar, Bajra, Ragi	Kharif	Maharashtra, Karnataka, and Rajasthan.
Maize	Kharif	Kranataka, Uttarpradesh, Bihar, Andhra Pradesh, Madhya Pradesh
Pulses		
Gram, Tur or arhar (Pigeon Pea or Red Gram), urd (black gram), mung (green gram), masur (lentil), kulthi (horse gram), matar (peas)	Kharif, rabi	Madhya Pradesh, Uttar Pradesh, Rajasthan, Maharashtra and Karnataka.
Cash Crops		
Sugarcane	Kharif, rabi, tropical and subtropical	Uttar Pradesh, Maharastra, Karnataka, tamil nadu, Andhra Pradesh, Bihar, Gujarat, Haryana, Uttarakhand, Punjab
Cotton	Kharif, tropical and subtropical	Gujarat, Maharashtra and Andhra Pradesh, Haryana, Madhya Pradesh, Punjab, Rajasthan, Karnataka, Tamil Nadu, Orissa.
Groundnut	Kharif and Rabi	Gujarat, Andhra Pradesh and Tamil Nadu.
Jute	Zaid, tropical	West Bengal, Bihar, Assam, Andhra Pradesh, Orissa, Meghaylaya, Nagaland, Tripura, Uttar Pradesh
Tobacco	Tropical	Maharashtra, Tamil Nadu
Plantation crops		
Tea	Kharif, Tropical and subtropical climate	Assam, West Bengal, Tamil Nadu, Meghalaya, Himanchal Pradesh, Karnataka
Coffee	Kharif, Baba Budan Hills, Nilgiri hills	Karnataka, Kerala, Andhra Pradesh, Telangana, Odhisha, Assam, Meghalaya, Arunchanchal Pradesh, Manipur, Nagaland and Tamil Nadu
Coconut	Rabi	Kerala, Tamilnadu, Karnataka, Andhra Pradesh
Rubber	Rabi	Kerala
Horticulture Crops		
Fruits	Tropical and subtropical	Mangoes of Maharashtra, Andhra Pradesh, Uttar Pradesh and West Bengal, oranges of Nagpur and Cherrapunjee (Meghalaya), bananas of Kerala, Mizoram, Maharashtra and Tamil Nadu, lichi and guava of Uttar Pradesh and Bihar, pineapples of Meghalaya, grapes of Andhra Pradesh and Maharashtra, apples, pears, apricots and walnuts of Jammu and Kashmir and Himachal Pradesh
Vegetables	Tropical and subtropical	It is an important producer of pea, cauliflower, onion, cabbage, tomato, brinjal and potato
Spices		
Cardamon, pepper, chillies, turmeric, nutmeg, arecanut, coconut, cinnamon, clove, ginger	1000-2000m altitude of western ghats and other hilly areas	Kerala, Karnataka

(Source FAO.org and ncert.nic.in)

Table 2 – Indian Crop seasons

Seasons	**Kharif**	**Rabi**	**Zaid**
Sowing month	June- July	October-November	March-June
Harvesting time	September- October	April-may	June - July
Growth requirement	Require lot of water and hot weather to grow	Requires warm climate for germination f seeds and cold climate for growth	They require warm dry weather for major growth period and longer day length for flowering.
Examples	Rice, Jowar, Bajra, Maize, cotton, groundnut, jute, sugarcane, turmeric, pulses	Wheat, oat, gram, Pea, barley, Potato, tomato, Onion, oil seeds	Cucumber, bitter gourd, pumpkin, watermelon, muskmelon, moongdal

(Source FAO.org and ncert.nic.in)

When proper attention in the field of research and development, national and international policy and legal frameworks may not be given to support the conservation and sustainable, which is use of the crop generally referred as neglected crops. While a particular crop is not utilized on the basis of geography and potential to supply food and better diets among population is called underutilized crops. There may be cases where specific crop species are underutilized at certain region, but not underutilized in other regions globally (Williams and Haq, 2002).

Due to lack of research and development, most effective commercialization, marketing and regulatory structure strategies about the ecological development of neglected crops, very little information in terms of uses and economic value are available about the underutilized or neglected crops (Ahmad and Javed, 2007; Mal, 2007). Considering all these, research and conservation approaches are needed to protect the neglected crops to ensure their sustainable uses and development for future generations. The aim of this article is to identify and prioritize the India's neglected and underutilized crop species for importance and document the knowledge gaps associated with them that can be addressed by both national and international communities.

What are Neglected crops?

Over the world, a number of plant species are cultivated for food and also play an important role in food security, nutrition and income generation of the poor people; but facing ignorance by the government in research funding as well as cultivation by producers, are called neglected and underutilized crops (Anonymous, 2015). The examples of neglected and underutilized species that are not much exhaustive given below:

Amaranthus caudatus (Amaranth, Ramdana), *Chenopodium quinoa* (Quinoa), *Echinochloa crusgalli* (Barnyard millet), *Eleusine coracana* (finger millet), *Fagopyrum esculemtum* (Buck wheat, kotu), *Panicum miliaceum* (Proso millet, Ragi), *Panicum sumatrense* (little millet), *Paspalium scrobiculatum* (kodo millet), *Setaria italic* (Italian or foxtail millet), *Linum usitassimum* (Linseed), *Hordeum vulgare* (Barley), *Pennisetum typhoideum* (Bajra), *Sorghum vulagre* (Jowar), *Phaseolus mungo* (Blackgram), *Dolichos biflorus* (Horse gram), *Phaseolus aureus* (Green gram), *Cajanas cajan* (red gram/pigeon pea), *Phaseolus aconitifolius* (Moth bean), *Cicer arietinum* (Bengal gram/chick pea), *Lathyrus sativus* (Khesari), *Glycine max* (Soybean) (Moreno et al, 2014). These crops play an important role in the traditional food systems of communities as many kinds of traditional foods and beverages are derived from them. It has also been reported that their grain protein is richer in sulphur-containing and other essential amino acids compared to other major cereals (Bala Ravi et al. 2010).

Rationale regarding crop negligence

Agricultural technicians highlighted that most of the developing countries support research only for specified major crops in their fund declaration. Therefore due to lack of grant support for research projects on neglected crops, most of the agriculturist as well as farmers are not interested to grow these crops in large quantity. Moreover, lack of organized markets, improved agricultural practices, limited post harvest shelf life, poor taste or unpleasant texture and major susceptibility to pathogens for growing, neglected crops limited their value for providing the food to people (Durst P and Bayasgalanbat N, 2014).

The above listed constrains revealed that unsatisfactory scientific research prone towards non profitable production of neglected crop species. Many young producers are mostly interested in growing cash crops such as cotton, sorghum and cassava from which they can generate lot of money in less time (Dansi et al, 2012). Lack of interest by researchers, agriculturists, extension workers, producers and lack of technical information create threat of continued genetic erosion and disappearance of these crops. These neglected crops are enriched with nutrition, therefore their erosion can results in restriction of nutritional status and food security to the poor while their increased utilization can produce better nutrition and fight unseen hunger (Padulosi et al, 1999; Johns and Eyzaguirre, 2006; Ghane et al, 2010).

The Green Revolution, despite its many benefits, ignored minor and neglected crops and in its place focused on rice and wheat. Now days our food habit is going in the unconstructive way due to lack of diversity in food intake with respect to nutritional value (Indian Institute of Medical Research). As these neglected crops are considered as poor man's food, producers and farmers are not taking interest to grow it. Moreover, apart from lack in research funding by government, there is an approach by the Public Distribution System, which provides cheap grains to the poor and played a key role in pushing nutritionally rich millet away from the plate.

Role of neglected crops in Food security

The world population is majorly dependent on three crops such as wheat, rice and maize for fulfilling their basic diet of carbohydrates, fats, and proteins. Therefore these major crops govern human consumption (Collins and Hawtin, 1999). Moreover, various scientific researchers are making transgenic of these major crops to improve the food security. However, merely focus on these major crops productivity under high agricultural practices cannot convene the challenges of food insecurity and probably create alarming situation for agriculture even more susceptible to environmental stresses in future. Neglected, minor or underutilized crops are the tag generally applied to plant species that are native, rather than non-native or introduced from outside thus called adapted, and generally people grow these crops for culture and diets accomplishment (Padulosi *et al.* 2006). It has been reported that women farmers found to cultivate neglected crops for survival purposes, while men preferred to cultivate the major cash crops (Mayes *et al,* 2012).

Neglected crops can play possible role in enhancement of food safety in the following ways: (i) It help the poor people in survival and earnings; (ii) It help to decrease over dependencey on major crops; (iii) It facilitate enhanced sustainability of agriculture with reduced input (iv) It play major role in improved food quality; and (v) It also support to conserve and celebrate cultural and dietary range (NPR.org).

Nutritional Value of the neglected Species

Data obtained from the Internet, articles and other sources on the nutritional values of some neglected crops revealed that most of the species have interesting nutritional value and if promoted, will surely help to combat malnutrition in India.

The chemical compositions and the nutritional values of priority neglected crops compiled in Table 3.

Millets

Millets are easy to digest and are highly nutritious, gluten free as well as fibre enriched crops. Dissimilar to wheat and rice which need a lot of inputs like water and fertilizers, millets grow well in dry region. It has been reported by ICRISAT (Crops Research Institute for the Semi-Arid Tropics) that one rice plant needs almost 2.5 times more water than needed by a single millet plant. Elderly farmers remember that millet was once the staple food in the Mandya, Dharwad and Tumakuru regions, but was replaced due to the invasion of rice and wheat in the last three to four decades (Saxena et al, 2018; Kumar et al, 2016; Upadhayaand Vetriventha, 2018). Among these, Barnyard Millet is the fastest growing (six weeks crop) and offering ten times more fibre than wheat. Koralu is drought-resistant and can be cultivated in any kinds of soil. while Kodo Millet, also drought-resistant, is an ideal crop for fallow and infertile lands with pebbles. Its straw is used as thatch for roof and preparing *mudde* (balls) to preserve seeds. Small millet, which is presently being grown in the dry land districts of Karnataka, requires very few inputs: a mere INR 5,000 (USD 69) per acre. Farmers prefer to shift to small millets, which help them adapt to climate change, and give an assured yield of around 8-10 quintal per acre with low input costs (University of Agricultural Sciences) (Bandyopadhyay et al, 2017).

Consider neglected crops as Superior grain

In the current agricultural scenario, millet producers can be considered as supporters of sustainable farming

Table 3 – Indian crop categories

Crops	Common names	Chemical constituents	Medicinal value	References
Pennisetum glaucum	Pearl millet	Rich in amino acids, arginine, threonine, valine, isoleucine and lysine	The plant is appetiser and tonic. It is also useful in the treatment of heart diseases	Adeola and Orban, 1995; Chopra et al, 1986
Sesamum indicum	Sesame	Rich in protein (21.44%), flavonoids, alkaloids and tannin, Ca and K and also found to have sesamin and sesamolin	Cholesterol lowering effect in humans and alos prevent high blood pressure.	Anilakumar et al, 2010
Sorghum bicolor	Milo or Jowar	Rich in carotenoids, flavonoids and phenolic acids, lycopene and β-carotene; fatty acid profiles of the leaves revealed palmitic, stearic, oleic and linoleic acid	Natural antioxidant and essential fatty acids that could fight cardiovascular related diseases.	Abugri et al, 2013
Amaranthus caudatus	Amaranth, Ramdana	Rich in flavonoids, steroids, terpenoids and cardiac glycosides	Antimicrobial activity	Maiyo et al, 2010
Chenopodium quinoa	Quinoa	Rich in amino acid, minerals and vitamins, and has also been found to contain compounds like polyphenols, phytosterols, and flavonoids	Used as novel functional food	Abugoch James LE, 2009
Echinochloa crusgalli	Barnyard millet	Rich in alkaloids, glycosides, carbohydrates, flavonoids, phytosterols/terpenes, proteins, and saponin	plant possessed antidiabetic, anticancer, antioxidant, antimicrobial hypolipidemic and anti-obesity effects.	Esmail and Snafi, 2017
Eleusine coracana	finger millet	High content of protein, calcium (0.38%), dietary fiber (18%) and phenolic compounds (0.3–3%)	Anti-diabetic, anti-tumerogenic, atherosclerogenic effects, antioxidant and antimicrobial properties.	Devi at al, 2014
Panicum miliaceum	Proso millet, Ragi	Rich source of protein, starch, trace elements, dietary fibre and vitamins; Phenolic compounds like antioxidants and beta carotene	Decrease the level of low density lipoprotein cholesterol in blood and injury to the liver	Kalinova, 2007
Panicum sumatrense	little millet	Rich in carbohydrate	Used in formulation of diets and value added foods	Kamatar et al, 2012
Paspalium scrobiculatum	kodo millet	Presence of tannins, phenolics, saponins, proteins and carbohydrates.	Management of diabetes.	Bhatia et al, 2010
Setaria italic	Italian or foxtail millet	Rich in alkaloids, phenolics, reducing sugars and flavonoids , annins and terpenoids	Antioxidant activity	Suma and Urooj, 2011
Triticale,	Manmade cereal from wheat and rye	Starch and non-starch polysaccharides	Food and beverage applications	Zhu, 2018
Linum usitassimum	Linseed	Presence of linolenic acid, linoleic acid, lignans, cyclic peptides, polysaccharides, alkaloids, cyanogenic glycosides, and cadmium	Management of diarrhea and gastrointestinal infections.	Shim et al, 2014; Palla et al, 2015
Hordeum vulgare	Barley	Cyanogenic glycoside, Coumarins, flavonoids	The seeds are astringent, demulcent, refrigerant, emollient, and diuretic, intellect promoting, aphrodisiac, digestive and tonic.	Kumar et al, 2016
Pennisetum typhoideum	Bajra	Rich in protein, total and reducing sugars levels varied, minerals	Used as millet fortification	Opoku et al, 1981
Sorghum vulagre	Jowar	Rich in Protein, starch, phenolic and antioxidant compounds	inhibit tumour development, help to reduce Celiac Disease (CD), antidiabetic	Kulamarva et al, 2009

Crops	Common names	Chemical constituents	Medicinal value	References
Phaseolus mungo	Blackgram	presence of carbohydrates, flavonoids, saponins, tannins, alkaloids, steroids and vitamin C qualitatively, whereas flavonoids	anti-inflammatory, analgesic, ulcerogenic, hypoglycemic, hepatoprotective, immunostimulatory, anticonvulsant, antioxidant, narcotic activity	Varma et al, 2013
Cajanas cajan	red gram/ pigeon pea	High levels of proteins and important amino acids like methionine, lysine and tryptophan. globulins, cajanin and concajanin	Treatment of ischemic necrosis of the caput femoris, aphtha, bedsore and wound healing	Pal et al, 2011
Cicer arietinum	Bengal gram/ chick pea	carbohydrates, proteins, amino acids, fixed oils, phytosterols, alkaloids, phenolic compounds and tannins, flavonoids, glycosides, saponins, amino acids, iron, phosphate, sulphate, and chloride	aphrodisiac, estrogenic, antioxidant, ACE- inhibition, antidiabetic, anti-inflammatory, hypocholesterolaemic, antidiarrhoeal antidiarrhoeal, anticonvulsant, hepatoprotective, anticancer, diuretic, anti-nephrolithiasis and many other pharmacological effects	Esmail and Snafi, 2016
Lathyrus sativus	Khesari	Starch, cane sugar, leguminvicilin, legumelin, fixed oil, gum resin, oleo-resin, alkaloids, carbohydrates, flavonoids, terpenes, phenols, tannins, vitamin C, riboflavin, carotenoids, beta-carotene, proteins and amino acids.	Antioxidant, nervous, antidiabetic, analgesic, antipyretic and cardioprotective effects.	Al snafi, 2019

(Source FAO.org and ncert.nic.in)

exercises in terms of constructing climate resilience or the ability to acclimatize under adverse environmental conditions, conquer constraints, reduce disruptions and enhance opportunities.

There should be seed bank of these crops and also distributed among farmers with the promise that they return double the volume once the crop is harvested. Farmers should be encouraged to grow neglected crops such as millets and make them believe that it is truly superior grain not inferior grain as it has been known in recent years.

Importance of neglected crops

These crops continue to play an important role in the subsistence and economy of poor people throughout the developing world, particularly in the agro biodiversity-rich tropics. In spite of their potential for dietary diversification and the prerequisite of micronutrients such as vitamins and minerals, they are not able to draw much attention by researcher and thus little research and development has been identified**.** Besides their commercial potential, many of the neglected crops also provide significant environmental services, as they are adapted to marginal soil and climate conditions.

Farmers gain a lot of money through commercialisation of the priority neglected crops and this helps them to improve their position within the society. It also encourage women's empowerment that female farmers contribute more significantly to the production of the priority neglected species than their male counterparts (Rahman and Ibrahim, 2007; Ogato et al, 2009; Ayoola et al, 2011; Umar et al, 2010).

Where a developing country has a nationally recognised programme on neglected crops, there is more likelihood of progress in incorporating a number of species for industrial applications. In India various research programmes on some plant species such as guayule (*Parthenium argentatum*), jojoba (*Simmondsia chinensis*), guar (*Cyamopsis*), *Jatropha, Cuphea* etc. have been approved which focus on food plants, plants for extreme environmental or emergency food situations. Importance should also be given to neglected crops for their consumption as well as research oriented programmes (Gautam, et al., 1999).

Conclusion

It has been revealed through market survey that neglected crops are a chief source of domestic

revenues and considerably support decline in malnourishment as well as poverty reduction. Various literatures have presented that a variety of neglected crops such as Millets are full of nutrition and possess medicinal importance and therefore it is believed that it help in promotion of their consumption which would control malnutrition or under nourishment and ready to lend a hand in improvement of health status of the indigenous populations. Although, it is most frequently used in rural population but due to lack of scientific research and awareness, these crops are underutilized or subjected to negligence globally. India has a great diversity of neglected and underutilised crop species. These crop species should be promoted on priority basis by national agricultural system with the help of political will and financial support. These species comprise of huge nutritional, medicinal and economic value and therefore basic ethno-botanical investigation should be started at national level including all the possible performers comprising researchers, developers, and producers. The knowledge about neglected species should be spread the sub region and thereafter be extended to other countries not included in the agricultural project. We recommend that promotion of these neglected crops is very necessary to support poor population, not giving extra burden on major crop generation, reducing genetic erosion for the next coming decade and also national and international research and development funders in the field of agriculture should prioritize neglected crops endowments.

References

1. Abugoch James LE, Chapter 1 Quinoa (*Chenopodium quinoa* Willd.): Composition, Chemistry, Nutritional, and Functional Properties Advances in Food and Nutrition Research Volume 58, 2009, Pages 1-31
2. Abugri DA[1], Tiimob BJ, Apalangya VA, Pritchett G, McElhenney WH. Bioactive and nutritive compounds in Sorghum bicolor (Guinea corn) red leaves and their health implication. Food Chem. 2013 May 1;138(1):718-23. doi: 10.1016/j.foodchem.2012.09.149. Epub 2012 Nov 10.
3. Adeola O and Orban JI, 1995. Chemical composition and nutrient digestibility of pearl millet (*Pennisetum glaucum*) fed to growingpigs. Journal of cereal science 22(2): 177-184.
4. Ahmad S. S. and Javed S., "Exploring the economic value of underutilized plant species in Ayubia National Park," *Pakistan Journal of Botany*, vol. 39, no. 5, pp. 1435–1442, 2007.
5. Al-Snafi, Ali. (2019). Chemical Constituents and Pharmacological Effects of Lathyrus Sativus -A Review. 9. 51-58.
6. Anilakumar, Pal, Ajay, Khanum, Farhath, Bawa, Amarinder 2010. Nutritional, Medicinal and Industrial Uses of Sesame (Sesamum indicum L.) Seeds - An Overview Agriculturae Conspectus Scientificus (ACS) (acs@agr.hr); Vol.75 No.4
7. Anonymous, 2015. Neglected tropical crops? *Nature Plants* volume 1, Article number: 15204 https://www.nature.com/articles/nplants2015204
8. Ayoola J. B., Dangbegnon C., Daudu C. K. et al., "Socio-economic factors influencing rice production among male and female farmers in Northern Guinea
9. Bala Ravi, S., Swain, S., Sengotuvel, D. & Parida, N.R. 2010. Promoting nutritious millets for enhancing income and improved nutrition: a case study from Tamil Nadu and Orissa. In Bhag Mal, S.
10. Bandyopadhyay T, Muthamilarasan M and Prasad M (2017) Millets for Next Generation Climate-Smart Agriculture. Front. Plant Sci. 8:1266. doi: 10.3389/fpls.2017.01266
11. Bhatia G, Barve, Ashutosh 2010. Phytochemical Studies of the Grains of Paspalum scrobiculatum International Journal of Pharmaceutical and Clinical Research 2 (2):66-67
12. Bhattacharjee L, Egal F, Collette L, Burlingame B, Nandi BK, Kuhnlein H (2005) Protecting and strengthening local food systems: Harnessing biodiversity and indigenous knowledge for food security, livelihoods and nutrition in "The Role of Biodiversity in Achieving The UN Millennium Development Goal of Freedom from Hunger and Poverty", Swaminathan Research Foundation (MSSRF), Chennai, India
13. Chang JH, 1977.Tropical Agriculture: Crop Diversity and Crop Yields *Economic Geography* 53 (3): 241-254
14. Chopra RN, Nayar SL, Chopra IC, 1986. Glossary of Indian medicinal plants (including the supplement) CSIR, New Delhi.
15. Collins WW, Hawtin GC, WW Collins, CO Qualset. Conserving and using crop plant biodiversity in agroecosystems, *Biodiversity in agroecosystems*, 1999 Boca Raton, Washington CRC Press(pg. 267-281)
16. Dansi A., Vodouhè R., Azokpota P., Yedomonhan H., Assogba P., Adjatin A., Loko Y. L., Dossou-Aminon I., and Akpagana K. 2012. Diversity of the Neglected and Underutilized Crop Species of Importance in Benin 19 pages https://doi.org/10.1100/2012/932947
17. Devi, P. B., Vijayabharathi, R., Sathyabama, S., Malleshi, N. G., & Priyadarisini, V. B. (2014). Health benefits of finger millet (Eleusine coracana L.) polyphenols and dietary fiber: a review. *Journal of food science and technology*, *51*(6), 1021–1040. https://doi.org/10.1007/s13197-011-0584-9
18. Durst P and Bayasgalanbat N, 2014 Promotion of underutilized indigenous food resources for food security and nutrition in asia and the pacific. Food and agriculture organization of the united nationsregional office for asia and the pacific, Bangkok.
19. Esmail A, Snafi Al, 2017. Pharmacology of Echinochloa crusgalli- A Review. Indo American J of Pharmaceutical Sciences 4(1)117-122
20. Esmail Ali and Al-Snafi The medical Importance of Cicer arietinum - A review IOSR Journal Of Pharmacy www.iosrphr.org (e)-ISSN: 2250-3013, (p)-ISSN: 2319-4219 Volume 6, Issue 3 (March 2016), PP. 29-40
21. Gautam, P.L., Sharma, G.D., Joshi, V. and S. Kockhar 1999 Opportunities for conservation of underutilised species and their sustainable use - Indian scenario. Paper presented at a CGIAR meeting, Chennai, 17-19 Feb. 1999
22. Ghane S. G., Lokhande V. H., Ahire M. L., and Nikam T. D., "*Indigofera glandulosa* Wendl. (Barbada) a potential source of nutritious food: underutilized and neglected legume in India," *Genetic Resources and Crop Evolution*, vol. 57, no. 1, pp. 147–153, 2010.

23. Himani, 2014. An analysis of agriculture sector in Indian economy. IOSR Journal of Humanities and Social science. 19(1):47-54.
24. http://ncert.nic.in/ncerts/l/jess104.pdf
25. http://www.fao.org/3/a0257e/A0257E02.htm
26. ICRISAT: India- Farmers turn to millets as a climate-smart crop https://www.icrisat.org/farmers-turn-to-millets-as-a-climate-smart-crop/
27. Kalinova J, 2007. Nutritionally important components of proso millet (Panicum miliaceum L.) Food 1(1):91-100. Global science book
28. Kulamarva Arun G., Venkatesh R. Sosle & G.S. Vijaya Raghavan (2009) Nutritional and Rheological Properties of Sorghum, International Journal of Food Properties, 12:1, 55-69, DOI: 10.1080/10942910802252148
29. Kumar P, Kumar R, Kumar P, 2016. Underutilized millets: A way to nutritional security. International J of Agriculture and environmental research. 2 (4):726-734.
30. Kumari R, Singh M, Kotecha Mita 2016. YAVA (HORDEUM VULGARE LINN.): A REVIEW Kumari Rajesh et al. Int. Res. J. Pharm. 2016, 7 (3)
31. Maiyo, Zacharia Raphael, Ngure Matasyoh, Josphat Chepkorir, R Phytochemical constituents and antimicrobial activity of leaf extract of three Amaranthus plant species Afr J Biochem 9 (21)
32. Mal B., 2007 "Neglected and underutilized crop genetic resources for sustainable agriculture," *The Indian Journal of Plant Genetic Resources*, vol. 22, no. 1, pp. 1–16,.
33. Mallikarjun Y Kamatar *1, Hemalatha S1 , Meghana DR1, Sharanappa Talawar1 and Rama K Naik 2013Evaluation of Little Millet (Panicum sumatrense) Land Races for Cooking and Nutritional Composition Volume 2, Issue 1, January-February ISSN No.: 2250 - 2637
34. Mayes S., Massawe F. J., Alderson P. G., Roberts J. A., Azam-Ali S. N., Hermann M., 2012. The potential for underutilized crops to improve security of food production, *Journal of Experimental Botany*, Volume 63, Issue 3, Pages 1075–1079, https://doi.org/10.1093/jxb/err396
35. Moreno ML, Comino I, Sousa C. 2014Alternative Grains as Potential Raw Material for Gluten-Free Food Development in The Diet of Celiac and Gluten-Sensitive Patients. Austin J Nutri Food Sci.;2(3): 1016
36. Ogato G. S., Boon E. K., and Subramani J., 2009 "Gender roles in crop production and management practices: a case study of three rural communities in Ambo district, Ethiopia," *Journal of Human Ecology*, vol. 27, no. 1, pp. 1–20.
37. *Opoku AR, Ohenhen SO, Ejiofor N,* 1981Nutrient composition of millet (Pennisetum typhoides) grains and malt *J. Agric. Food Chem.* , 29, 6, 1247-1248
38. Padulosi & S. Bala Ravi, eds. Minor m illets i n Sou th A sia: learnings f rom I FAD-NUS pr oject in I ndia a nd N epal. Rome, Italy, Bioversity International and Chennai, India, the M.S. Swaminathan Research Foundation.
39. Padulosi S, Hodgkin T, Williams JT, Haq N. Engels JMM, Ramanatha Rao V, Brown AHD, Jackson MT. 2002. Underutilised crops: trends, challenges and opportunities in the 21stcentury, *Managing plant genetic diversity*, , vol. Vol. 30RomeIPGRI(pg. 323-338)
40. Padulosi S., Eyzaquirre P., and Hodgkin T.,1999. *Challenges and Strategies in Promoting Conservation and Use of Neglected and Underutilized Crop Species*, edited by J. Janick, ASHS Press, Alexandria, Va, USA, 1999.
41. Pal Dilipkumar, Mishra Pragya, Sachan Neetu, Ghosh Ashoke K 2011. Biological activities and medicinal properties of *Cajanus cajan* (L) Millsp. REVIEW ARTICLE 2(4):207-214
42. Palla AH[1], Khan NA[1], Bashir S[1], Ur-Rehman N[2], Iqbal J[1], Gilani AH. 2014. Pharmacological basis for the medicinal use of Linum usitatissimum (Flaxseed) in infectious and non-infectious diarrhea. J Ethnopharmacol. 2015 Feb 3;160:61-8. doi: 10.1016/j.jep.2014.11.030. Epub Nov 26
43. Rahman S. A. and Ibrahim H., 2007 "Socio-economic study of gender role in farm production in Nasarawa state of Nigeria," *Asia-Pacific Journal of Rural Development*, 17, (1) : 57–66.
44. Saxena R, Vanga SK, Wang J, Orsat V, Raghavan V, 2018. Millets for food security in the context of climate change: A review. Sustainability 10, 2228.
45. Shim, Youn & Gui, Bo & Wang, Yong & Reaney, Martin. 2014. Flaxseed (Linum usitatissimum L.) bioactive compounds and peptide nomenclature: A review. Trends in Food Science & Technology. 38. 10.1016/j.tifs.2014.03.011.
46. Sua PF, Urooj A, 2011 Antioxidant activity of extracts from foxtail millet (*Setaria italica)* J Food Sci Technol. 2012 Aug; 49(4): 500–504
47. T. Johns and P. B. Eyzaguirre, "Symposium on "wild-gathered plants: basic nutrition, health and survival" Linking biodiversity, diet and health in policy and practice," *Proceedings of the Nutrition Society*, vol. 65, pp. 182–189, 2006.
48. Umar H. S., Luka E. G., and Rahman S. A., 2010."Gender based analysis of labour productivity In sesame production in doma local government area of Nasarawa state, Nigeria," *PAT Journal*, 6, (2):. 61–38.
49. Upadhyaya, H D and Vetriventhan, M . 2018. *Underutilized Climate-Smart Nutrient Rich Small Millets for Food and Nutritional Security.* In: Regional Expert Consultation on Underutilized Crops for Food and Nutritional Security in Asia and the Pacific – Thematic, Strategic Papers and Country Status Reports. Asia-Pacific Association of Agricultural Research Institutions (APAARI), Bangkok, Thailand, pp. 109-120. ISBN 978-616-7101-10-1.
50. Varma, Rajeev & Garg, Vipin & Singh, Lubhan & Kumar, Dinesh. 2013. Pharmacognostic Evaluation and Phytochemical Analysis of Seeds of Vigna mungo (L.) Hepper. Open Research Journal of Phytotherapy & Pharmacognosy. 1. 1-9.
51. Williams, J.T. and Haq, N. 2002. Global research on underutilized crops. An assessment of current activities and proposals for enhanced cooperation. ICUC, Southampton, UK.
52. www.npr.org. A Forgotten Group Of Grains Might Help Indian Farmers – And Improve Diets, Too https://www.npr.org/sections/thesalt/2017/02/09/514171025/how-an-indian-state-is-putting-millets-back-on-people-s-plates
53. Zhu F, 2018, Triticale: Nutritional composition and food uses. Food Chem. 2018 Feb 15;241:468-479. doi: 10.1016/j.foodchem.2017.09.009. Epub 2017 Sep 6.

Journal of the Maharaja Sayajirao University of Baroda: Science & Technology
Vol. 57, 2023, pp. 14-22

FPGA Based Improved Vector Control of Three-Phase Induction Motor

Sumit Kumar Gupta[1,a*], Shashi Bhushan Singh[2,b] and Pradeep Kumar[3,c]

[1]Electrical Engineering, ECE, School of Studies of Engineering and Technology, Guru Ghasidas Vishwavidyalaya Bilaspur India-4950092

[2,3]Electrical Engineering Department, NIT Kurukshetra, Kurukshetra, Haryana, India – 136119

[a] sgupta@ggu.ac.in, [b] sbsingh@nitkkr.ac.in, [c] pradeepkumar@ieee.org

Vector control (VC) and direct torque control (DTC) schemes for an induction motor drive (IMD) system have been prevalent in an industrial environment. To achieve the advantages of both the control scheme, they are combined, resulting in improved vector control (IVC). Conventionally, the control system employed for implementation of these controllers involves analog devices, which depend on the external environment and temperature. This affects the operation of the drive system. This paper attempts to overcome this drawback by presenting a field programmable gate array (FPGA) realization of the IVC for IMD using Xilinx System Generator (XSG). The design is implemented and verified within the Simulink environment. The implementation is performed considering the challenges of these conversions of control designs from analog to digital. Reliability and efficiency of the approach adopted for rapid prototyping using XSG in Simulink environment have been established. The simulation results validate dominance of IVC scheme over VC and DTC schemes for IMD.

Keywords: Improved Vector Control, Induction Motor Drives, FPGA.crop

1. Introduction

The control Induction motor drives (IMDs) has been a matter of research for a long time. Developments of vector control (VC) and direct torque control (DTC) was a significant breakthrough in IMD area [1][2]. These control strategies have their own merits like DTC has direct torque and flux control, no coordinate transform, absence of PWM signal generator and current regulator, good dynamics, low sensitivity to electric machine parameter changes, no PI regulator, while the VC offers low torque ripple, good dynamics, constant sampling frequency, and sinusoidal current (in linear modulation angle) [3][4]. Improved vector control (IVC) combines the advantages of DTC and VC resulting in a new topology, avoiding some of the difficulties in implementation of DTC and VC [5]. IVC being advantageous has a complex control structure. Thus, to make in hardware implementable, efficient control scheme are required. An efficient control system offers the distinction in terms of its performance, i.e., accurate torque control, good dynamic response, and ripple free current, etc. To achieve this, fast computation units are required. Digital signal processor (DSP) and microprocessor are popular for such applications. But, regardless of their fast response, they have complicated circuitry, limited function, and rigid circuitry [6]. Nowadays, Field Programmable Gate Arrays (FPGAs) are of great interest in control application as they provide dedicated and reconfigurable hardware solutions. Studies have shown the suitability of digital hardware solutions for specific needs of target algorithm, such as FPGA over software solution viz. DSP, ASICs and microcontroller, as significant integration density, designing parallel architectures, fast execution time and their reprogramability for flexible controller.

Mostly, FPGA implementation are addressed using hardware description languages (HDLs) like VHDL or Verilog, but it has loss of coupling between model (i) debugging difficulties, and (ii) functional verification, leading to delay in design and implementation [7]-[9]. Use of Xilinx System Generator (XSG) based design flow system level design is a better alternative exploring architecture, debugging in hardware and provides a more attractive model than HDLs. Limited numbers of references [10]-[13] have proposed the simulation of variable speed drives using XSG.

Therefore, this paper presents an FPGA based

controller realization using XSG on MATLAB/ Simulink platform and prototype verification using hardware co-simulation for the IVC. The proposed approach offers advantages, such as one-time modeling of the algorithm, and significant time-saving as the XSG blocks provide the precise hardware design for algorithm implementation on the hardware. The performance is compared with VC and DTC on the same platform using hardware co-simulation. It has been established that the XSG IVC scheme exhibits fast dynamic response as well as less torque pulsation.

Rest of the paper is organized as follows: Section II examines the principle of IVC, control circuit modeling, block suitability and prototype verification. Section-III presents the simulation results with brief discussion and conclusions are drawn in Section-IV.

1.1. **Improved Vector Control Scheme (IVC) [3]**

DTC and VC are used to control the torque of IMDs for more than three decades. In VC, the direct-(i_d), and quadrature-axis currents, i_q, are directly related to flux, Ψ_r, and torque, T_e, respectively, whereas in DTC calculation of torque and flux requires, neither any current control nor any PWM signal generator. Application of DTC has been a matter of concern due to high current and torque ripples during operation. In terms of response, DTC has a fast dynamic response due to predefined switching of power electronic devices in the lookup table. While, in VC, i_d and i_q are controlled rather than torque and flux, resulting in reduced computational burden.

The Improved Vector Control includes the advantages of both the schemes and avoids the implementation difficulties of either of the scheme. The new scheme includes vector control in connection with a switching table based on space vector modulation scheme. The comparison of motor performance under scheme suggested with respect to those obtained under DTC and VC confirms faster dynamics than that of VC and less system variable pulsations than those under DTC. The idea comes on the fact that there is direct relationship between the hysteresis control of flux linkage in DTC and direct axis current control in VC. Similarly the hysteresis control of electromagnetic torque in DTC corresponds to quadrature axis current control in VC. As DTC provide a faster torque response due to faster selection of the status of the power electronics switches.

The approximated equations for controlling torque and flux using IVC is [5]

$$\Delta T_e = K cos\gamma |\psi_r| \Delta\psi_T \quad (1)$$

i.e., $\Delta T_e \; \alpha \; \Delta\psi_T$

$$\Delta\psi_s = \Delta\psi_F \quad (2)$$

$$\begin{cases} \Delta\psi_F \; \alpha \; \Delta i_d \\ \Delta\psi_T \; \alpha \; \Delta i_q \end{cases} \quad (3)$$

In proposed IVC, the merits of both these topologies have been combined. The block diagram of the IVC is presented in **Fig. 1 (a).** In IVC, i_d and i_q are calculations of VC, and predetermined switching of DTC has been adopted. So, the IVC works with less computation burden and fast switching. The emphasis of present work is to explore IVC hardware realization suitability using its XSG. This implementation eliminates the torque and flux estimation inaccuracy in fixed point format by eliminating the torque and flux estimator.

1.1. **System Level Modeling using System Generator**

Advances in the FPGA have allowed development of compact and complex high-performance controllers. The system level design for a FPGA can be performed using two methodologies, namely, high-level languages and visual data flow [13]. Language based approaches have been found successful for system modeling, specification, and algorithm verification, but remain inapt for targets other than a microprocessor. On the other hand, visual data flow offers libraries of functional blocks that can be poised to model a system, similar to traditional schematic capture tools. These blocks and the simulation environment allow graphical modeling of a system.

XSG is one such design flow-based system level design commercial tool developed by Xilinx Inc. It contains set of instructions written in HDL, which run in Xilinx Integrated Software Environment (ISE). It allows exploring the architecture, hardware debugging and provides a model more attractive than HDLs. Its high level of abstraction allows replacement of Simulink blocks easily. Also, it translates the designs into faithful, synthesizable, and efficient hardware realization [13].

The system is modeled using XSG blocks. Reliability and efficiency of the implementation is assured as the system model, and hardware implementation are bit-identical and cycle-identical, at sample times defined in Simulink, and they use Intellectual Property (IP) cores that provide a range

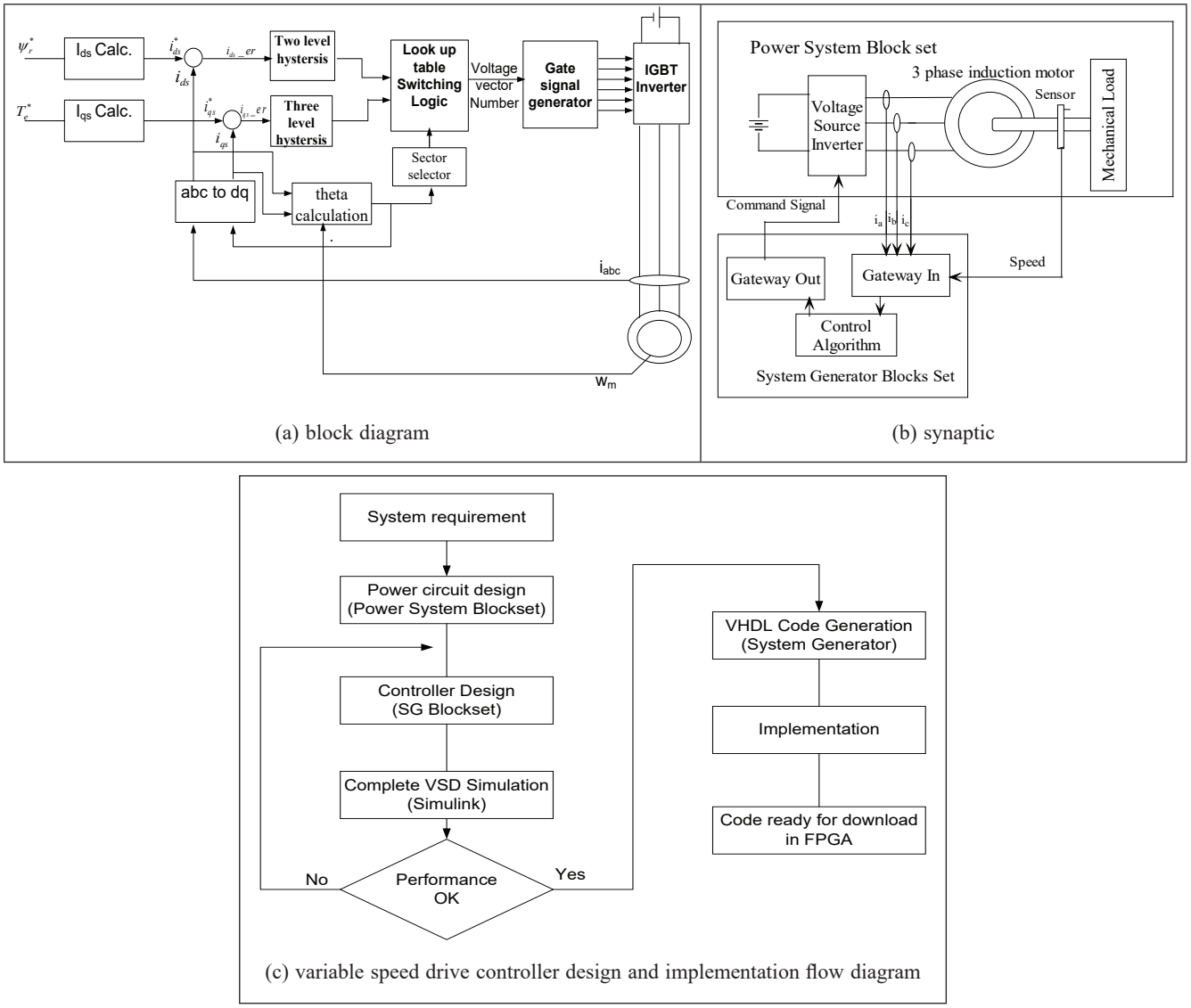

Fig. 1. Combined VC and DTC system (a) block diagram and (b) its synaptic (c) Flow Diagram

of functionality from arithmetic operations to complex DSP algorithms [14]-[15]. These generated HDL files are then synthesized in a synthesizer, leading to a schematic of the logic design which is converted into a configuration file, downloadable on the target device**.**

1.1. **IVC Simulation**

To simulate the IVC scheme motor drive, the power circuit is implemented using power system block set of Simulink and control scheme is implemented using XSG block set. Both the power circuit and control circuit are simulated simultaneously in MATLAB using XSG. Synoptic of the proposed control system is shown in Fig. 1(b). XSG block set contain one token block, which allows to select the device to be used for implementation, FPGA clock period, Simulink system period and code to be generated for targeted an FPGA with the option of VHDL or Verilog. After Simulation, the VHDL code generated, in Xilinx to utilize it for FPGA programming. The advantage of with XSG is the VHDL code generated is guaranteed to be implemented and requires lesser time because of only one step for both software and hardware simulation testing. Fig. 1 (c) gives systematic flow chart representation of the proposed design

1.2. Control System Architecture

For the IVC control scheme, shown in Fig. 1, the reference current of direct-axis i_{ds}^* and quadrature axis i_{qs}^* are obtained as in VC. These reference currents are compared with the actual/ measured currents to obtain the current error in *d-q* reference frame as in DTC. These current errors are fed to hysteresis current controller (HCC), implemented using XSG blocks as shown in Fig. 3. For torque and flux command, 3- and 2-level HCC are used, respectively.

The output of HCC and the sector number *S(K)* are used as the three inputs to switching table as shown in Table-I. To develop the, (i) angle calculation block, (ii) angle conversion block, and (iii) sector number, the algorithm is simulated and depicted in Fig. 3. Angle range conversion block is one of the most important parts of the design. Sector number generator block gives sector number *S(K)*, among six sectors (each π /3 angle wide). [18]

Verification of Simulation

The control scheme developed using FPGA is verified using the hardware co-simulation. It is performed by generating a board support package compatible to the target. Here, the target device is Spartan3e kit, with clock frequency of 50 MHz. Synthesis tool XST and VHDL are used for bit stream generation. Bit stream generated automatically generates the run time block (JTAG), representing the hardware model. This block is added on MATLAB/ Simulink and connected between input and output. The USB cable speed is set at 12 MHz in run time simulation block. RTL schematic view after physical implementation is given in Fig.4. The FPGA time/ area performance of the IVC controller is presented in Table-2.

The consumed resources are obtained for a 16 bit fixed point format, determined after performing hardware co-simulation. There are three parallel execution processes happen. One PI controller and *d-q* transformation are executed within 12 cycles, i.e., 0.24 µs. HCC execution in parallel with the theta calculation and sector generation within 10 cycles, i.e., 0.20 µs. Computation time for switching table is 0.16 µs. so the whole execution time is taken by the IVC controller by the 0.60 µs. the corresponding execution time is therefore 2.8 µs. the digital FPGA based IVC controller can be approximated quite closely to analog one because the effect of sampling and computation delay are very negligible.

Table 1 – FPGA time/area performance

S. No	Module	Latency	Computation Time
1.	PI controller (TP-I)	12	0.24µs
2.	dq to abc (Td-q)	12	0.24 µs
3.	Hysteresis current controller (THys)	10	0.20 µs
4.	Theta calculation (Tac)	6	0.12 µs
5.	Sector generation (Tss)	4	0.08 µs
6.	Switching table (TLT)	8	0.16 µs
7.	AD conversion (TADC)		2.20 µs
Total			2.8 µs
Consumed resources			28%

2. Result

The FPGA implementation of the IVC is tested considering two cases.

1. *Case-I:* Controller design algorithm using XSG is tested and performance of IVC is analyzed under different operating condition.
2. *Case-II:* Comparative performance of IVC, DTC and VC during steady-state and transient-state. The effect of time discretization and delay caused by the sampling of signals is taken into consideration in the simulation.

2.1. Steady State Performance of IVC

To verify the performance of the proposed FPGA based controller modeling for IVC IMD, two case studies have been demonstrated in this section. Case studies describe the dynamic response to the changes in the reference load conditions and the reference speed. Simulations of the control schemes for all the systems have been performed in XSG environment.

A. Case 1: Reference Speed Change: Initially, the reference speed of the motor is 120 rad/sec. This reference speed is decreased at time t = 1.5 sec to 80 rad/sec, and at time t=2.5 sec the reference speed is suddenly increased from 80 rad/sec to 140 rad/ sec. The results obtained are shown in Fig 5(a). It is clearly visible that the drive follows the changes in the reference speed and reaches the steady state quickly with less torque pulsations during transients. Thus, the IVC drive tracks the reference speed effectively.

B. Case 2: Load Torque Change: Load torque of depicts the nature of the load applied on the drive system. The drive should be able to tolerate sudden changes in the load torque. To check the robustness of

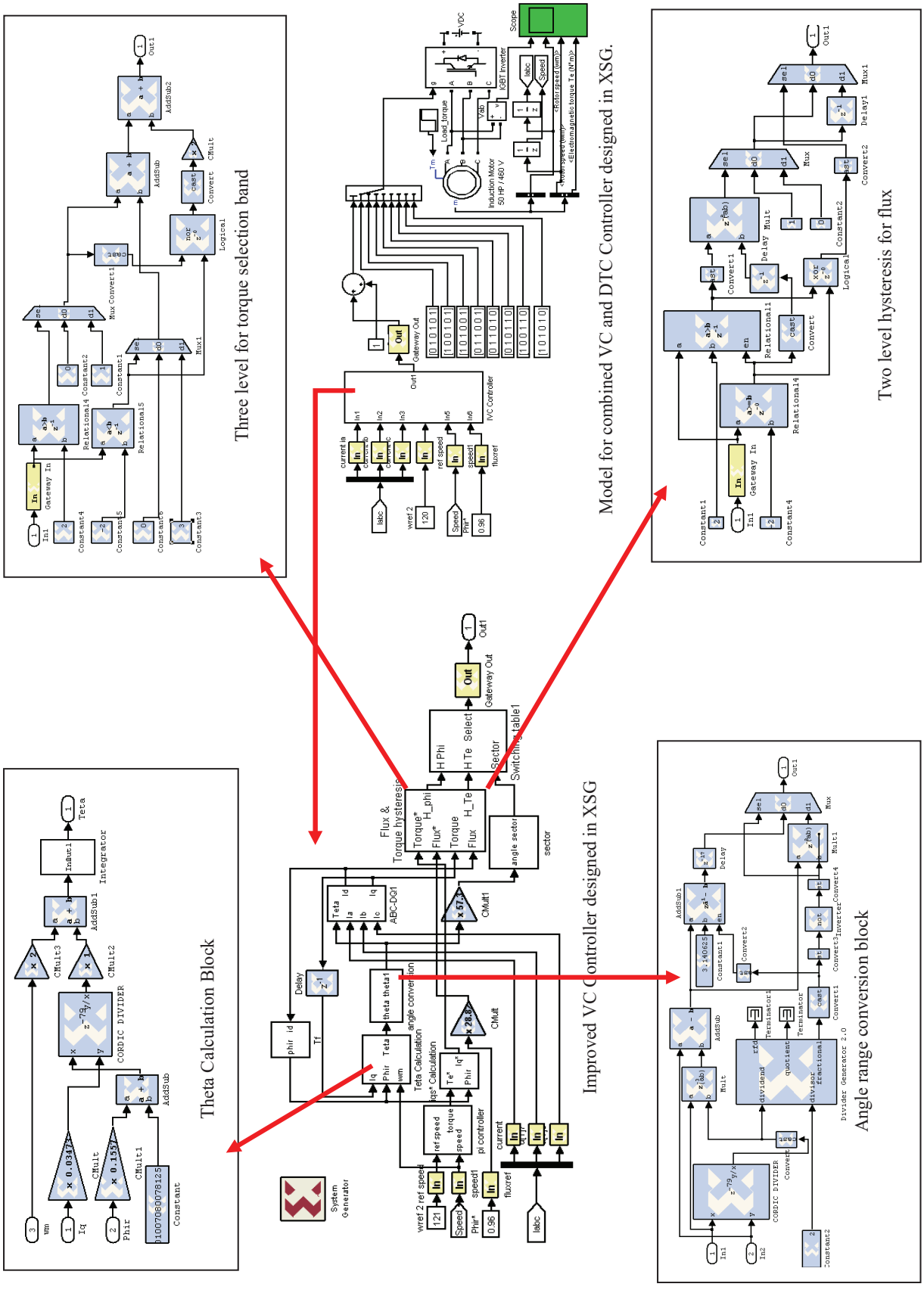

Fig. 3 – Model for combined VC and DTC Controller designed in XSG and its components

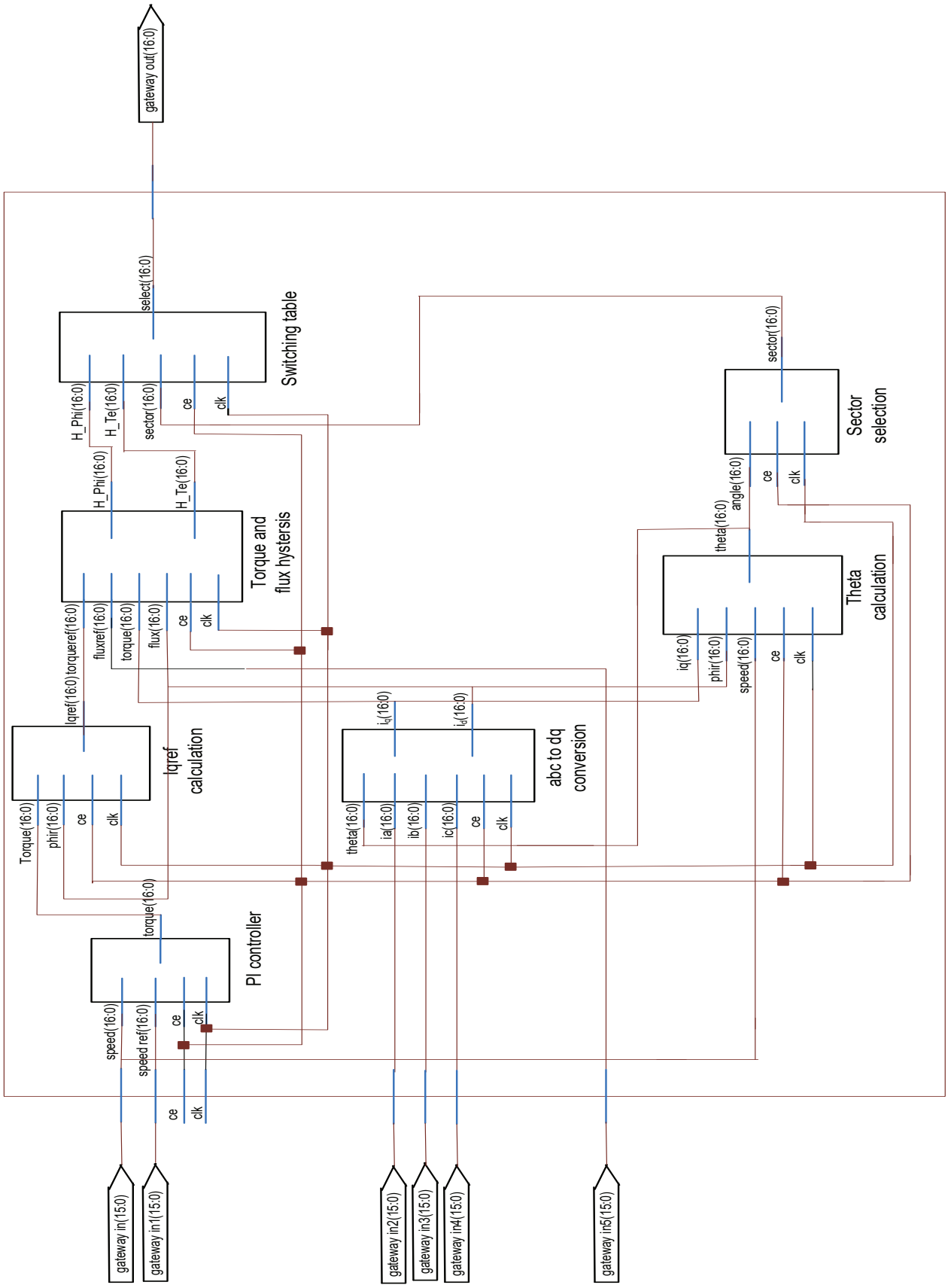

Fig. 4 – RTL schematic view of IVC controller

the proposed scheme, the load torque is varied from no load to 200 N-m at time t = 1.5 sec, and then suddenly decreased from 200 N-m to 150 N-m at time t = 2.5 sec. It is noticeable from the results given in Fig. 5 (b) that the drive follows the load torque and speed of the motor decreases from 120 rad/sec to 110 rad/sec at time t = 1.5 and at time t = 2.5 sec the speed of motor increases from 110 rad/sec to 113 rad/sec.

2.2. **Comparative Performance of IVC**

The steady state performance of IVC, DTC and VC has been compared by evaluating the three phase rms current ripple in different operating conditions. The considered operating condition are related to rotor speed value of 100%, 50% and 10% of the rated value, and torque value of 100%, 50% and 0% of the rated value. The results obtained using IVC, DTC and VC scheme are summarized in table I. The rotor rated speed is 180 rad/sec and the rated torque is 203 N-m. The behavior of IVC scheme is characterized by lower value of the three phase rms current ripple with respect to DTC scheme in all the operating conditions. Under the assumption made of the same mean inverter switching frequency, the amplitude of the torque ripple in DTC higher than that of IVC. But at the same time IVC has approximately same three phase rms current ripple and amplitude of torque ripple with respect to VC.

2.2.1 Transient performance

In transient characteristics load mitigation capability of the three drives at rated torque variation from no load for different operating speed are observed and performance is evaluated in terms of settling time and maximum overshoot. The transient performance of the three schemes has been compared analyzing the response to a step variation of the torque command from 0 Nm to 206 Nm (rated torque), at different rotor speeds. Fig. 6 depicts the torque responses obtained using IVC, DTC, and VC scheme at 180, 90, and 18 rad/sec, respectively. These results show that using the IVC scheme a better torque response can be achieved in terms of settling time and maximum overshoot with respect to VC and less torque ripple with comparison to DTC. The settling times for the three cases are summarized in Table 4. Results confirm that IVC scheme is well capable to provide high performance control of induction machine. All these results are validating our design scheme in XSG for generating the configurable code for FPGA.

Fig. 7 gives the comparative speed for IVC of IMD in Simulink and XSG. The result verifies the

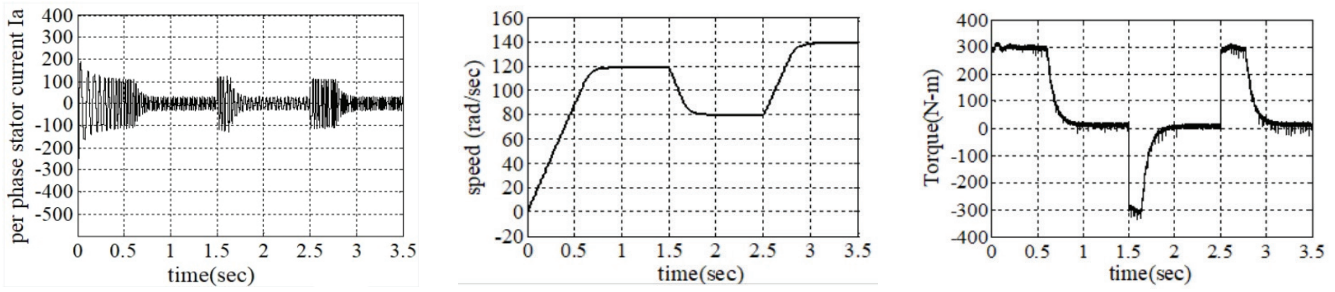

Per phase stator current, I_a Speed (rad/sec.) Torque, N-m

Fig. 5 – Performance of IVC when (a) change in reference speed at time t=1.5 sec and t=2.5 sec.

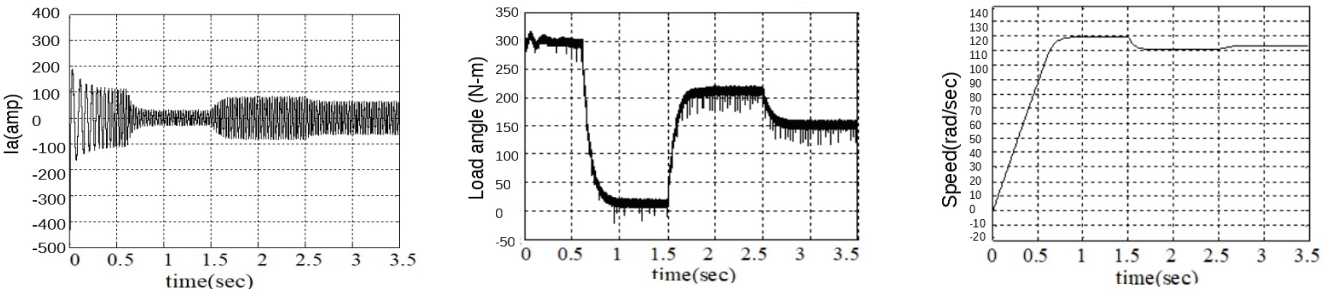

Per phase stator current, I_a Speed (rad/sec.) Torque, N-m

Fig 5 (b) – change in reference load torque at time t=1.5 sec and t=2.5 sec.

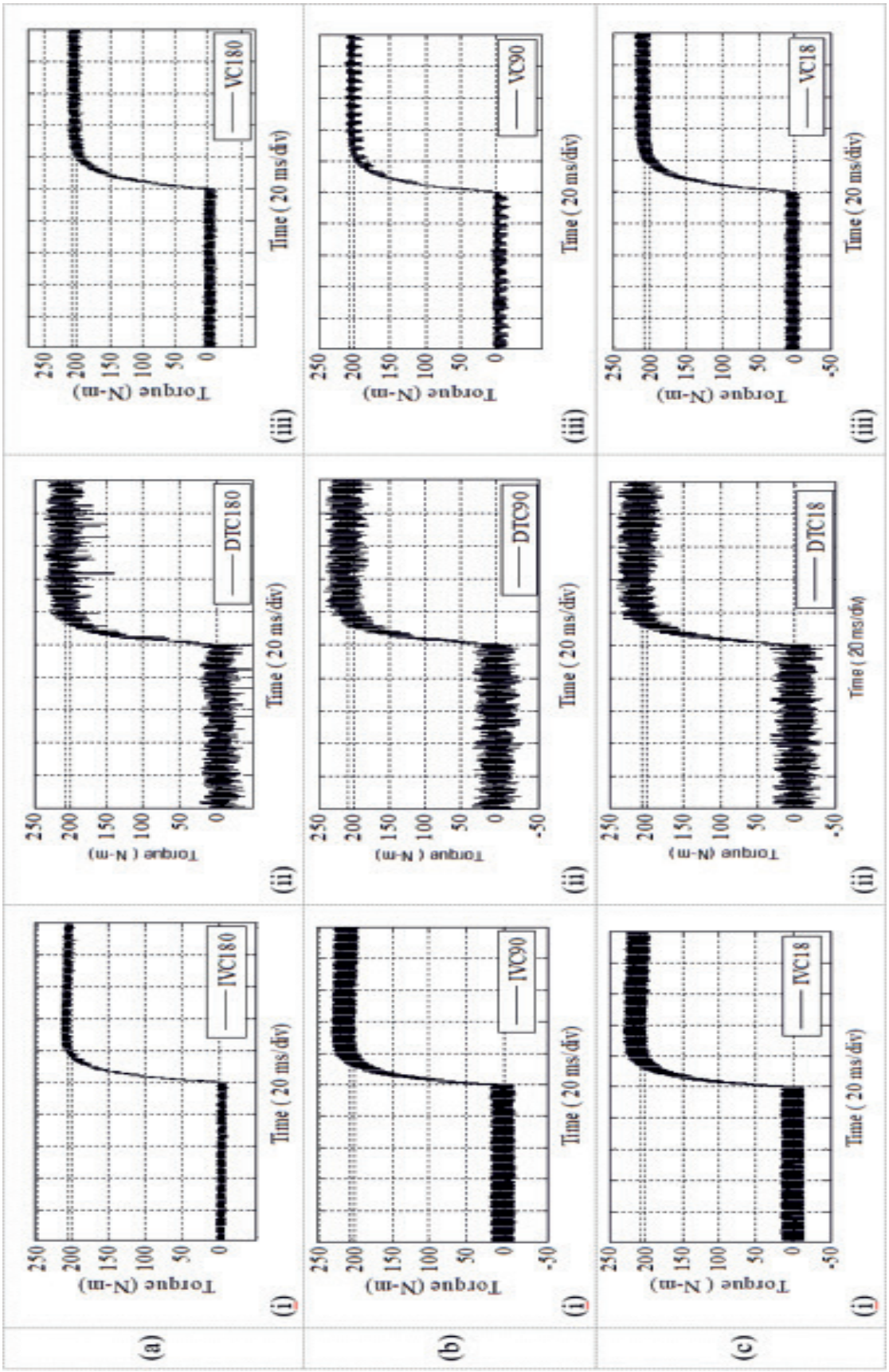

Fig. 6 – Torque response for (i) IVC, (ii) DTC, and (iii) VD at speed of (a) 180 rad/sec. (b) 90 rad/sec., and (c) 18 rad/sec.

Table 3 – Three phase rms current ripple

Torque(N-m)	Speed(rad/sec)								
	180			90			18		
	IVC	**VC**	**DTC**	**IVC**	**VC**	**DTC**	**IVC**	**VC**	**DTC**
206	31.3 A	**9.05** A	9.2 A	34.8 A	**34.6** A	36.7 A	**3.47** A	3.5 A	8.3 A
103	**1.2** A	2.78 A	4.4 A	**21.2** A	21.45 A	**21.2** A	**3.9** A	4.05 A	5.7 A
0	**0.5** A	2.74 A	3.9 A	12.2 A	**11** A	12.2 A	3.5 A	**3.48** A	4.3 A

Table 4 – Settling times for the three cases

	IVC	DTC	VC
180 rad/sec	17 ms	15 ms	30 ms
90 rad/sec	15 ms	14 ms	26 ms
18 rad/sec	14 ms	12 ms	22 ms

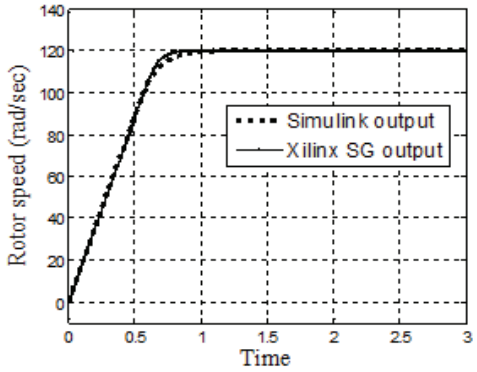

Fig. 7 – Comparison of speed of IVC drive in Simulink and XSG

applicability of the proposed modeling approach of controller using XSG for IVC. The slight difference in response is due to the fact that calculation in XSG is performed using fixed point digit.

Conclusion

The work successfully demonstrates the design and implementation of FPGA based controller design of an IVC IMD using XSG. First, suitability of XSG for FPGA implementation with merits of IVC is presented. Then, the system level modeling with feasibility and block suitability for design is discussed. After, examining some details of IVC, control system architecture using XSG and prototype verification using hardware co-simulation is presented. Finally, the results show the effectiveness of the proposed scheme. Major contributions of this study are:

1) The successful implementation of IVC scheme using XSG.
2) It confirms supremacy of IVC scheme over VC scheme and DTC.
3) It presents a hardware efficient solution for controller design problem.

References

1 D. Casadei, F Profumo, G. Serra, and A. Tani, “FOC and DTC: Two Viable Schemes for Induction Motor torque control” IEEE Trans. on Power Elect., vol. 17, no. 5, pp. 779 – 787, Sept 2002.

2 O. Salari, M. Nouri, K. Hashtrudi Zaad, A. Bakhshai, P. Jain, "Space Vector Modulation for Multi-Source Inverters", Power Electronics and Application Conference and Exposition (PEAC) 2018 IEEE International, pp. 1-6, 2018.

3 P. Wojcik, “Flux control with space vector modulation (FC-SVM)”, in Intl. Conf. On computer as a tool, EUROCON, Warsaw, 9-12 Sept. 2007, pp. 1759 – 1763.

4 Praveen Kumar V. Kunisetti, Thippiripati Vinay Kumar, "Enhanced direct torque control and predictive torque control strategies of an open-End winding induction motor drive to eliminate common-mode voltage and weighting factors", Power Electronics IET, vol. 12, no. 8, pp. 1986-1997, 2019.

5 S. Vaez-Zadeh, E. Jalali, “Combined vector control and direct torque control method for high performance induction motor drives”, *Energy Conv. and Management,* vol. 48, pp. 3095–3101, 2007.

6 M. Cirstea, A. Aounis, M. McCormick, P. Urwin, “Vector control system design and analysis using VHDL” IEEE intl. Conf. PES, Vancouver, BC, 17-21 Jun 2001 pp. 81-84.

7 J. Lis, C.T. Kowalski, T.O. Kowalska, “Sensorless DTC control of the induction motor using FPGA,” Intl. Symp. On Indust. Electronics, June 30- July 2, 2008, pp. 1914 – 1919.

8 L. Idkhajine, E. Monmasson, M. W. Naouar, A. Prapa, K. Bouallaga, “Fully integrated FPGA – based controller for synchronous motor drive,”

9 *IEEE Trans. Ind. Electron.*, vol. 56, no. 10, pp. 4006–4017, Oct. 2009.

10 L. Idkhajine, E. Monmasson, M. W. Naouar, A. Prapa, K. Bouallaga, “Fully integrated FPGA – based controller for synchronous motor drive,” IEEE Trans. Ind. Electron., vol. 56, no. 10, pp. 4006–4017, Oct. 2009.

11 Deepak Chenumalla, Venkat Kishore Garimella, Amarendra Gangavarapu, "Modelling and simulation of synchro and synchro-to-digital converter for electrical motor drives", Science Measurement & Technology IET, vol. 10, no. 1, pp. 58-68, 2016.

12 Y. Y. Tzou and H. J. Hsu, “FPGA realization of space-vector PWM control IC for three-phase PWM inverters,” IEEE Trans. Power Elec., vol. 12, no. 6, pp. 953–963, Nov. 1997.

13 Francesco Ricci, Hoang Le-Huy, “Modeling and simulation of FPGA-based variable-speed drives using Simulink”, *Mathematics and Computers in Sim.*, vol. 63, pp. 183–195, 2003.

14 Hwang, J., Milne, B., Shirazi, N., and Stroomer, J.D.: ‘System level tools for DSP in FPGAs’, Lect. Notes Comput. Sci., 2001.

15 *System Generator User Guide*, Xilinx, San Jose, release 10.1 March, 2008.

16 *Foundation ISE User Guide*, Xilinx, San Jose, CA, 2005.

17 D. Telford, M. W. Dunnigan, and B. W. Williams, “A comparison of vector control and direct torque control of an induction machine,” in *Proc. IEEE PESC*, 2000, pp. 421–426.

18 H. Le-Huy, “Comparison of field-oriented control an direct torque control for induction motor drives,” in Proc. 34th IEEE IAS Annu. Meeting Conf., Oct. 3–7, 1999, vol. 2, pp. 1245–12.

Journal of the Maharaja Sayajirao University of Baroda: Science & Technology
Vol. 57, 2023, pp. 23-27

Synthesis, Characterization and Structural Properties of Pr^{3+} Doped TiO_2 Nanoparticles for Photo-Catalytic and Anti-Microbial Properties

K.R. Venkatesha Babu[1], M. Vishwas[1,*], Sheema Kauser [2], Rajeshree Patwari D[1], L.A. Sathish[1], K.S. Hemalatha[3]

[1]Department of Physics, Nrupathunga University (GSC), Bangalore-560 001, India
[2]Department of Microbiology, Nrupathunga University (GSC), Bangalore-560 001, India
[3]Department of Physics, Maharani Cluster University (MSCW), Bangalore-560001, India.

Undoped and praseodymium (Pr^{3+}) doped titanium dioxide (TiO_2) nanoparticles (NPs) were obtained from titanyl nitrate via self-propagating solution combustion method (SCM) at low temperature using a muffle furnace **with eco-friendly Brassica Oleracea leaf extract used as a fuel/reducing agent for the reaction**. The structural characterization of the undoped and Pr^{3+} doped NPs was performed using powder x-ray diffraction (PXRD) studies. The microstructure and surface morphology of the nanoparticles were studied using scanning electron microscope (SEM). Raman studies elucidated the vibrational modes of TiO_2 and the presence the dopant in the host. The photo catalytic and anti-microbial activities of the pure and Pr^{3+} doped NPs were investigated. The results reveal that in both un-doped and doped samples, no growth being observed in Gram positive bacteria: ***Staphylococcus aureus,*** **Gram negative*: Pseudomonas aeruginosa, Salmonella typhi and*** **Yeast:** ***Candida albicans.***

Keywords: TiO_2: Pr^{3+}; XRD; SEM; Photocatalytic activity; anti-microbial activity.

1. INTRODUCTION

Pure and Pr^{3+} doped TiO_2 NPs has great potential for facilitating the development of novel biomedical applications as well as photo-catalysis, optical and electrical applications, etc [1-3]. Over the years, bacteria have developed resistance to wide range of antibiotics, leading to an emergence of different infections and diseases. Treatment of these disorders is getting increasingly complex. As a result, a deliberate effort was made to study how effective TiO_2: Pr^{3+}(5% mol) NPs prepared by Brassica Oleracea leaf extract using green synthesis route were against the bacteria and yeast. As a result of urbanisation and commercialization, industrial effluents and certain organic dyes are being discharged into the aquatic systems. Organic dyes are generally implemented as dye stuff in major industries, notably fabrics, tanning, and paper mills. These extremely toxic, carcinogenic, and non-degradable organic dyes can cause significant health problems in people, especially skin ailments, cancer, allergic reactions and mutation. For this effect, numerous water purification procedures such as sedimentation, aggregation, electrolysis, and chemical precipitation, oxidation and reduction reactions have been studied in the treatment of industrial sewage effluents. As a consequence, a cost-effective and environmentally sustainable technique for the degradation of an organic pollutant from wastewater is essential.

2. MATERIALS AND METHODS

2.1 Materials

The broths namely: Potato Dextrose (PD) and Luria Bertani (LB), the agar media namely PD, EMB, nutrient, sterile discs and swabs, cultures of *Candida albicans*, *Pseudomonas aeruginosa, Salmonella typhi* and *Staphylococcus aureus* and antibiotic Streptomycin were used. Ethanol, sulphuric acid, hydrochloric acid, nitric acid, praseodymium, titanium (IV) butoxide and ammonium acetate of analytical grade chemicals were used. Methylene blue (MB) was used as a stain and glycine as source of fuel. Muffle furnace, autoclave, sonicator, incubator, laminar air flow, UV transilluminator, water bath and oven were the instruments used.

*Corresponding author.
Email: vishwasm46@yahoo.com

2.2 Method of Preparation TiO_2: Pr^{3+} (5 mol %)

Pure and doped TiO_2 NPs were prepared from titanyl nitrate and praseodymium nitrate employing an environmental friendly leaf extract (Brassica Oleracea) as a reducing agent by solution combustion methodology at low temperature (≈ 450 °C) with suitable stoichiometry computations. After self-propagating combustion, a black colored ash was obtained. The obtained powder was finely grounded and calcinated for 2 h at 700 °C to remove impurities. The undoped and Pr^{3+} doped TiO_2 samples thus obtained were tested for photo-catalytic and anti-microbial activities.

2.3 PXRD studies

X-ray diffraction studies reveal crystallinity, phase and purity of the sample. Crystallite size, unit cell variables and other structural parameters were also were estimated. Sharp, well defined peaks in PXRD shown in Fig.1 suggest the crystallinity, phase, and purity of the prepared sample. The PXRD data was matched with JCPDS data for anatase phase of TiO_2 and confirmed the card number as 84-1286 [4], indicating the phase of sample was anatase. Employing Scherrer's formula [5] represented in equation (1), the crystallite size was estimated to be 46 nm. All the spikes were designated with (h k l) values as shown in the Fig.1. The calculated cell parameters were noticed to be a=b=3.76 Å and c=9.43 Å were in agreement with standard values a=b= 3.7822 Å and c=9.5 Å.

$$D = \frac{k\ \lambda}{\beta\ \cos\theta} \qquad (1)$$

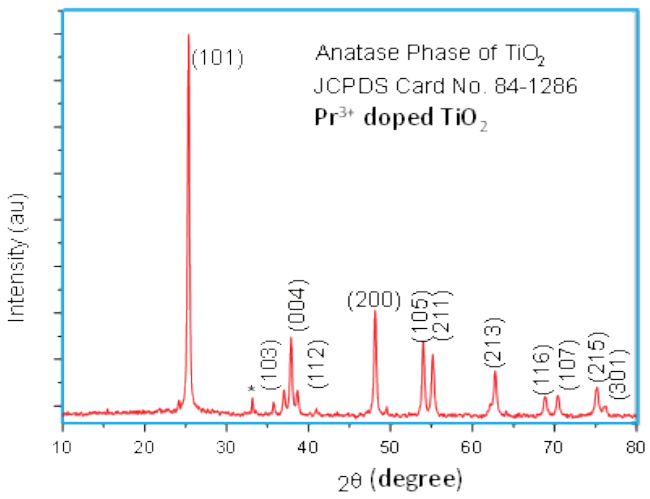

Fig. 1 – PXRD patterns of Pr^{3+} doped TiO_2 NPs.

where k be Scherrer factor (0.89 for spherical particles), λ be the wavelength (1.54 Å) and as the full width at half maximum (FWHM). High value of texture coefficient (TC) ≈0.5 for (2 1 3) plane confirms that the majority of planes are oriented along this. Other methods namely: Williamson-Hall (WH) and Nelson-Riley (NR) plots were also used to find the crystallite size, the observations were found to be 42 nm and 56 nm respectively, confirming nano size.

2.4 Surface morphology

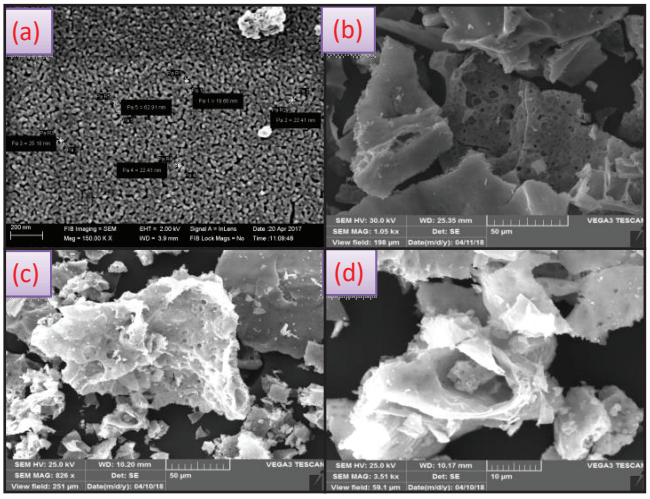

Fig. 2 (a-d) FESEM images of the pure and doped

NPs at different concentration and resolution (a) Pure TiO_2 (b) 1 mol% (c) 9 mol% at 50 m (d) 9 mol% at 10 µm.

Images in the Fig. 2 (a-d) show the surface appearance of the sample using FESEM for pure and doped TiO_2 at different concentrations and resolutions. Fig. 2(a) shows the images of pure TiO_2 with average grain size of 20 nm, with large agglomeration at a higher resolution. Fig. 2 (b) depicts flake shapes for 1 mol% doped TiO_2 NPs at lower resolution. Fig. 2(c) were the images for 9 mol% Pr doped TiO_2 NPs indicating cone shapes but at 10 µm resolution shows flowers. The large number of pores in the Fig. 2(b) and 2(c) are the indications of the large gases released during the process of synthesis.

2.5 Raman studies

The Raman studies were performed and shown in the Fig. 3 for pure and doped (5 mol%) TiO_2 NPs. The intensity was measured at RT in the range of 98 - 850 cm^{-1}. The absorption peaks reported for pure TiO_2 at 141, 446 and 608 cm^{-1} was owing to active

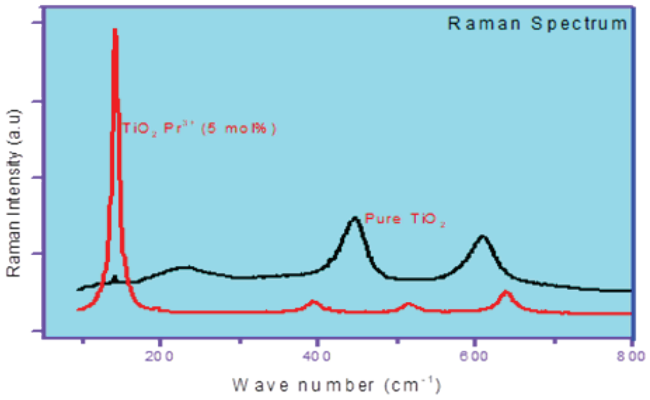

Fig. 3 – Raman spectra of the un-doped and Pr^{3+} doped TiO_2 NPs.

vibrational modes (optical phonon modes) B_{1g}, E_g and A_{1g} sequentially. There is a shift in the peak position with fall in intensity of the peaks due to doping effect. The new peak position for the doped NPs were noticed at 229, 446 and 608 cm^{-1} were due to confinement of phonons. Dhanalakshmi et al. [6] reported that, with increase of weight percent of rare earth (Ce) ions in TiO_2, the intensity of all the peaks decreased and the high intense Raman peak slightly shifted towards the higher wave number side.

2.6 Photo catalytic degradation

The photo catalytic activity of undoped and Pr^{3+} doped TiO_2 NPs was investigated by photo-degradation of MB dye under UV lamp. The time dependent fall in the intensity of absorption band of MB dye was noticed after the adding Pr^{3+} doped TiO_2 NPs in appropriate proportions. The photo catalytic degradation efficiency was observed at a wavelength of 664 nm by UV-Vis spectrophotometer. Here, MB concentration of 10 mg/L was mixed with 10 mg dosages of photo-catalyst and the observations were done under UV light. The amount of degradation of MB dye increased linearly with time under UV irradiation as shown in the Fig. 4 (a). The concentration of dye (C/C_o) with time, where C_o is the initial concentration when time t=0 is shown in Fig.4 (b). The concentration of dye after 100 minutes of irradiation was found to be 92, 69 and 51 percent, respectively for blank, pure TiO_2 and Pr^{3+} doped TiO_2 NPs. Xu et al. [7] reported the photocatalytic degradation of Rhodamine B (RhB) and 2,4-dichlorophenol (2,4-DCP) dyes using un-doped and Pr^{3+} doped $Bi_2Sn_2O_7$ NPs under visible light irradiation and found that Pr^{3+} doped NPs exhibited enhanced photocatalytic activity compared to un-doped NPs. Cordeiro et al [8] reported the photo-catalytic degradation of bisphenol-A (BPA) using un-doped and Pr^{3+} modified TiO_2 NPs under visible light and found an enhancement in the photo-catalytic activity with the Pr^{3+} modified TiO_2 NPs.

3. Anti-microbial activity

The synthesized TiO_2:Pr^{3+} (5 mol%) NPs were investigated for antimicrobial activity against fungus, Gram – ve bacilli, and Gram +ve cocci. The minimum inhibitory concentration (MIC) of the sample was checked by the well diffusion method. For *Candida albicans* (MTCC 3958) Potato dextrose broth was used, Luria Bertani (LB) was prepared for *Pseudomonas*

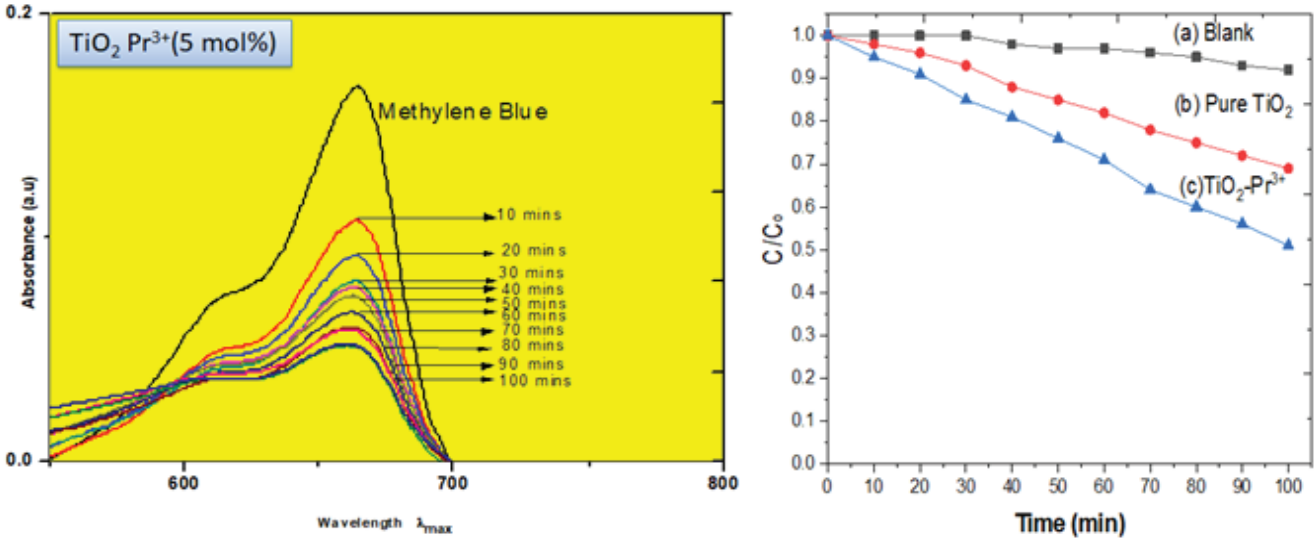

Fig.4: Photo catalytic degradation of undoped and Pr^{3+} doped TiO_2 NPs
(a) absorbance versus wavelength (nm), (b) degradation (C/C_o) versus time.

aeruginosa (MTCC 2453), *Salmonella typhi* (MTCC 735) and *Staphylococcus aureus* (MTCC 96). MTCC 3958 was incubated at 25 °C for 72 h, whereas MTCC 2453, MTCC 735, and MTCC 96 were incubated at 37 °C for 24 h.

3.1 Preparation of samples

10 mg of doped TiO_2 and control (Streptomycin) were dissolved in 1mL of dimethyl sulfoxide (DMSO) Different aliquots of our sample were prepared by pipetting 10µL (100 µg), 20 µL (200 µg), 30 µL (300 µg) and 40 µL (400 µg) and the final volume was made up to 50 µL by adding DMSO.

3.2 Media preparation for MIC

For the fungal culturing, 100 ml of PD Agar was prepared and 500ml of LB Agar was prepared for the bacterial culturing. Both the media were autoclaved at 121 °C and 15 lbs PSI for 20 min along with the Petriplates.

3.3 Plating for MIC against organisms

To the sterile petriplates, 25 mL of the media (PDA and LB agar) was poured and allowed to set. Into each of the plates, 200 µL of inoculum (*Candida albicans, Pseudomonas aeruginosa, Salmonella typhi, and Staphylococcus aureus*) was inoculated by spread plate technique. With the corkborer five wells of 0.6 cm diameter were bored. To these 50µL of doped samples containing 100 µg, 200 µg, 300 µg and 400 µg were dispensed into the respective wells, 50 µL of DMSO at the center as blank. The inoculated fungal plates were incubated at 25 °C for 72 h, whilst the bacterial plates were incubated at 37 °C for 24 h. These plates after incubation were observed for the zone of inhibition indicating microbial activity.

3.4 Observation

The NPs did not inhibit the growth of neither the fungus (*Candida albicans)* nor the bacteria both Gram positive and Gram negative as no inhibition zone was observed around it. The control (Streptomycin) inhibited the growth to a large extent (Clear zone observed). Therefore, it can be inferred that, the activity of TiO_2 nano particles is limited hence it cannot be used as an effective antimicrobial agent as indicated in by the studies carried out. In the Fig. 5, the nano particles directed towards *Candida albicans* at 400 µg show insignificant inhibitions. As seen in the Fig. 6, no zone of inhibition by nano particles was observed against the Gram negative bacteria (*Pseudomonas aeruginosa)*. As indicated in the Fig. 7, no observance of clear zone the plates inoculated with *Salmonella typhi-Gram* negative bacterium. The nano particles did not show any activity against *Staphylococcus aureus*-Gram positive bacterium as indicated in Fig. 8. The control (streptomycin) showed encouraging inhibition against all four microorganisms namely *Candida albicans*, *Pseudomonas aeruginosa, Salmonella typhi* and *Staphylococcus aureus*. Zeeshan Ali et at [9] reported the study on antimicrobial activity and zone of inhibition of pure and cerium (Ce) doped TiO_2 nanoparticles on E. coli strain and found that Ce doped TiO_2 nanoparticles possess high bactericidal activity confirmed by Colony Forming Unit (CFU) and Kirby-Bauer (KB) method with and without TiO_2 nanoparticles inoculated on LB agar. Schutte-Smith et al. [10] reported the antiviral and antimicrobial properties of TiO_2 NPs in paints and coatings under visible light to prevent the spread of pandemic diseases in the future. Ahrens et al [11] reported the incorporation of TiO_2 NPs into a cellulose-reinforced melamine-formaldehyde resin (MF) to obtain a

Fig. 5 – Effect of Pr^{3+} doped TiO_2 against *Candida albicans*

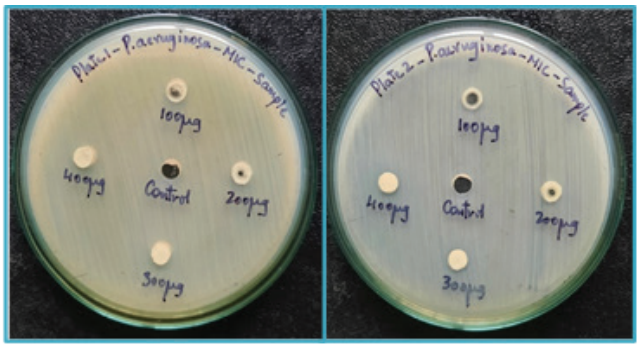

Fig. 6 – Effect of Pr^{3+} doped against *Pseudomonas aeruginosa*

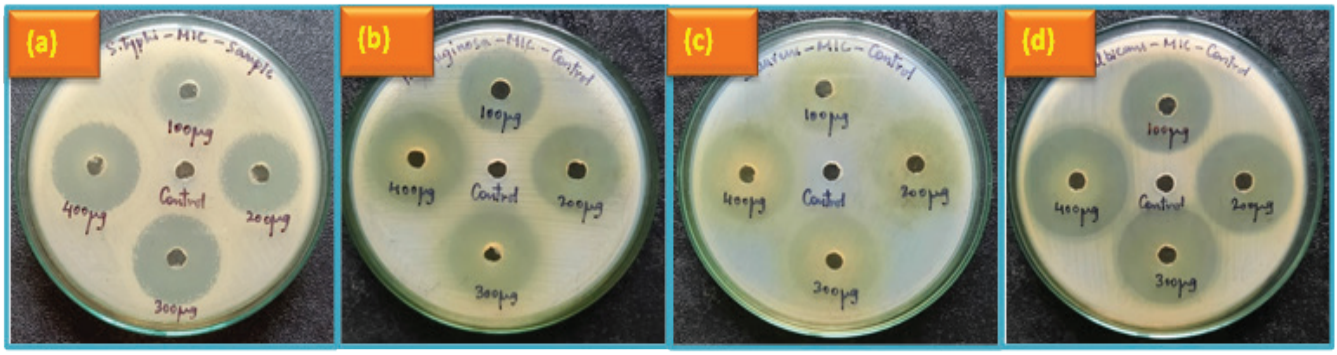

Fig. 9: Antimicrobial activity of control on:
(a) *Salmonellatyphi,* (b) *PseudomonasAeruginosa,* (c) *Staphylococcusaureus,* (d) *Candidaalbicans*

photocatalytic antimicrobial thermoset, to study the photocatalytic activity TiO_2 NPs using methylene blue dye and antimicrobial surface activity of the modified MF against E. coli and showed that, a complete reduction in E. coli after UV irradiation for 2 h.

4. Conclusions

The synthesized, Pr^{3+} doped TiO_2 NPs were examined by several procedures prior to getting tested for photocatalytic degradation under UV light and anti-microbial activities. The sample has shown to be more useful for photo-catalytic degradation rather than antibacterial action where the growth of the fungus and the bacteria continued and remained uninhibited.

References

1 D. Casadei, F Profumo, G. Serra, and A. Tani, "FOC and M. Vishwas, Sudhir Kumar Sharma, K. Narasimha Rao, S. Mohan, K.V. Arjuna Gowda, R.P.S. Chakradhar, Optical, dielectric and morphological studies of Sol-Gel derived nanocrystalline TiO_2 films, Spectrochim. Acta Part A. 74 (2009) 839-842.

2 K.S. Shamala, M. Vishwas, Influence of substrate temperature on optical, structural and dielectric properties of TiO_2 thin films prepared by spray pyrolysis technique, Mat. Today: Proc. 52 (3) (2022) 1344-1347.

3 M. Vishwas, K. Narasimha Rao, D. Neelapriya, Ashok M. Raichur, R.P.S. Chakradhar, K.Venkateswarulu, Effect of TiO_2 nano-particles on optical, electrical and mechanical properties of poly (vinyl alcohol) films, Proceedia Materials Science. 5(2014)847– 854.

4 S. Priatmoko, E. Widhihastuti, N. Widiarti, D. Subagja, Synthesis of Ni/NiO-TiO_2 using sol-gel method and its activity in blue methylene degradation, Journal of Physics: Conference Series. 1918 (2021) 032013.

5 M. Vishwas, Sudhir Kumar Sharma, K. Narasimha Rao, S. Mohan, K.V. Arjuna Gowda, R.P.S. Chakradhar, Sol-gel synthesis, characterization and optical properties of TiO_2 thin films deposited on ITO/ glass substrates, Modern Physics Letters B. 24 (2010) 807-816.

6 J. Dhanalakshmi, S. Iyyapushpam, S. T. Nishanthi, M. Malligavathy, D. P. Padiyan, Investigation of oxygen vacancies in Ce coupled TiO_2 nanocomposites by Raman and PL spectra, Adv. Nat. Sci.: Nanosci. Nanotechnol. 8 (2017) 015015.

7 W. Xu, G. Zhou, J. Fang, Z. Liu, Y.F. Chen, C. Cen, Synthesis and Characterization of Pyrochlore $Bi_2Sn_2O_7$ Doping with Praseodymium by Hydrothermal Method and Its Photocatalytic Activity Study, International Journal of Photoenergy. 2013 (2013)234806.

8 Denise S. Cordeiro, Fernando L. Cassio, Larissa Ciccotti, Thiago L. R. Hewer, Paola Corio, Renato S. Freire, Photocatalytic activity of Pr-modifed TiO_2 for the degradation of bisphenol ASN Applied Sciences. 3 (2021) 258.

9 Zeeshan Ali, Bharat Raj, M. Vishwas, M. Anisa Athhar, Synthesis, characterization and antimicrobial activity of Ce doped TiO_2 nanoparticles, Int. J. Curr. Microbiol. App. Sci. 5(4) (2016) 705-712.

10 M. Schutte-Smith, E. Erasmus, R. Mogale, N. Marogoa, A. Jayiya, H. G. Visser, Using visible light to activate antiviral and antimicrobial properties of TiO_2 nanoparticles in paints and coatings: focus on new developments for frequent-touch surfaces in hospitals, J Coat Technol Res. 20(3) (2023) 789–817.

11 Markus Ahrens, Theresa Fischer, Nina Zuber, Serhiy Yatsenko, Thomas Hochrein, Martin Bastian, Markus Eblenkamp, Petra Mela, Antimicrobial activity of a titanium dioxide additivated thermoset, Catalysts. 12 (2022) 829.

Journal of the Maharaja Sayajirao University of Baroda: Science & Technology
Vol. 57, 2023, pp. 28-41

Critical Assessment and Comparative Analysis of Widely Used Exchange-Correlation Functionals: A Comprehensive Review Across Diverse Properties

Apeksha Gauswami, Jay Panchal and Prafulla K. Jha*

Department of Physics, Faculty of Science, The Maharaja Sayajirao University of Baroda, Vadodara, Gujarat, India-390002
*E-mail: prafullaj@yahoo.com.

The ground-state energy and density of a many-electron system are frequently computed using Kohn-Sham density functional theory. While exact in principle for the ground-state energy and electron density, Kohn-Sham density functional theory necessitates, in practice, an approximation for the exchange-correlation energy within the density functional. Common approximations can be visualized as rungs on a ladder, with higher rungs being more complex to formulate and apply, yet potentially greater accuracy. Each rung introduces an additional component to the energy density. Progressing from the bottom to the top, these rungs involve: the local density approximation (LDA), the generalized gradient approximation (GGA), the meta-Generalized gradient approximation (meta-GGA), the hybrid functional and the double hybrid functional. LDA, GGA and meta-GGA suffer from certain fundamental shortages, particularly the band gap problem. This problem was solved in hybrid functional methods which have saved significant interest as a relatively cost-effective approach to address the challenges posed by LDA/GGA. Although early hybrid functionals employed fixed parameters derived from either fitting standard experimental databases or theoretical considerations, recent research has clearly proved that the hybridization parameters possess physical significance and hence should be personalized to the specific system. This article aims to provide a systematic overview of exchange-correlation functionals, outlining various strategies and reviewing significant methodological advancements in recent years.

Keywords: Kohn-Sham density functional theory, Jacob's ladder, Exchange-correlation energy, Kinetic energy density, The random phase approximation.

1. Introduction

Density functional theory (DFT) represents valuable and predicting equipment for the calculating electronic structure of atoms, molecules, solids and other extended systems [1–3]. This theory is most widely used based on the Kohn-Sham density functional theory (KS-DFT) and it reduces the many-electron ground state problem to a computationally compliant self-consistent one-electron problem [4,5]. Hence, approximate DFT has become the main focus of modern computational chemistry and materials science. This success also lies in the development of increasingly high-performance density functional approximations (DFAS) [6]. Consequently, the exchange-correlation contribution to total energy is represented by DFT, which being unknown, it must be approximated [7]. The exchange-correlation energy (E_{XC}) is usually split into two distinct parts, exchange term (E_X) and correlation term (E_C) [8,9]. The exchange term arises due to the fact that two electrons with the same spin cannot occupy the same point in space, while the correlation term arises due to the coulomb repulsion between two electrons due to their same charge. It can be express as:

$$E_{XC}[n] = E_X[n] + E_C[n] \quad \text{....1)}$$

Here, the term E_X and E_C are the functional of electron density, which can be combined to form E_{XC}. These functionals are called the exchange functional and the correlation functional, respectively [10].

The exchange-correlation functionals, both the old and newly proposed ones, are positioned within rungs 1 to 5 of Jacob's ladder in the density functional theory hierarchy, as outlined by John Perdew [8,11]. By ascending the rungs of Jacob's ladder, the functional's form becomes more complex, resulting in more accurate energies at the cost of increased computational expense [12,13].

Now, we'll see one by one the rungs of Jacob's ladder, Local density approximation (LDA) the 1st rung, Generalized gradient approximation (GGA) 2nd rung, Meta-generalized gradient approximation (m-GGA)

*Corresponding author.
Email: prafullaj@yahoo.com

3rd rung, hybrid functionals 4th rung and the last double hybrid functionals 5th rung [11–14]. In this panel, each rung contributes some new terms to design elements and creating a more aesthetic design.

We shall start with LDA in section 2.1, it has been found as the most useful in calculating the electronic structure of solids and it is simple way to represent exchange-correlation (XC) functional. Kohn and Sham (in 1965) also gave an approximate expression for the XC functional, known as the local density approximation [15–18]. The influences of the electron density (n(r)) on the exchange-correlation energy at a given point in space is limited to LDA.

In section 2.2, we briefly discuss about the generalized gradient approximation (GGA) [19–21], its derivative and examples. Based on LDA, Perdew and Wang proposed in 1986 that in addition to electron density n(r), the exchange-correlation energy of the system also depend on the density gradient ∇n(r). At present, LDA and GGA have been widely used in the calculation of solid physics and material chemistry and have achieved great success.

Next, we will see the third rung of Jacob's ladder in section 2.3, it's a meta-generalized gradient approximation (m-GGA). The Laplacian (second derivative) of the density (∇^2n(r)) or the kinetic energy density (τ(r)) is a key element of meta-GGA functional, addition to the density and the magnitude of the gradient of the density. A non-empirical meta-Generalized Gradient approximation has been specifically made for molecules and solids [22,23].

Then we proceed further, next we would like to introduce a very successful functional for density functional calculations of molecular structure, properties, thermochemistry, kinetics and spectroscopy, the functionals on the fourth rung of Jacob's ladder, the hybrid density functionals [24]. Although hybrid functionals are not completely DFT functionals but they do have exact Hartree-Fock calculations. We will discuss it in detail in section 2.4 with the well-known examples.

The highest rung of Jacob's ladder features functionals that make use of not only occupied, but also unoccupied orbitals. Alongside methods such as MP2 or the random phase approximation (RPA), these functionals are referred to as double hybrid functionals. These double hybrids (DH) represent the most computationally expensive density functionals, yet they also offer exceptional precision. [25].

In the past many comparative studies of the Jacob's ladder have been done, but they are limited to any such systems or particular properties. But no work has been done as of containing different systems and different properties and compared it with experimental value. So, we did that in this work and we also determined what specific additional mathematical requirements can be met at each level and discuss how functionals at each level can be built without any empirical input.

2. Theory and discussions

2.1. Local density approximation (LDA)

The local density approximation was the initial approximation to attain the exact form of exchange-correlation functionals. It was formulated by W. Kohn and L. J. Sham in 1965 [26]. This approach proves highly effective for precise calculations of the electronic structure of materials. The approximation postulates that the electron density exhibits gradual variation throughout space. As a consequence, it hypothesizes that the electron gas within a small volume element d^3r can be approximated as locally uniform. Consequently, the exchange-correlation energy becomes depending on the electron density of the homogeneous electron gas at that specific locality. This approximation implies that if the exchange-correlation energy (E_{XC}) value for a particular particle at a given point is ε_{xc}(n), then the corresponding E_{XC} value for the entire volume d^3r becomes $\varepsilon_{xc}(n(r))n(r)d^3r$. And therefore, the E_{XC} of the LDA can be written as

$$E_{XC}[n] = \int \varepsilon_{XC}\big(n(\vec{r})\big)n(\vec{r})d^3r \quad ....2)$$

While, the total energy is written as,

$$E = \sum_i \varepsilon_i - \frac{e^2}{2}\iint \frac{1}{4\pi\varepsilon_0}\frac{n(\vec{r})n(\vec{r}')}{|\vec{r}-\vec{r}'|}d^3r d^3r' + \int \Big(\varepsilon_{xc}\big(n(\vec{r})\big) - \mu_{xc}\big(n(\vec{r})\big)\Big)n(\vec{r})d^3r$$

In 1976, O. Gunnarsson and B. I. Lundqvist introduced the concept of spin density formalism (SDF) to the local density approximation, leading to the development of what is now known as the local spin density approximation (LSDA) [27]. The XC energy of LSDA is written as,

$$E_{xc}^{LSDA}[n_\uparrow(r), n_\downarrow(r)] = \int n(r)\ \varepsilon_{xc}^{hom}[n_\uparrow(r), n_\downarrow(r)]dr \quad ....3)$$

The LDA/LSDA is expected to yield accurate outcomes under circumstances where the electron density exhibits gradual variation, as previously mentioned. These approximations offer precise ground

state geometries, accurate representation of physical trends and highly precise bond lengths. Nevertheless, there are certain limitations to the LDA/LSDA. They tend to underestimate the bandgap in semiconductors, overestimate adsorption energy and underestimate diffusion barriers. Additionally, their performance is suboptimal in materials where weak hydrogen bonds or van der Waals interactions play a significant role.

2.2. Generalized gradient approximation (GGA)

The second rung of Jacob's ladder is represented by the Generalized Gradient Approximation, which can be tailored to fulfill various sets of precise constraints [28]. However, there exists a certain level of unsuitability linked to the constrained nature of GGA. While it is feasible to meet a subset of potential constraints, achieving the fulfillment of all these constraints using a single GGA is not possible. Hence, it becomes necessary to carefully choose the specific constraints to be satisfied.

Typical molecular systems often deviate significantly from a uniform electron gas. In fact, every real system displays dimensional non-uniformity, meaning it possesses a spatially varying density denoted as n(r) [11]. Generalized Gradient Approximation methods are employed to consider this phenomenon, combining dependence of exchange and correlation energies not exclusively on density, but also on another factor: the gradient of density, represented as ∇n(r) [21,29,30].

When the gradient of the electron density is added to the XC functional, it leads to improved accuracy in describing systems with varying electron densities and better accounts for effects like bond breaking, molecular geometries, and surface properties. GGA functionals take the form:

$$E_{XC}^{GGA}[n\uparrow, n\downarrow] = \int d^3r\, f(n\uparrow(r), n\downarrow(r), \nabla n\uparrow, \nabla n\downarrow) \quad \ldots.4)$$

GGAs are standard for providing improved total energies, atomization energies, structural energy differences and energy barriers. In the solid-state materials, the lattice constants obtained through expanded GGA approaches can occasionally be more accurate than those yielded by the Local Density approximation. (See table 1).

A well-known GGA is the Perdew–Burke–Ernzerhof (PBE) approximation. The PBE approximation accurately gives back the second-order gradient expansion for correlation when dealing with slowly varying densities. Another GGA variation, known as PBEsol (PBE for solids) goes beyond PBE by accurately reinstating the second-order gradient expansion not only for the correlation energy but also for the exchange energy across a broad spectrum of slowly varying densities [28].

The second-order density-gradient expansion can be employed to formulate a first-principles numerical GGA that characterizes the exchange-correlation hole surrounding an electron in a system with a gradually changing density. This approach involves eliminating the undesirable long-range components of the hole to follow the sum rules governing the exact hole behavior. The Perdew-Wang 1991 (PW91) functional represents an analytical approximation to this numerical GGA. In cases where density variations are either gradual or minor, PW91 converges to the second-order gradient expansion. Above, we address this issue by presenting a straightforward and new derivation of a GGA functional. Remarkably, all parameters employed in this functional are fundamental constants. While the derivation depend on just on the fundamental characteristics of the real-space construction that supports PW91 [19,21], the resulting functional closely approximates the numerical GGA.

The exchange-correlation energy of a many-electron system has a spin-density gradient expansion [20,31],

$$E_{xc} = \int d^3r\, n\epsilon_{xc}(n,\xi) + \int d^3r\, [C_{xc}^{\uparrow\uparrow}(n,\xi)|\nabla n\uparrow|^2/n_{\uparrow}^{\frac{4}{3}} + C_{xc}^{\downarrow\downarrow}(n,\xi)|\nabla n\downarrow|^2/n_{\downarrow}^{\frac{4}{3}} + C_{xc}^{\uparrow\downarrow}(n,\xi)\nabla n\uparrow.\nabla n\downarrow/(n\uparrow n\downarrow)^{\frac{2}{3}}] \quad \ldots.5)$$

valid for slowly varying spin densities. By symmetry, $C_{xc}^{\downarrow\downarrow}(n,\xi) = C_{xc}^{\uparrow\uparrow}(n,-\xi)$ and $C_{xc}^{\uparrow\downarrow}(n,\xi) = C_{xc}^{\uparrow\downarrow}(n,-\xi)$ The exchange coefficients are constants: $C_x^{\downarrow\downarrow} = C_x^{\uparrow\uparrow}$ and $C_{xc}^{\uparrow\downarrow} = 0$.

In the high-density limit, the correlation coefficients $C_c^{\sigma\sigma'}$ depend exclusively upon the local spin polarization, ξ, not upon n. A parameterization capturing this relationship established by Rasolt and Davis [32]. For $|\nabla\xi| = 0$, equation (1) simplifies to,

$$E_{xc} = \int d^3r \left[n\epsilon_{xc}(n,\xi) + \frac{C_{xc}(n,\xi)|\nabla n|^2}{n^{\frac{4}{3}}}\right] \quad \ldots.6)$$

Where,

$$C_{xc}(n,\xi) = C_{xc}^{\uparrow\uparrow}(n,\xi)\left[\frac{1+\xi}{2}\right]^{\frac{2}{3}} + C_{xc}^{\downarrow\downarrow}(n,\xi)\left[\frac{1-\xi}{2}\right]^{\frac{2}{3}} + C_{xc}^{\uparrow\downarrow}(n,\xi)\left[\frac{1+\xi}{2}\right]^{\frac{1}{3}}\left[\frac{1-\xi}{2}\right]^{\frac{1}{3}} \quad \ldots.7)$$

Hence, the precise scaling of the exchange coefficient can be expressed as follows:

$$C_x(\xi)/\,C_x(0) = g(\xi) \quad \ldots.8)$$

Here we use Sham's exchange coefficient [33]. For correlation, we use the Rasolt-Davis parameterization of the high-density limit to find,

$$C_c(n,\xi)/\,C_c(n,0) = g(\xi) \quad \text{.....9)}$$

With an error less than 1%. Above equation is exact at |ξ|=0 and 1 and the error us less than 0.5% for $|\xi| \leq 0.6$.

While generalized gradient approximation functionals have significantly improved upon the accuracy of local density approximation in density functional theory, they still have certain limitations and drawbacks. Some of the drawbacks of GGA functionals includes that they tend to underestimate the band gaps of semiconductors and insulators, often struggle to accurately describe long-range dispersion forces (van der Waals interactions) and gives poor results for strongly correlated system. Researchers and computational chemists are aware of these drawbacks and have been working on developing improved XC functionals that address these issues. Hybrid functionals, meta-GGA functionals, and other advanced approaches aim to overcome these limitations and provide more accurate and reliable descriptions of various systems.

2.3. meta-Generalized gradient approximation (*meta*-GGA)

Meta-GGAs combine an additional element: the orbital kinetic energy density, which can be connected to fulfill additional exact constraints. For example, it agrees us to extend the gradient expansion of the exchange energy beyond the second order (as seen in PBEsol) and even up to the fourth order in gradient terms. Simultaneously, this approach holds a precise linear response of the uniform density, thus, avoiding the necessity for GGA constraint selection. Meta-GGAs further possess the ability to nullify the correlation energy for a one-electron density, which is beneficial considering that a one-electron system inherently lacks correlation effects. Additionally, the capability to exactly compute the exchange energy arises, although for specific densities, like that of a one-electron atom. Through the combination of this supplementary element—the orbital kinetic energy density, meta-GGA approaches can identify spatial regions where a single orbital's form mostly influences the electron density.

The meta-GGA [34] method employs the kinetic energy densities $\tau_{\uparrow}(r)$ and $\tau_{\downarrow}(r)$, as well as the Laplacians of the densities $n_{\uparrow}(r)$ and $n_{\downarrow}(r)$, as supplementary components [23]. In this context, the kinetic energy density for electrons with spin σ is characterized through the occupied Kohn-Sham orbitals $\psi_{i\sigma}(r)$ and it is defined as follows:

$$\tau_\sigma(\vec{r}) = \sum_i^{occupied} \frac{1}{2} |\nabla\psi_{i\sigma}(r)|^2 \quad \text{.....10)}$$

The kinetic energy density exhibits two fundamental properties:

(1) Within regions governed by a single electron $\tau_\sigma(r) = \tau_\sigma^W(r)$ for real orbitals, where in the von Weizsacker kinetic energy density [35] is implicated.

$$\tau_\sigma^W(r) = {|\nabla n_\sigma|^2}/{8n_\sigma} \quad \text{.....11)}$$

(2) When dealing with a gradually changing spin-unpolarized density, it conforms to a second-order gradient expansion.

$$\tau^{GEA} = \tau^{unif} + \frac{1}{72}\frac{|\nabla n|^2}{n} + \frac{1}{6}\nabla^2 n + 0(\nabla^4) \quad \text{.....12)}$$

Where $\tau = \sum_\sigma \tau_\sigma$ and $\tau^{unif} = \frac{3}{10}(3\pi^2)^{\frac{2}{3}} n^{\frac{5}{3}}$ is the Thomas-Fermi kinetic energy density.

Kinetic energy density is a measure of the local kinetic energy associated with the electron motion within a certain region of space. Including the kinetic energy density in the XC functional can help to improve the description of systems with rapidly varying electron densities, such as molecules with strong chemical bonds and regions of charge density concentration. The addition of the kinetic energy density introduces additional terms and dependencies in the functional, making the resulting expressions more complex compared to standard GGA functionals. In the form of,

$$E_{XC}[n\uparrow, n\downarrow] = \int d^3r\, n\, \epsilon_{xc}(n\uparrow, n\downarrow, \nabla n\uparrow, \nabla n\downarrow, \tau\uparrow, \tau\downarrow) \quad \text{.....13)}$$

where $n(r) = n_{\uparrow}(r) + n_{\downarrow}(r)$ is the total density and $\varepsilon_{xc}(r)$ the exchange-correlation energy per electron.

Utilizing the features of the kinetic energy density τσ(r), Tao, Perdew, Staroverov and Scuseria (TPSS) recently developed a meta-GGA [36]. Among the available meta-GGAs, our preference lies with TPSS. In comparison to GGAs, TPSS offers accurate lattice constants for solids, as well as precise surface energies and binding energies for atoms. Furthermore, it successfully calculates binding energies of molecules to surfaces, making it highly suitable for

various materials science computations. In the TPSS meta-GGA, the exchange energy for a spin-polarized system can be computed by employing the exchange functional intended for a spin-unpolarized system, utilizing the spin-scaling relation [37].

$$E_X[n\uparrow, n\downarrow] = {E_X[2n\uparrow]}/{2} + {E_X[2n\downarrow]}/{2} \quad \text{.....14)}$$

Consequently, our task is to approximate the exchange energy $E_x(n)$ for a spin-unpolarized system. Furthermore, our functional must fulfill the condition of uniform coordinate scaling [38].

$$E_X[n_\gamma] = \gamma E_X[n] \quad \text{.....15)}$$

Where $n_\gamma(r) = \gamma^3 n(\gamma r)$ is the scaled density of n(r). Thus, we write the meta-GGA as,

$$E_X^{MGGA}[n] = \int d^3r\, n\, \varepsilon_{xc}{}^{unif}(n)\, F_X(p,z) \quad \text{.....16)}$$

Here, the enhancement factor, which reveals the extent of nonlocality, is defined as:

$$F_{XC} = {\varepsilon_{xc}}/{\varepsilon_x{}^{unif}(n)} \quad \text{.....17)}$$

Where $\varepsilon_x{}^{unif}(n) = -\left(\frac{3}{4\pi}\right)(3\pi^2 n)^{\frac{1}{3}}$,

It refers to the exchange energy per particle in a spin-unpolarized uniform electron gas The meta-GGA functional must also adhere to the Lieb-Oxford bound [39,40],

$$E_X[n\uparrow, n\downarrow] \geq E_{XC}[n\uparrow, n\downarrow] \geq -1.679 \int d^3r\, n^{\frac{4}{3}} \quad \text{.....18)}$$

The TPSS meta-GGA correlation functional originates from the removal of self-correlation energy from the PBE GGA [41], similar to the approach employed by the PKZB (Perdew-Kurth-Zupan-Blaha) meta-GGA [42]. This is accomplished without compromising the accuracy of the second-order gradient expansion within the slowly varying regime. The PKZB meta-GGA, however, exhibits an incorrect dependency on relative spin polarization in the low-density limit, which TPSS rectifies to the extent possible for a meta-GGA. The chosen form of the TPSS meta-GGA correlation functional retains these accurate attributes of the PKZB functional, and it can be expressed as follows:

$$E_C^{MGGA}[n\uparrow, n\downarrow] = \int d^3r\, n\, \epsilon_{xc}{}^{revPKZB} \times [1 + d\epsilon_C^{revPKZB}(\tau^W/\tau)^3] \quad \text{.....19)}$$

Where, $E_C^{MGGA} = 0$ for fully spin-polarized one-electron densities. So, we can write the TPSS correlation energy per electron,

$$\epsilon_C^{MGGA} = \epsilon_c{}^{revPKZB}[1 + d\epsilon_C^{revPKZB}(\tau^W/\tau)^3 \quad \text{.....20)}$$

Notably, we aim to tackle a constraint that has not been previously addressed—a stringent Lieb–Oxford lower bound on the exchange energy pertaining to any one-electron density. The exchange energy associated with any one-electron density is stringently bounded by the Lieb–Oxford lower bound. This implies that the functional's behavior is largely dictated by this lower bound when considering one-electron densities, and we aim to capitalize on this aspect.

The TPSS meta-GGA incorporates a significant portion of the available exact constraints on the exchange-correlation energy as a density functional However, a few crucial constraints still remain, which are essential for the advancement of additional nonempirical functionals within the hierarchy of approximations known as Jacob's ladder [14]. Achieving these constraints is possible on the fifth rung of the ladder.

The meta-GGA functional aims to capture more complex features of the electron density and its gradients, leading to improved accuracy in predicting various properties of molecular and solid-state systems. Like any theoretical approach, meta-GGA functionals have their successes and drawbacks that are they can often describe non-covalent interactions (such as van der Waals forces) more accurately than GGA functionals, they can provide improved descriptions of systems with strong electron correlation, such as transition metal complexes or systems with localized electrons and this is especially important for studies involving chemical reactions and molecular dynamics. Some drawbacks are; meta-GGA functionals are often more computationally expensive than simpler functionals like GGA or LDA, while meta-GGA functionals incorporate more information about the electron density, they may still miss certain higher-order effects that are important in some systems. In recent years, efforts have been directed towards developing new meta-GGA functionals that address these limitations and further improve accuracy.

2.4. Hybrid density functionals

Hybrid functionals [43,44] represent a significant improvement over standard local density approximation and generalized gradient approximation functionals,

as well as meta-GGA functionals, by incorporating a fraction of exact Hartree-Fock exchange [45]. The basic idea behind hybrid functionals is to combine the advantages of both density functional theory and Hartree-Fock methods. In DFT, the exchange-correlation energy is approximated based on the electron density, making it computationally efficient and applicable to a wide range of systems. This accurately describes the key points about hybrid functionals and their relationship to DFT and Hartree-Fock methods.

However, traditional DFT methods can sometimes lead to inaccuracies in predicting properties such as band gaps and reaction energies. on the other hand, Hartree-Fock theory, includes exact exchange terms that treat electron-electron interactions more rigorously. This can lead to better descriptions of electronic correlations and energy gaps but is computationally demanding, especially for larger systems. It highlights the shortcomings of traditional DFT methods and the benefits of Hartree-Fock theory while also acknowledging the computational challenges

Hybrid functionals strike a balance between these two approaches by incorporating a fraction of Hartree-Fock exchange into the DFT calculation. The functional takes the form:

$$E_{XC}^{Hybrid} = aE_X^{HF} + (1-a)E_X^{DFT} + E_C^{DFT} \quad \text{.....21)}$$

Where, E_{XC}^{Hybrid} is the total exchange-correlation energy of the hybrid functional, E_X^{HF} is the Hartree-Fock exchange energy, E_X^{DFT} is the exchange energy from the standard DFT functional, E_C^{DFT} is the correlation energy from the standard DFT functional and a is the mixing parameter, often called the Hartree-Fock exchange mixing coefficient.

The value of the mixing parameter a determines the fraction of Hartree-Fock exchange included in the functional. Different hybrid functionals use different values of a to balance accuracy and computational cost. Popular hybrid functionals include B3LYP (a = 0.20), PBE0 (a = 0.25) and HSE06 (a ≈ 0.25) among others.

One of the simplest examples of these hybrid functionals is PBE0 [46,47], which combines a fraction of exact exchange with a complementary fraction of exchange from the PBE-GGA functional and full PBE correlation. A common choice for the fraction of exact exchange is around 25%. This percentage can be considered a semi-empirical parameter because the rationale behind its value is not precisely established. Nevertheless, this functional has demonstrated superior accuracy compared to the PBE functional for predicting atomization energies of molecules and lattice constants of solids. It also improves the calculation of surface energies and energy barriers, compared to PBE. It gives improved but still inaccurate dissociation limits, but this is at least an improvement on semi-local functionals.

We note, however, that it has been argued that the ratio of the required nonlocal exchange is system dependent [44]. The electron correlation is represented by the correlation part of the PBE density functional. The resulting expression for the exchange correlation energy then takes the following simple form:

$$E_{xc}^{PBE0} = \frac{1}{4}E_x + \frac{3}{4}E_x^{PBE} + E_c^{PBE} \quad \text{.....22)}$$

where the nonlocal Fock exchange energy E_x in real space can be written as,

$$E_x = -\frac{e^2}{2}\sum_{kn,qm} 2w_k f_{kn} \times 2w_q f_{qn} \times \iint d^3r\, d^3r' \frac{\phi_{kn}^*(r)\phi_{qm}(r)\phi_{qm}^*(r')\phi_{kn}(r')}{|r-r'|}$$

.....23)

In terms of the set of one-electron Bloch states $\{\phi_{kn}(r)\}$ of the system and the corresponding set of occupational numbers $\{f_{kn}\}$. The sums over k and q need to be performed over all k-points chosen to sample the Brillouin zone BZ, whereas the sums over m and n are performed over all bands at these k-points. The k-point weights W_k typically sum to one, and the factors of 2 account for the consideration of a closed-shell system with doubly occupied one-electron states. The corresponding non-local Fock exchange potential is given by,

$$V_x(r,r') = -e^2 \sum_{qm} 2\, w_q f_{qm} e^{-iq.r'} \frac{u_{qm}^*(r')u_{qm}(r)}{|r-r'|} e^{iq.r}$$

.....24)

Where $u_{qm}(r)$ is the cell periodic part of the Bloch state. This equation can be written in the form of,

$$V_x(r,r') = \sum_k \sum_{GG'} e^{i(K+G).r} V_k(G,G')\, e^{-i(k+G').r'}$$

.....25)

where,

$$V_k(G,G') = \langle k+G|V_x|k+G'\rangle = -\frac{4\pi e^2}{\Omega}\sum_{mq} 2w_q f_{qn} \times \frac{\sum_{G''} C_{qm}^*(G'-G'')C_{qm}(G-G'')}{|k+q+G''|^2}$$

.....26)

is the representation of the Fock exchange potential in reciprocal space is a key aspect [48]. The description of finite systems using the PBE0 functional has been

extensively investigated. The notable improvement compared to PBE calculations is attributed to utilizing a fixed portion of the Fock exchange, which moderates the self-interaction error inherent in density functional theory. To avoid the computation of costly integrals involving the slowly decaying long-ranged component of the Fock exchange, Heyd [49] proposed its replacement with the corresponding density functional counterpart. The resulting expression for the exchange-correlation energy HSE03 is given by,

$$E_{xc}^{HSE03} = \frac{1}{4}E_x^{sr,\mu} + \frac{3}{4}E_x^{PBE,sr,\mu} + E_x^{PBE,lr,\mu} + E_c^{PBE} \quad .....27)$$

As can be observed from the equation above, the electron-electron interaction is separated into distinct short-range and long-range components, with only the exchange part being involved in this separation. A simple decomposition of the Coulomb kernel [50] can be obtained using the construction,

$$\frac{1}{r} = S_\mu(r) + L_\mu(r) = \frac{erfc(\mu r)}{r} + \frac{\mathrm{erf}(\mu r)}{r} \quad .....28)$$

Where $r = |r - r'|$ and μ is the parameter that establishes the range separation corresponding to the characteristic distance at which the influence of short-range interactions becomes insignificant. In the framework of the HSE03 functional, empirical studies have indicated that the μ, is approximately 0.3 $Å^{-1}$ [49]. Using the decomposed coulomb kernel, one obtains straightforwardly,

$$E_x^{sr,\mu} = -\frac{e^2}{2}\sum_{kn,qm} 2w_k f_{kn} \times 2w_q f_{qn} \times \iint d^3r\, d^3r' \frac{erfc(\mu|r-r'|)}{|r-r'|} \times \phi_{kn}^*(r)\phi_{qm}(r)\phi_{qm}^*(r')\phi_{kn}(r') \quad .....29)$$

The representation of the corresponding short-range Fock exchange potential in reciprocal space is given by,

$$V_k^{sr,\mu}(G,G') = \langle k+G|V_x^{sr,\mu}|k+G'\rangle = -\frac{4\pi e^2}{\Omega}\sum_{mq} 2w_q f_{qm} \times \frac{\sum_{G''} C_{qm}^*(G'-G'')C_{qm}(G-G'')}{|k-q+G''|^2} \times \left(1 - e^{-\frac{|k-q+G''|^2}{4\mu^2}}\right) \quad .....30)$$

The only distinction in the reciprocal space representation of the complete Fock exchange potential, as provided by equation (5), lies in the second factor found in equation (9), which denotes the complementary error function in reciprocal space. Notably, equation (9) illustrates that the range-separated exchange interaction falls within the category of screened exchange interactions.

The short-range PBE exchange energy and potential, along with their corresponding long-range components, are determined using the same decomposition scheme, as proposed by Heyd. It's evident from equation (7) that the long-range term becomes zero when μ=0, resulting in the short-range contribution equating the full Coulomb operator. Conversely, as μ approaches ∞, this relationship is inverted. Consequently, the two extreme cases of the HSE03 functional, as depicted in equation (6), correspond to the PBE0 functional for μ=0 and a pure PBE calculation for μ→ ∞.

Furthermore, the hybrid functional allows for an improved prediction of energy gaps in materials. This improvement is due to the potential within the hybrid functional, which is a blend of a non-local Hartree-Fock potential and a local Kohn-Sham potential, in contrast to the strictly local Kohn-Sham potential. The non-local character of the potential can emulate the behavior of the self-energy, leading to a more accurate description of bandgaps that may not be adequately captured solely from the orbital energies of the exact Kohn-Sham density functional.

This hybridization aims to improve the accuracy of DFT calculations, especially for systems where standard functionals might fail. Here are the key success and drawbacks of hybrid functionals: The inclusion of exact exchange allows hybrid functionals to better capture both short-range and long-range electronic interactions, leading to improved description of van der Waals forces and intermolecular interactions, Hybrid functionals can provide significantly improved accuracy compared to standard DFT functionals for certain electronic properties such as band gaps, reaction energies, and ionization potentials. This is particularly important for systems with significant electron correlation effects, where standard DFT functionals may underestimate or overestimate these properties. Some drawbacks are: The development of hybrid functionals often involves empirical tuning, and there might not always be a clear theoretical basis for the specific mixing of exchange terms used in a particular functional, the success of hybrid functionals can be system-dependent. They might perform well for some systems but not for others, and there is no universally best functional for all types of calculations.

2.5. Double-hybrid density functionals

Double-hybrid density functionals (DHDFs) constitute the fifth and most advanced rung of Jacob's Ladder, extracting insights from unoccupied Kohn–Sham orbitals. In Double-hybrid density functionals (DHDFs), portions of the standard exchange and correlation functionals in density functional theory are replaced with contributions from nonlocal Fock-exchange and second-order perturbative correlation. The fifth-rung functionals are the RPA-like functionals. The concept of RPA (Random Phase Approximation) [51] in the context of density functional theory emerged in the 1970s. This many-body approximation encompasses unoccupied Kohn–Sham orbitals, a distinction from the preceding four levels which solely utilize occupied orbitals. While RPA offers near-exact results for the long-range fraction of the exchange-correlation hole, its accuracy diminishes in the short-range portion. This latter aspect relies on the well-established MP2 wave-function approach, albeit leveraging Kohn–Sham orbitals for its computation.

However, in recent years, Georg Kresse has applied RPA [52] to solids and observed a substantially improved error cancellation. This outcome closely resembles the error cancellation we had anticipated in the 1990s. Kresse and his contemporaries have demonstrated that RPA can deliver highly precise lattice constants, surface energies, cohesive energies, and solid-state reaction energies. The discovery that the RPA can furnish accurate structures and reliable transition pressures for structural phase transitions in solids have been done. Additionally, RPA effectively captures the long-range van der Waals interaction, an aspect absents from the initial four levels of the ladder

Therefore, the expectation is that DHDFs are more accurate and robust than lower-rung DFAs [53]. Here, we are referring to the DHDFs as originally defined by Grimme for the B2PLYP7 [54] DFA in 2006, which is the First modern double-hybrid with a PT2 contribution replacing parts of the DFT correlation. In the B2PLYP method, a portion of the (semi-)local DFT exchange and correlation is substituted with non-local Fock exchange, along with a non-local correlation contribution derived from Møller-Plesset (MP) type second-order perturbation theory (PT2). In this exchange-correlation functional, B88 functional is used as exchange DFT functional and LYP functional is used as correlation DFT functional. The DHDF exchange-correlation energy is calculated as follows,

$$E_{xc}^{DH}[\rho] = a_x E_x^{HF} + (1 - a_x)E_x^{DFA}[\rho] + (1 - a_c)E_c^{DFA}[\rho] + a_c E_c^{PT2} \quad .....31)$$

where E_{XC}^{HF} represents the Fock-exchange contribution, also known from Hartree-Fock (HF) theory, E_X^{DFA}, the DFA exchange part, E_C^{DFA} the DFA correlation component, and E_C^{PT2} the second order correlation perturbation term based on KS orbitals. The second DH-functional is mPW2-PLYP, which is Similar to B2-PLYP, but with different DFT exchange. It is also developed in 2006. In this exchange-correlation functional, mPW functional is used as exchange DFT functional and LYP functional is used as correlation DFT functional.

DHDFs not only represent a conceptual advancement on Jacob's Ladder but have also been extensively validated through numerous benchmark and application studies. Various iterations of this approach have consistently demonstrated significantly improved accuracy when compared to hybrid functionals.

The failure of standard functionals in delivering a satisfactory depiction of Vander Waals complexes is remedied by incorporating orbital-dependent correlation terms. This not only addresses this challenge but also enhances the treatment of numerous short-range correlation effects within molecules. However, the limitation of perturbative computation as in all double hybrids is obvious in electronically complicated situations when this approach can fail.

Indeed, the computation by RPA methods may be the best way to go for the future and these methods leading to the eventual replacement of double-hybrid functionals by these techniques as the go-to "everyday" electronic structure methods. As evidenced by the theory's success in describing excited states, exploring its applications in calculating molecular properties beyond ground-state energy and structure holds the potential to yield enhanced outcomes compared to those obtained from standard functionals.

2.6. Comparison of Different systems and its properties with Exchange-Correlation functionals

System	Properties	Functionals										Exp. value
		LDA	PBE	PBEsol	PW91	BLYP	TPSS	SCAN	B3LYP	PBE0	HSE06	
C_{18} [55]	Bond length (Å)	-	1.284	-	-	1.2851	-	-	1.2769	**1.2758**	-	1.275
	Bond angle (°)	-	**160.01**	-	-	160.04	-	-	160.03	160.03	-	160
H_2 Molecule	Harmonic Frequency (cm^{-1}) [16]	-	4319	-	-	4349	**4419**	-	4421	-	-	4401
	Atomization energy (Kcal/mol) [42]	**113.3**	138.6	-	-	-	114.5	-	-	-	-	109.5
Si	Bulk Modulus (GPa) [56]	97	89	94	88	-	92	99.30	-	100	**99**	99
	Lattice constant Å) [56]	5.403	5.470	5.436	-	-	5.456	-	5.4357	**5.435**	5.438	5.430
	Band gap (eV) [22]	0.59	0.75	-	-	-	0.79	0.93	2.26	1.81	**1.16**	1.17
	Elastic Constant (GPa) [56]	161	153	156	-	-	157	-	-	171	**170**	167
Ge	Bulk Modulus (GPa) [56]	73	60	68	76	-	66	73.38	-	**75**	73	75
	Lattice constant (Å) [56]	5.627	5.550	**5.674**	5.547	-	5.705	-	-	5.676	5.682	5.658
	Band gap (eV) [22]	0.0	0.0	-	-	-	0.26	**0.56**	-	1.39	**0.56**	0.74
	Elastic Constant (GPa) [56]	123	105	116	-	-	115	-	-	133	**131**	129
GaAs	Lattice constant (Å) [56]	**5.610**	5.751	5.661	-	-	5.714	-	-	5.674	5.680	5.637
	Atomization energy [57] (KJ/mol/atom)	-	**304**	343	-	-	-	-	-	-	304	319
	Bulk Modulus (GPa) [56]	**74**	60	69	-	-	64	-	-	73	71	75
	Elastic Constant (GPa) [56]	116	98	109	-	-	103	-	-	**118**	117	120
	Band gap (eV)[55]	0.43	0.18	0.45	-	-	-	-	-	-	**1.29**	1.52
InP [56]	Lattice constant (Å)	5.827	5.957	**5.879w**	-	-	5.948	-	-	5.893	5.889	5.855
Graphene [56]	Lattice constant (Å)	2.446	2.467	**2.460**	2.466	-	-	-	-	-	-	2.46
	Thermal conductivity ($Wm^{-1}K^{-1}$)	1999.1	1936.1	3094.97	**3196.81**	-	-	-	-		-	4000 [59]
Cu [60]	Cohesive energy (eV/atom)	4.548	**3.48**	4.046	3.517	-	3.73	-	2.54 [61]	3.01	3.06	3.48
	Lattice parameter (Å)	3.532	3.649	**3.579**	3.646	-	-	3.61 [62]	-	-	-	3.595
	Bulk Modulus (GPa)	177.7	146.9	160.4	134.6	-	184.3	146 [62]	113.4 [61]	135.2	**133.8**	133.0

MoS_2 [63]	Activation Energy (eV)	0.27	-	-	**0.31**	0.28	-	-	-	-	-	0.32
LiF	Atomization energy (KJ/mol/atom) [57]	-	**418**	432	-	-	-	-	-	-	408	425
	Band gap (eV) [57]	8.93 [64]	8.85	9.05	-	-	-	-	**11.68**	-	-	13.6
	Formation energy (KJ/mol) [57]	-	569	573	-	-	-	-	-	-	**591**	614
	Lattice Constant (Å) [56]	3.906	4.074	4.022	-	-	4.049	-	4.027	**4.021**	4.023	4.010
	Bulk Modulus (GPa) [56]	90	71	76	-	-	71	-	-	78	**77**	77
	Elastic Constant (GPa) [56]	166	117	**134**	-	-	121	-	-	132	131	136
α-Ag_3VO_4 [65]	Lattice Constant (Å)	9.827	**10.665**	-	10.788	-	-	-	-	-	-	10.267
TiN [66]	Lattice Constant (Å)	4.175	**4.237**	-	4.236	-	-	-	-	-	-	4.238
	Elastic Constant (GPa)	735	598	-	**610**	-	-	-	-	-	-	625
	Bulk Modulus (GPa)	**307**	278	-	270	-	-	-	-	-	-	318
Pd [67]	Lattice Constant (Å)	-	3.94	-	-	4.04	-	-	3.99	-	**3.93**	3.89
Pt [67]	Lattice Constant (Å)	-	3.97	-	-	4.06	-	-	4.02	-	**3.93**	3.92
TiO_2 [68]	Lattice Constant (Å)	4.555	4.653	-	-	-	-	-	4.639	4.591	**4.588**	4.587
InSb [56]	Elastic Constant (GPa)	**67**	54	61	-	-	56	-	-	68	**67**	67
	Lattice Constant (Å)	**6.450**	6.631	6.518	-	-	6.600		-	6.534	6.542	6.473
	Bulk Modulus (GPa)	**47**	37	43	-	-	38		-	46	45	47
CaF_2 [56]	Elastic Constant (GPa)	191	159	171	-	-	**160**	-	-	171	170	164

In this table, we compared the calculated values of various properties using different density functional theory functionals with experimental reference values. The properties being compared include bond lengths and bond angles, harmonic frequencies, atomization energies, bulk modulus, lattice constants, elastic constants, band gaps, cohesive energies, activation energies, formation energies and vertical energies. The DFT functionals being compared are: LDA, PBE, PBEsol (PBE for solids), PW91, BLYP, TPSS, SCAN, B3LYP, PBE0 and HSE06. This comparison likely aims to evaluate the performance of these DFT functionals in predicting the mentioned properties by analysing how well they match experimental data, taking into account both uncorrected and corrected experimental values, as well as the deviations between calculations and experiments. This type of analysis helps us to choose the most appropriate functional for specific research purposes. The items mentioned are listed in the same order as presented in the table. Within the table, the numbers highlighted in boldface indicate the values that closely match the corresponding experimental values. These boldface values suggest that the associated functionals exhibit the best performance for the specific systems detailed in the table.

Upon examining the table, it becomes evident that the LDA functional consistently underestimates the equilibrium lattice constants for most of the systems, while overestimating them for GaAs and InSb. This indicates that, among the functionals investigated, the

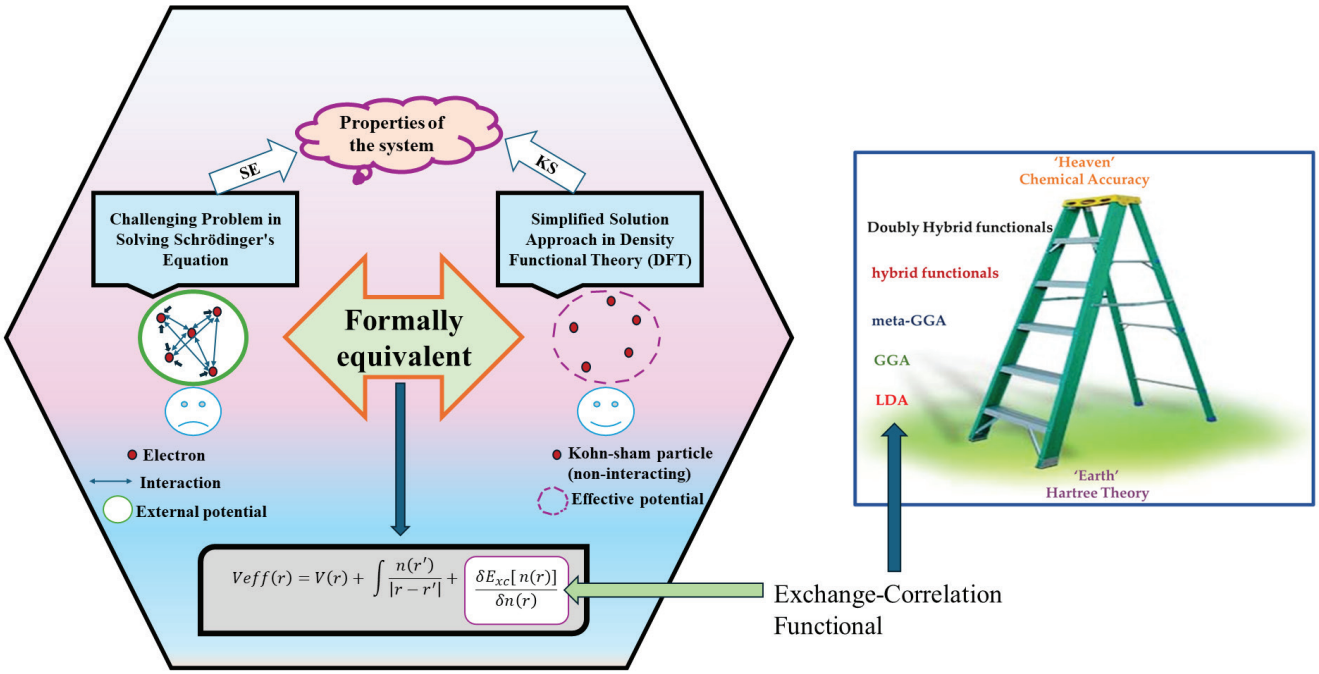

Fig. TOC

LDA functional is the least accurate in its predictions.

Regarding the bulk modulus, the LDA functional performs well for GaAs, TiN, and InSb, whereas the hybrid functionals (PBE0 and HSE06) excel for a wide array of systems. Additionally, the HSE06 hybrid functional proves to be the most proficient and accurate in predicting the bandgap values for the various systems considered.

Furthermore, GGA functionals demonstrate proficiency in predicting cohesive and atomization energies. The table also reveals that meta-GGA functionals (TPSS and SCAN) yield favorable outcomes for harmonic frequencies, band gaps and elastic constants concerning H_2 molecule, Ge, and CaF_2, respectively. In summary, our analysis of the table leads us to the conclusion that hybrid functionals exhibit the highest accuracy across the majority of the systems presented.

3. Conclusion and future prospects

Kohn-sham density theory has a demanding foundation for ground-state energies, ground-state electron densities, and geometric structures. It also has an order of approximations - the "Jacob's ladder" - of increasing sophistication for the exchange-correlation energy as a functional of the density. A large number of exchange-correlation functionals have been tested for solid-state properties, namely, the bond length, bond angle, harmonic frequency, atomization energy, bulk modulus, lattice constant, bandgap energy, elastic constant, dielectric constant, cohesive energy, activation energy, formation energy, vertical energy gap. One of the purposes of this work was to assess the accuracy of different XC functionals and mostly the recently proposed functionals like the m-GGA TPSS, SCAN and hybrid HSE. And from the assessment to identify the functionals which are used extensively and show great accuracy for any general kind of material or the property. As shown in the paper we can say that the functionals SCAN and BLYP are not used often. For most of the elastic constant and lattice constant calculations the hybrid functionals (PBE0, HSE06) functional show the most accurate results. For the commonly known semiconductors the hybrid functionals give the best results. For the III-V group semiconductors such as GaAs, InSb and InP the LDA and GGA functionals show great results. For 'transition metal dichalcogenides' the PW91 functionals show better performance. Finally, based on the current and earlier published works, a short conclusion can be drawn. Currently, the functionals yield favorable results under specific conditions.

Here are some potential future perspectives and developments in the field of exchange-correlation

functionals and Jacob's Ladder: Researchers are likely to continue developing more accurate exchange-correlation functionals that can better describe complex electronic interactions in various materials. This might involve incorporating more sophisticated physical models and taking into account dispersion forces, Vander Waals interactions, and more. Machine learning techniques have shown promise in improving exchange-correlation functionals. Future developments might involve using large datasets and machine learning algorithms to develop functionals that can capture complex electronic behaviors across different systems. Many systems, especially heavy elements and molecules involving high-energy processes, require the inclusion of relativistic effects. Future functionals might aim to accurately incorporate relativistic corrections into the exchange-correlation functionals. Current functionals struggle with strongly correlated systems, where electron-electron interactions play a significant role. Future work might involve developing functionals that can handle these situations more accurately. Collaboration within the scientific community is key to developing better functionals. Open-source projects and shared databases of functionals and benchmark results could help accelerate progress in this field. We hope that this article will encourage not only new applications but also further work toward the goal.

Conflict of interest:

On behalf of all authors, the corresponding author states that there is no conflict of interest.

Acknowledgments:

The authors are thankful to the department of physics, faculty of science, The Maharaja Sayajirao University of Baroda, Vadodara for the computational facilities.

References

1. R. M. Dreizler, *Sdensity Functional Theory of Relativistic Systems*, Phys. Scr. **1993**, 167 (1993).
2. P. Jaksch, I. Yakimenko, and K. Berggren, *And Correlation Effects*, 1 (2006).
3. M. Noe, R. Heller, W. H. Fietz, W. Goldacker, and T. Schneider, *HTS Applications*, Proc. - Work. Accel. Magn. Supercond. Des. Optim. WAMSDO 2008 94 (2009).
4. W. Kohn, *Nobel Lecture: Electronic Structure of Matter - Wave Functions and Density Functional*, Rev. Mod. Phys. **71**, 1253 (1999).
5. C. H. Chu and C. W. Leung, *The Convolution Equation of Choquet and Deny on [IN]-Groups*, Integr. Equations Oper. Theory **40**, 391 (2001).
6. M. Y. Zhang, Z. H. Cui, Y. C. Wang, and H. Jiang, *Hybrid Functionals with System-Dependent Parameters: Conceptual Foundations and Methodological Developments*, Wiley Interdiscip. Rev. Comput. Mol. Sci. **10**, 1 (2020).
7. L. J. Sham and W. Kohn, *One-Particle Properties of an Inhomogeneous Interacting Electron Gas*, Phys. Rev. **145**, 561 (1966).
8. J. P. Perdew, *Jacob's Ladder of Density Functional Approximations for the Exchange-Correlation Energy*, **1**, 1 (2003).
9. J. D. Talman and W. F. Shadwick, *A, =1.*, **14**, (1976).
10. S. Report, *An Exchange-Correlation Functional Capturing Bulk , Surface , and Confinement Physics Sandia National Laboratories*, (2018).
11. S. F. Sousa, P. A. Fernandes, and M. J. Ramos, *General Performance of Density Functionals*, J. Phys. Chem. A **111**, 10439 (2007).
12. T. J. Giese and D. M. York, *Density-Functional Expansion Methods: Evaluation of LDA, GGA, and Meta-GGA Functionals and Different Integral Approximations*, J. Chem. Phys. **133**, (2010).
13. F. Tran, J. Stelzl, and P. Blaha, *Rungs 1 to 4 of DFT Jacob's Ladder: Extensive Test on the Lattice Constant, Bulk Modulus, and Cohesive Energy of Solids*, J. Chem. Phys. **144**, (2016).
14. A. H. Romero and M. J. Verstraete, *From One to Three, Exploring the Rungs of Jacob's Ladder in Magnetic Alloys*, Eur. Phys. J. B **91**, (2018).
15. V. Sahni, K. P. Bohnen, and M. K. Harbola, *Analysis of the Local-Density Approximation of Density-Functional Theory*, Phys. Rev. A **37**, 1895 (1988).
16. Y. Zhao and D. G. Truhlar, *A New Local Density Functional for Main-Group Thermochemistry, Transition Metal Bonding, Thermochemical Kinetics, and Noncovalent Interactions*, J. Chem. Phys. **125**, (2006).
17. M. Lewin, E. H. Lieb, and R. Seiringer, *The Local Density Approximation in Density Functional Theory*, Pure Appl. Anal. **2**, 35 (2020).
18. A. I. Mitsek, *CHARGE AND SPIN DENSITY WAVES IN 3d-METALS.*, Phys. Met. Metallogr. **61**, 27 (1986).
19. J. P. Perdew and K. Burke, *Generalized Gradient Approximation for the Exchange-Correlation Hole of a Many-Electron System*, Phys. Rev. B - Condens. Matter Mater. Phys. **54**, 16533 (1996).
20. J. P. Perdew, K. Burke, and M. Ernzerhof, *Generalized Gradient Approximation Made Simple*, Phys. Rev. Lett. **77**, 3865 (1996).
21. K. Burke, J. P. Perdew, and M. Ernzerhof, *Why the Generalized Gradient Approximation Works and How to Go beyond It*, Int. J. Quantum Chem. **61**, 287 (1997).
22. Y. Yao and Y. Kanai, *Plane-Wave Pseudopotential Implementation and Performance of SCAN Meta-GGA Exchange-Correlation Functional for Extended Systems*, J. Chem. Phys. **146**, (2017).
23. J. P. Perdew, J. Tao, V. N. Staroverov, and G. E. Scuseria, *Meta-Generalized Gradient Approximation: Explanation of a Realistic Nonempirical Density Functional*, J. Chem. Phys. **120**, 6898 (2004).

24. R. Peverati and D. G. Truhlar, *Improving the Accuracy of Hybrid Meta-GGA Density Functionals By*, J. Phys. Chem. Lett. **2**, 2810 (2011).
25. N. Mehta, M. Casanova-Páez, and L. Goerigk, *Semi-Empirical or Non-Empirical Double-Hybrid Density Functionals: Which Are More Robust?*, Phys. Chem. Chem. Phys. **20**, 23175 (2018).
26. W. Kohn and L. J. Sham, *R '[— P ',* **385**, (1965).
27. O. Gunnarsson and B. I. Lundqvist, *Erratum: Exchange and Correlation in Atoms, Molecules, and Solids by the Spin-Density-Functional Formalism (Physical Review B)*, Phys. Rev. B **15**, 6006 (1977).
28. J. P. Perdew, *Climbing the Ladder of Density Functional Approximations*, MRS Bull. **38**, 743 (2013).
29. A. Dal Corso, A. Pasquarello, A. Baldereschi, and R. Car, *Generalized-Gradient Approximations to Density-Functional Theory: A Comparative Study for Atoms and Solids*, Phys. Rev. B - Condens. Matter Mater. Phys. **53**, 1180 (1996).
30. K. Burke, J. P. Perdew, and Y. Wang, *Derivation of a Generalized Gradient Approximation: The PW91 Density Functional*, Electron. Density Funct. Theory 81 (1998).
31. Y. Wang and J. P. Perdew, *Spin Scaling of the Electron-Gas Correlation Energy in the High-Density Limit*, Phys. Rev. B **43**, 8911 (1991).
32. M. Rasolt and H. L. Davis, *Within the Local Potential Approximation ~*, Phys. Lett. **86**, 45 (1981).
33. J. Lampe, H. Rein, W. Scheler, and I. Introduction, *I 1972 1*, FEBS Lett. **23**, 0 (1972).
34. J. P. Perdew, *Accurate Density Functional for the Energy: Real-Space Cutoff of the Gradient Expansion for the Exchange Hole*, Phys. Rev. Lett. **55**, 1665 (1985).
35. E. Engel and R. M. Dreizler, *Extension of the Thomas-Fermi-Dirac-Weizsäcker Model: Four-Order Gradient Corrections to the Kinetic Energy*, J. Phys. B At. Mol. Opt. Phys. **22**, 1901 (1989).
36. J. Tao, J. P. Perdew, V. N. Staroverov, and G. E. Scuseria, *Climbing the Density Functional Ladder: Nonempirical Meta–Generalized Gradient Approximation Designed for Molecules and Solids*, Phys. Rev. Lett. **91**, 3 (2003).
37. G. L. Oliver and J. P. Perdew, *Spin-Density Gradient Expansion for the Kinetic Energy*, Phys. Rev. A **20**, 397 (1979).
38. M. Levy and J. P. Perdew, *Hellmann-Feynman, Virial, and Scaling Requisites for the Exact Universal Density Functionals. Shape of the Correlation Potential and Diamagnetic Susceptibility for Atoms*, Phys. Rev. A **32**, 2010 (1985).
39. Y. Zhao and D. G. Truhlar, *Construction of a Generalized Gradient Approximation by Restoring the Density-Gradient Expansion and Enforcing a Tight Lieb-Oxford Bound*, J. Chem. Phys. **128**, (2008).
40. E. H. Lieb and S. Oxford, *Improved Lower Bound on the Indirect Coulomb Energy*, Stab. Matter From Atoms to Stars Fourth Ed. **XIX**, 65 (2005).
41. J. P. Perdew, K. Burke, and M. Ernzerhof, *Perdew, Burke, and Ernzerhof Reply*, Phys. Rev. Lett. **80**, 891 (1998).
42. F. Avellaneda, C. Bustacara, J. P. Garzón, and E. González, *Implementation of a Molecular Simulator Based on a MultiAgent System*, Proc. - 2006 IEEE/WIC/ACM Int. Conf. Intell. Agent Technol. (IAT 2006 Main Conf. Proceedings), IAT'06 **82**, 117 (2006).
43. K. Raghavachari, *Perspective on "Density Functional Thermochemistry. III. The Role of Exact Exchange,"* Theor. Chem. Acc. **103**, 361 (2000).
44. J. P. Perdew, M. Ernzerhof, and K. Burke, *Rationale for Mixing Exact Exchange with Density Functional Approximations*, J. Chem. Phys. **105**, 9982 (1996).
45. M. a L. Marques and C. B. Lyon, *Functionals in DFT Hybrids Orbital Functionals What Functional to Use*, (2012).
46. C. Adamo and V. Barone, *Toward Reliable Density Functional Methods without Adjustable Parameters: The PBE0 Model*, J. Chem. Phys. **110**, 6158 (1999).
47. M. Ernzerhof and G. E. Scuseria, *Assessment of the Perdew-Burke-Ernzerhof Exchange-Correlation Functional*, J. Chem. Phys. **110**, 5029 (1999).
48. A. Baldereschi, *Q(G)e'q+o",* **34**, (1986).
49. J. Heyd, G. E. Scuseria, and M. Ernzerhof, *Hybrid Functionals Based on a Screened Coulomb Potential*, J. Chem. Phys. **118**, 8207 (2003).
50. T. Leininger, H. Stoll, H. J. Werner, and A. Savin, *Combining Long-Range Configuration Interaction with Short-Range Density Functional*, Chem. Phys. Lett. **275**, 151 (1997).
51. T. I. Shibuya and V. McKoy, *Higher Random-Phase Approximation as an Approximation to the Equations of Motion*, Phys. Rev. A **2**, 2208 (1970).
52. B. Ramberger, Z. Sukurma, T. Schäfer, and G. Kresse, *RPA Natural Orbitals and Their Application to Post-Hartree-Fock Electronic Structure Methods*, J. Chem. Phys. **151**, (2019).
53. L. Goerigk and S. Grimme, *Double-Hybrid Density Functionals*, Wiley Interdiscip. Rev. Comput. Mol. Sci. **4**, 576 (2014).
54. S. Grimme, *Semiempirical Hybrid Density Functional with Perturbative Second-Order Correlation*, J. Chem. Phys. **124**, (2006).
55. S. Arulmozhiraja and T. Ohno, *CCSD Calculations On*, **114301**, (2008).
56. M. Råsander and M. A. Moram, *On the Accuracy of Commonly Used Density Functional Approximations in Determining the Elastic Constants of Insulators and Semiconductors*, J. Chem. Phys. **143**, (2015).
57. L. Schimka, J. Harl, and G. Kresse, *Improved Hybrid Functional for Solids: The HSEsol Functional*, J. Chem. Phys. **134**, 1 (2011).
58. G. Qin, Z. Qin, H. Wang, and M. Hu, *On the Diversity in the Thermal Transport Properties of Graphene: A First-Principles-Benchmark Study Testing Different Exchange-Correlation Functionals*, Comput. Mater. Sci. **151**, 153 (2018).
59. A. A. Balandin, *Thermal Properties of Graphene and Nanostructured Carbon Materials*, Nat. Mater. **10**, 569 (2011).
60. M. Fishman, H. L. Zhuang, K. Mathew, W. Dirschka, and R. G. Hennig, *Accuracy of Exchange-Correlation Functionals and Effect of Solvation on the Surface Energy of Copper*, Phys. Rev. B - Condens. Matter Mater. Phys. **87**, 1 (2013).
61. P. Janthon, S. Luo, S. M. Kozlov, F. Viñes, J. Limtrakul, D. G. Truhlar, and F. Illas, *Bulk Properties of Transition Metals: A Challenge for the Design of Universal Density Functionals*, J. Chem. Theory Comput. **10**, 3832 (2014).
62. N. A. W. Holzwarth, M. Torrent, J. B. Charraud, and M. Côté, *Cubic Spline Solver for Generalized Density Functional*

Treatments of Atoms and Generation of Atomic Datasets for Use with Exchange-Correlation Functionals Including Meta-GGA, Phys. Rev. B **105**, 1 (2022).

63. O. El Beqqali, I. Zorkani, F. Rogemond, H. Chermette, R. Ben Chaabane, M. Gamoudi, and G. Guillaud, *Electrical Properties of Molybdenum Disulfide MoS2. Experimental Study and Density Functional Calculation Results*, Synth. Met. **90**, 165 (1997).
64. R. Webster, L. Bernasconi, and N. M. Harrison, *Optical Properties of Alkali Halide Crystals from All-Electron Hybrid TD-DFT Calculations*, J. Chem. Phys. **142**, 1 (2015).
65. C. Peng, Y. Liu, J. Cui, K. Luo, Y. Shen, and X. Li, *First-Principle Calculation of the Electronic Structure of α-Ag_3VO_4 Using Two Different Exchange Correlation Functionals*, Mater. Chem. Phys. **262**, 124307 (2021).
66. M. Marlo and V. Milman, *Density-Functional Study of Bulk and Surface Properties of Titanium Nitride Using Different Exchange-Correlation Functionals*, Phys. Rev. B - Condens. Matter Mater. Phys. **62**, 2899 (2000).
67. A. Stroppa and G. Kresse, *The Shortcomings of Semi-Local and Hybrid Functionals: What We Can Learn from Surface Science Studies*, New J. Phys. **10**, (2008).
68. F. Labat, P. Baranek, C. Domain, C. Minot, and C. Adamo, *Density Functional Theory Analysis of the Structural and Electronic Properties of TiO2 Rutile and Anatase Polytypes: Performances of Different Exchange-Correlation Functionals*, J. Chem. Phys. **126**, (2007).

Journal of the Maharaja Sayajirao University of Baroda: Science & Technology
Vol. 57, 2023, pp. 42-51

Synthesis, Characterization and Antibacterial Activities of Copper (ii) Complexes with New Binucleating Isoniazid Analogs

Ran Bahadur Yadav[1]*, N. D. Kulkarni[2], Arif Khan[3]

[1]Applied Chemistry Department, Faculty of Technology and Engineering, Kalabhavan,
The Maharaja Sayajirao University of Baroda, Vadodara-390001, India.

[2]Department of Chemistry, Faculty of Science,
The Maharaja Sayajirao University of Baroda, Vadodara-390002, India.

[3]Department of Microbiology and Biotechnology Centre, Faculty of Science,
The Maharaja Sayajirao University of Baroda, Vadodara-390002, India.

In the present study, two new binucleating ligands have been prepared from nicotinic and isonicotinic hydrazines. These have been used to prepare new ternary dicopper (II) complexes (1a-1b, 2a-2b) with general formula, $[Cu_2(AA)L(CH_3COO)_n]$. The ligands L are N-nicotinoyl-N'-[1-(5-acetyl-2,4-dihydroxy-phenyl)-ethylidene]-hydrazine or L = N-isonicotinoyl-N'-[1-(5-acetyl-2,4-dihydroxy-phenyl)-ethylidene]-hydrazine. The secondary ligands AA are 2,2'-bipyridine (a), or 1,10-phenanthroline (b). The ligands have been analyzed by elemental analysis and spectral techniques i.e. FTIR, ^{1}H NMR and ^{13}C NMR. The complexes have been characterized by elemental, thermal analysis and various spectroscopic methods. Room temperature magnetic properties shows ferromagnetic nature of the complexes. Antibacterial activity of the ligands and complexes has been examined against *S. aureus, B. megaterium* (gram positive) and *S. typhi, S. marsescens, P. vulgaris* (gram negative) strains. It has been observed that the ligand molecules are more active than corresponding complexes, the copper (II) ion in this case has in fact an inhibitory effect.

Keywords: Binucleating lignads, Binuclear copper (II) hydrazide complexes, Antibacterial activity.

1. Introduction

Hydrazides-hydrazones compounds have been demonstrated to possess, among other, antimicrobial, anticonvulsant, analgesic, antiinflammatory, antiplatelet, antitubercular and antitumoral activities [1-5]. Complexation of a drug molecule with a metal ion is always expected to alter its activity. It is specially so with copper (II) due to the redox properties associated with it. The antibiotic activity of the simplest drug molecule aspirin is known to be enhanced on coordination with copper (II). Another well known antibiotic ciprofloxacin has been shown to have enhanced activity when coordinated to copper (II) ion in a binary complex or a ternary complex with another polypyridine or amine ligand [6]. A variety of copper complexes including those with salicylaldoxime [7], 8-hydroxyquinoline [8], penicillamine [8], quinolone derivatives [9] and oxindole derivatives [10] are shown to possess anticancer activity. The anticancer / antitumer activity of known anticancer drugs like netropsin, daunamycin and combilexin have copper dependent activity [11]. The copper complex of isonicotinic acid hydrazide has been shown to possess antiviral activity [12].

Mixed ligand complexes of copper (II) complexes containing polypyridine ligand like 2,2'-bipyridine and 1,10-phenanthroline have been shown to be useful as photophysical and chemical probes of DNA in view of their relevance to various biochemical and biomedical application [13-19]. A wide range of metal complexes are already in clinical use [20-22]. However, their mechanisms of action are still unknown.

In the present paper we have synthesized binucleating hydrazone based ligands possessing both neutral as well as anionic donor chelating sites, one site involving an amide and phenolate and the other involving carbonyl and phenolate functionalities which can provide dissimilar environment to the metal ions. The present binucleating ligands have the potential to bind to metal ion through imine nitrogen and phenolate

*Corresponding author.
Email: ranbahadur-appchem@msubaroda.ac.in

oxygen in one side and ketonic oxygen and phenolic oxygen in another side. Such binding are likely to leave some potential donor atom free and this donor atom enhance the biological activity. It was thus felt that the study of the interaction of metal ions with above derivatives would be useful in understanding the effect of free atom on biological activity. Antibacterial activity of these ligands and complexes has been examined against *S. aureus, B. megaterium* (gram positive) and *S. typhi, S. marsescens, P. vulgaris* (gram negative) strains.

2. Materials and methods

2.1 Chemicals:

Nicotinoyl hydrazine and isonicotinoyl hydrazine were prepared from their ethyl esters by condensation with hydrazine [23]. Luria agar (Himedia), acetic anhydride (Allied), 2,2'-bipyridine and hydrazine hydrate (Qualigens), resorcinol, anhydrous zinc chloride, ethyl-3-pyridine carboxylate, ethyl-4-pyridine carboxylate, 2,2'-bipyridine, 1,10-phenanthroline. H_2O, cupric acetate monohydrate, DMSO and DMF procured from Marck were of A. R. grade and were used as received without further purification. 1-(5-Acetyl-2,4-dihydroxy-phenyl)-ethanone (DAR) was in our laboratory from resorcinol by using Fries rearrangement [24].

Preparation of the ligands

Preparation ligand, N-nicotinoyl-N'-[1-(5-acetyl-2,4-dihydroxy-phenyl)-ethylidene]-hydrazine, (H_2drNZ):

To a 30 ml methanolic solution of (0.6467 g, 3.33 mmol) of 1-(5-acetyl-2,4-dihydroxy-phenyl)-ethanone (DAR), 20 ml methanolic solution of (0.4612 g, 3.36 mmol) nictonyl hydrazine was added. The reaction mixture was allowed to reflux for 5 hours with constant stirring. A creamy white solid separated on cooling, was filtered, washed thoroughly with 30 ml methanol and dried at 50 – 60 ºC (**Figure 1**). Yield 73% (0.7623 g), m.p. 268 – 270 ˚C. Elemental analysis calculated for molecular formula $C_{16}H_{15}N_3O_4$ (MW = 313): C 61.34, H 4.79, N 13.42; found C 61.94, H 4.56, N 13.50. IR (KBr, cm^{-1}) 3650, 3404, 3058, 1676, 1639, **(S8).** ^{1}H NMR (DMSO – d6), (δ): 2.503 (s, 3H (CH_3)); 2.526 (s, 3H (CH_3)); 6.380 (s, 1H (ArH)); 7.572 (dd, 1H (PyH)); 8.127 (s, 1H (ArH); 8.266 (m, 1H (PyH); 8.295 (d, 1H (PyH); 9.082 (s, 1H (PyH); 11.617 (s, H (NH)) 12.634 (s, H (OH)); 14.441 (s, H (OH));. ^{13}C (DMSO – d6), δ): 14.63 (CH_3); 27.46 (CH_3); 104.26 (Ar); 113.12 (Ar)); 113.71 (Ar); 124.00 (Py); 134.07 (Py); 136.45 (Ar); 149.45 (Py) 152.94 (Py); 158.70 (Py); 163.43 (CONH); 164.79 (C-OH); 166.33 (C-OH); 170.45 (C=N); 203.31 (C=O); **(S1-S3)**.

Ligand, N-isonicotinoyl-N'-[1-(5-acetyl-2,4-dihydroxy-phenyl)-ethylidene]-hydrazine (H_2drINZ): was prepared by similar method using appropriate quantities of 1-(5-Acetyl-2,4-dihydroxy-phenyl)-ethanone and isonicotinoyl hydrazine. Yield 69% (0.7173), m.p. ˃300˚C. Elemental analysis calculated for molecular formula $C_{16}H_{15}N_3O_4$ (MW = 313): C 61.34, H 4.79, N 13.42; found C 61.88, H 4.65, N 13.01. IR (KBr, cm^{-1}) 3650, 3448, 3125, 1678, 1643, (**S11**). NMR (DMSO – d6), (δ): 2.564 (s, 3H (CH_3)); 2.666 (s, 3H (CH_3)); 6.385 (s, 1H (ArH)); 7.847 (d, 2H (PyH)); 8.146 (s, 1H (ArH); 8.804 (d, 2H (PyH); 11.660 (s, H (NH)) 12.627 (s, H (OH)); 14.357 (s, H (OH));. ^{1}H NMR (DMSO – d6), (δ): 11.660 (s, H (amide exchangeable NH)) 12.627 (s, H (phenolic exchangeable OH)); 14.357 (s, H (phenolic exchangeable OH));. ^{13}C (DMSO – d6), δ): 14.72 (CH_3); 27.47 (CH_3); 104.26 (Ar); 113.05 (Ar)); 113.73 (Ar); 122.50 (Py); 134.21 (Ar); 140.40 (Py); 150.66 (Py) 159.51 (CONH); 163.44 (C-OH); 164.86 (C-OH); 166.32 (C=N); 203.29 (C=O);.); (**S4-S7**).

Preparation of the complexes

Preparation of complex, [Cu_2(bip)(drNZ)Ac_2] (1a)

Binucleating ligand, H_2drNZ (0.313 g, 1.0 mmol) was suspended in 20 ml methanol in a flask equipped with a water condenser and a magnetic stirrer. Copper acetate monohydrate (0.1996 g, 1.0 mmol) dissolved in 10 ml of methanol added into the ligand solution. The reaction mixture was allowed to reflux for 1 hour. Separately $[Cubipy]^{2+}$ complex was prepared by adding 20 ml methanolic solution of (0.1561g, 1.0 mmol) 2,2'-bipyridine to a solution of (0.1996 g, 1.0 mmol) copper acetate monohydrate with constant stirring. This solution containing $[Cu(bipy)]^{2+}$ was added to the above refluxing solution over 30 minutes. The reaction mixture was allowed to reflux for 5 hours, at the end of which brownish coloured microcrystalline compound separated. The reaction mixture was cooled and the solid obtained was washed thoroughly with 20 ml methanol in 5-6 portions and dried in air at 60 – 70 ºC.

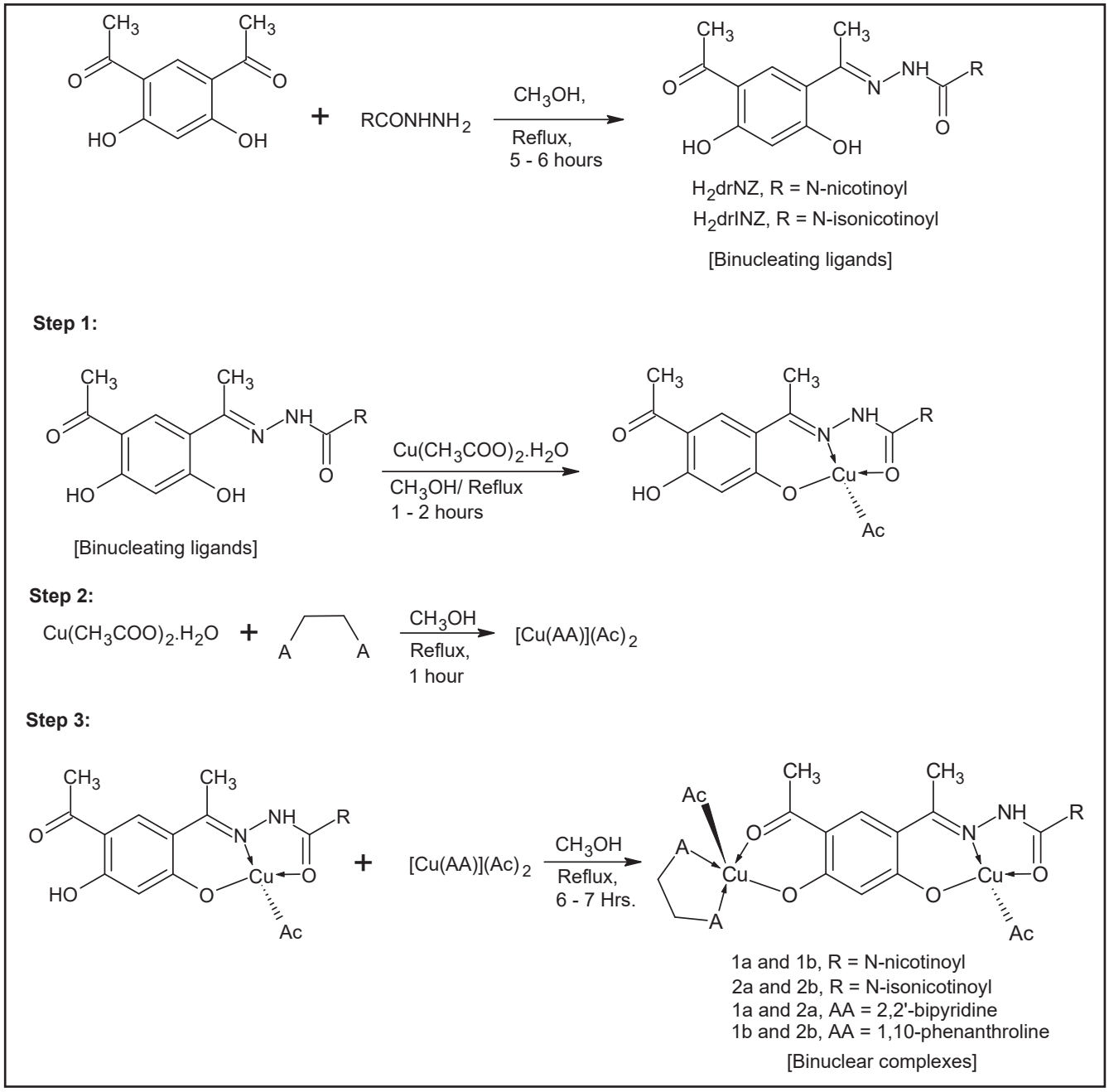

Figure 1 – Synthesis of ligands and complexes.

Complexes (**1b** and **2a** – **2b**) were synthesized by using a similar procedure and equivalent amounts of binucleating ligands, H_2drNZ and H_2drINZ, copper acetate monohydrate and respective secondary ligands, 2,2'-bipyridine or 1,10-phenanthroline (**Figure 1**).

Physical measurements

Composition of products was determined by elemental analysis on Perkin Elamer Model-2400 CHN/S analyzer. ^{1}H NMR and ^{13}C NMR of the ligands were recorded on Brucker AVCN 400 MHZ instrument. Electronic spectra of the complexes in UV-Vis region were recorded in methanolic solutions using Perkin Elmer Lambda 35 UV – Vis spectrometer. Infrared spectra (as KBr pellets) were recorded on Perkin Elamer FT-IR spectrometer model, spectrum RXI. The ESI-MS spectra of the complexes 1a and 2a in acetonitrile solvent were recorded on THERMO Finigan LCQ

Advantage max ion trap mass spectrometer. Magnetic susceptibility of the complexes at room temperature was measured in the powder form by the Faraday method at magnetic field of 0.8 Tesla. Pascal corrections for ligands and counter ions have been incorporated. Magnetic moments were calculated from Eq. 1:

$$\mu_{eff} = 2.808 (\chi_M T \times 10^{-6} / 2)^{1/2} \quad (1)$$

Antibacterial activity test

As a preliminary screening for antibacterial activity, the binucleating ligands and complexes in dimethylsulfoxide (DMSO) were tested against the gram (+) ve bacteria *S. aureus*, *B. megaterium* and gram (-) ve bacteria *S. typhi*, *S. marsescens* and *P. vulgaris* by well agar diffusion method in vitro. The liquid medium in which the bacterial cultures were to be grown was autoclaved for 15 minutes at 121ºC and at 15-psi pressure before inoculation. The bacteria were simultaneously cultured in Luria broth for 24 hours at 37 ºC in an incubator. Luria agar was poured into plates and allowed to solidify. The bacterial cultures were spread plated on to the solidified agar plates. The stock solutions of the compounds were prepared by dissolving 5 mg/ml of each compound in DMSO. 100 µl of the test compounds (DMSO solutions) were added to each well made with the help of 8 mm diameter borer on agar plates in sterile conditions. The zone of inhibition around the well was measured in millimeters after 24 hours incubation at 37 ºC. DMSO was used as control and ampicillin, tetracycline, gentamicin and chloroamphenicol as standard drugs. All tests were repeated thrice and average of the values were taken as the final results.

Results and discussion

The binucleating ligands were obtained in appreciably good yield. Structure of the ligands proved by elemental analysis, FTIR, ^{1}H NMR and ^{13}C NMR analysis. The melting points and analytical data of the ligands are given with synthesis. The analytical data is agreeable with the calculated values.

The elemental analysis of binuclear complexes agrees with the values calculated using the suggested molecular formulae (**Table 1**).

Electronic spectra

The electronic spectra of the complexes in methanolic solutions exhibit a weak broad band in the region 605 – 640 nm and four intense bands between 232 to 397 nm. The bands around 236 and 320 nm can be attributed to interaligand $\pi \rightarrow \pi^*$ transition in the pyridyl ring and the imine function of the binucleating hydrozone and secondary ligands. The band around 390 nm indicate metal → ligand charge transfer in the complexes. The band in the region 605 – 640 nm region corresponds to the ligand field transitions and can be assigned to $d_{xy} \rightarrow d_{x2-y2}$, $d_{yz} \rightarrow d_{x2-y2}$, $d_{xz} \rightarrow d_{x2-y2}$ and $d_{z2} \rightarrow d_{x2-y2}$ transitions in square and elongated square based pyramidal geometry resulting due to coordination of acetate. (**Table 2**).

Table 1 – Preparative yields, analytical[a] and magnetic moment for binuclear complexes

Sr. No.	Complexes	Yield (%)	C (%)	H (%)	N (%)	Magnetic moment (BM)
1a	$[Cu_2(bip)(drNZ)Ac_2]$ $C_{30}H_{27}N_5O_8Cu_2$	56	50.68 (50.55)	3.79 (3.79)	9.88 (9.83)	1.88
1b	$[Cu_2(phen)(drNZ)Ac_2]$ $C_{32}H_{27}N_5O_8Cu_2$	53	52.76 (52.16)	3.35 (3.66)	9.80 (9.51)	1.89
2a	$[Cu_2(bip)(drINZ)Ac_2]$ $C_{30}H_{27}N_5O_8Cu_2$	43	50.27 (50.55)	3.83 (3.79)	10.00 (9.83)	1.81
2b	$[Cu_2(phen)(drINZ)Ac_2]$ $C_{32}H_{27}N_5O_8Cu_2$	54	52.89 (52.16)	3.71 (3.66)	9.58 (9.51)	1.97

[a]**Calculated values are given in the parentheses.**

Table 2 – Energies of the band positions and IR absorptions of binuclear complexes

Comp. No.	Uv-Visible band positions λ_{max}(nm) in methanolic solution	ν(-NH) (cm^{-1})	aromatic stretching ν(-C-H) (cm^{-1})	ν(>C=O) (cm^{-1})	ν(>C=N) (cm^{-1})	ν(-COO^-) (cm^{-1})
1a	233, 269, 359, 380, 640	3448	3065	1638	1592	1369
1b	232, 254, 340, 620	3435	3060	1638	1540	1369
2a	232, 290, 325, 391, 610	3433	3055	1638	1575	1362
2b	260, 280, 361, 605	3434	3094	1628	1586	1370

IR Spectra

The IR spectra of the complexes in the region 400 – 4000cm^{-1} are very rich. The most important IR absorption frequencies among these are as follows.

Absorption due to the stretching of the amide N-H occurs between 3404 – 3448 cm^{-1} in the free ligand and in the complexes. In the free ligands, the band at 1678 cm^{-1} is due to >C=O stretching of the amide or ketonic group. On complexation this ν(>C=O) shifts to lower frequencies, i.e. 1628 – 1638 cm^{-1}. In the ligands, imine band ν >C=N is observed between 1639 – 1643 cm^{-1}. These are observed at lower energies in complexes i.e. between 1540 – 1592 cm^{-1}. The shift in >C=O (amide or ketonic) and >C=N (imine) towards lower energy in the complexes compared to the ligands and almost

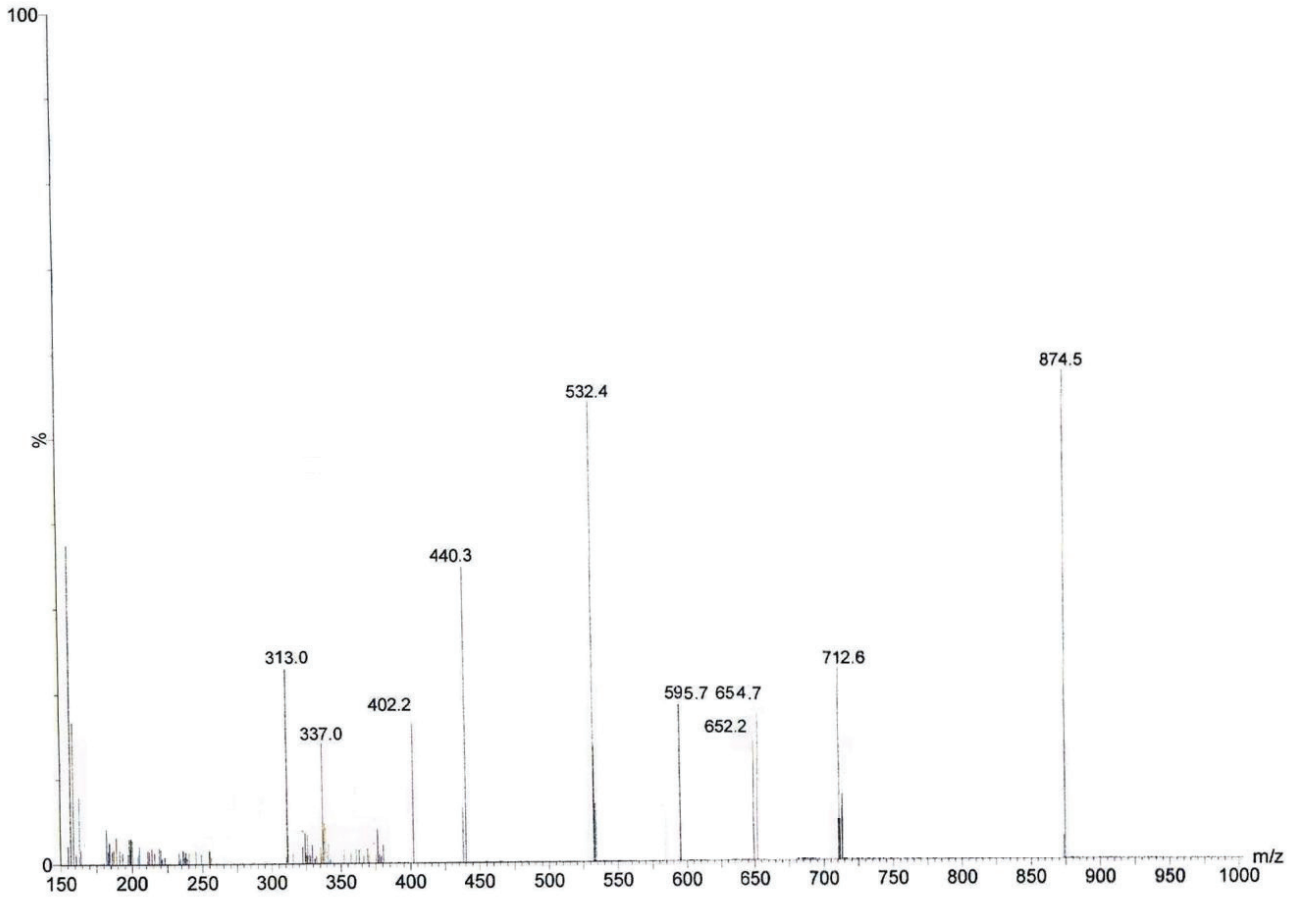

Figure 2 – ESI-Ms spectra of the complex, [Cu_2(bipy)(drNZ)Ac_2].

Table 3 – Antibacterial activities of ligands and complexes (Zone formation in mm).

Compounds	S. aureus	B. megaterium	S. marsescens	P. vulgaris	S. typhi
H_2drNZ	16	12	14	-	-
1a	-	-	-	-	-
1b	-	-	-	-	-
H_2drINZ	-	-	15	16	-
2a	-	-	13	-	-
2b	-	-	12	-	-

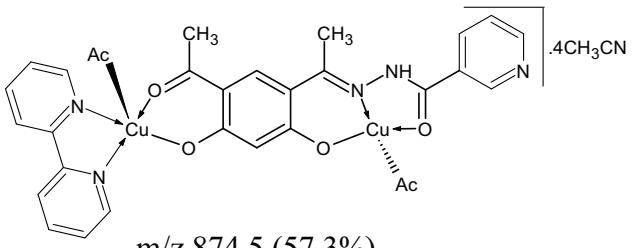

m/z 874.5 (57.3%)

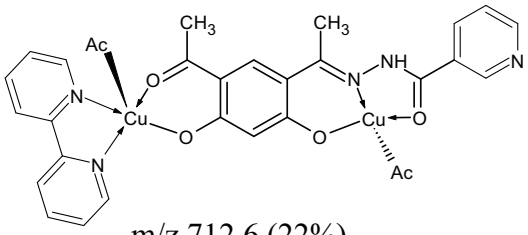

m/z 712.6 (22%)

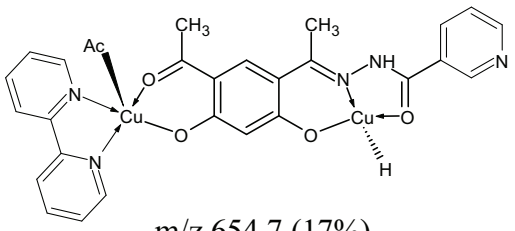

m/z 654.7 (17%)

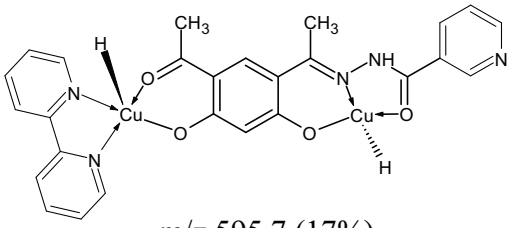

m/z 595.7 (17%)

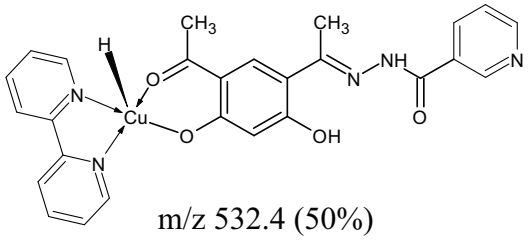

m/z 532.4 (50%)

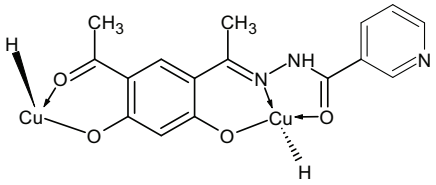

m/z 440.3 (31%)

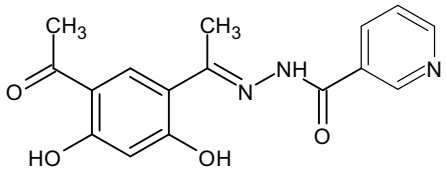

m/z 313.0 (21%)

Figure 3 – Possible structure of $[Cu_2(bipy)(drNZ)Ac_2]$ and the corresponding fragments in ESI-Ms.

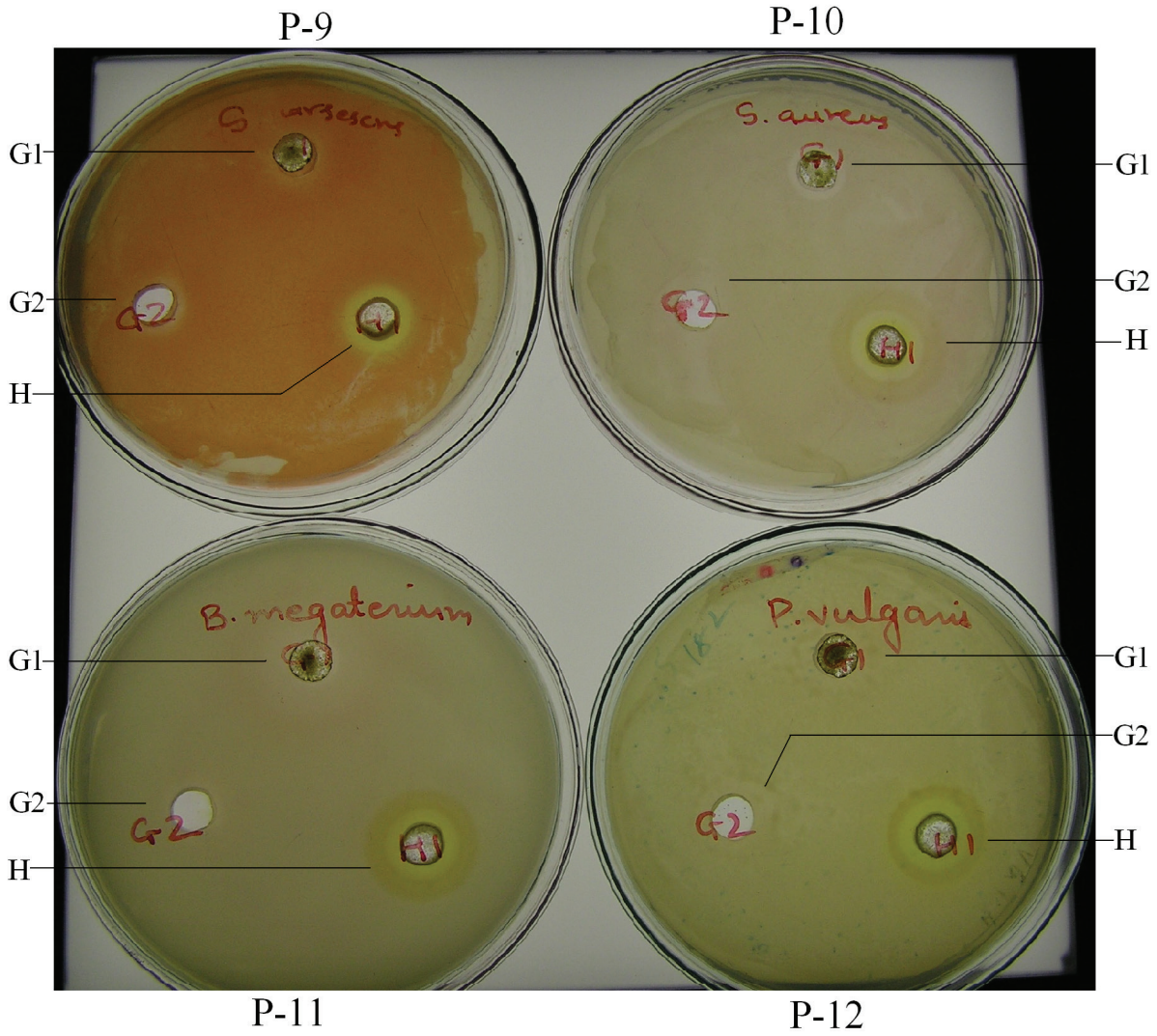

Figure 4 – Inhibition of bacteria by ligand, H_2drNZ (H) and binuclear complexes [Cu_2(bipy)(drNZ)Ac_2] (G1) and [Cu_2(phen)(drNZ)Ac_2] (G2), Plate-9: B. megaterium, plate-10: S. marsescens, plate-11: P. vulgaris, and plate-12: S. aureus.

unaffected amide N-H stretching frequency indicate that the imine nitrogen and amide or ketonic oxygen are involved in coordination with metal ion where as amide nitrogen does not take part in the binding with metal ion.

The absorption due to $–COO^-$ (carboxylate anion) ions were observed between 1362 – 1370 cm^{-1} region. It confirmed that the acetate ions are inside the coordination sphere and directly attached to the central metal ion [25]. In all the complexes characteristic bands appeared between 3030 – 3125 cm^{-1} due to aromatic C-H stretching, (**Table 2, S9, S10, S12 and S13**).

Magnetic properties

Effective magnetic moment values of the complexes at room temperature range between 1.81 – 1.97 BM per copper (II) ion. These values of magnetic moment indicate weakly ferromagnetic interaction between the two metal centers. (T**able** 1).

Mass spectra

The ESI-Ms spectrum of the complex, [Cu_2(bipy)(drNZ)Ac_2] was recorded in acetonitrile solution (**Figure 2**). As acetonitrile has strong coordinating tendency, it associated with complex and exhibited

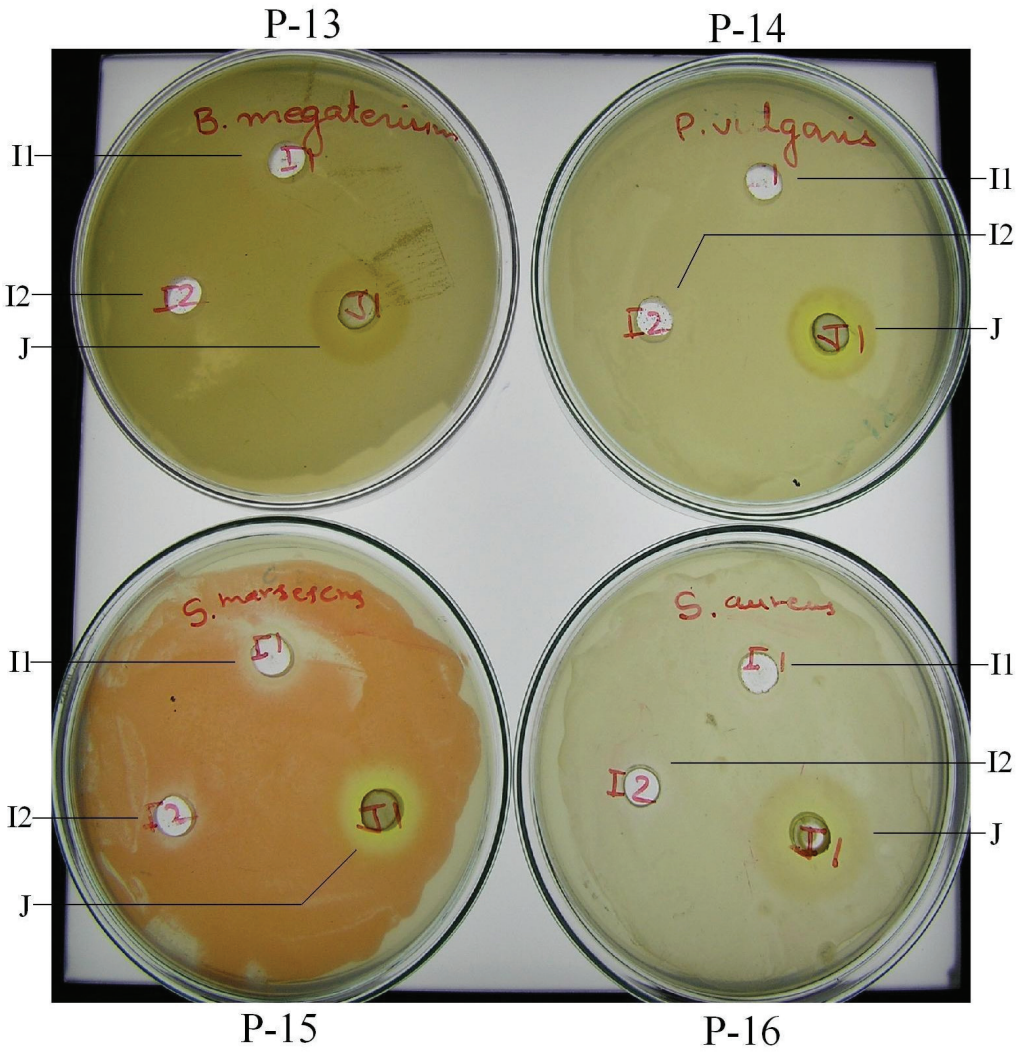

Figure 5 – Inhibition of bacteria by ligand, H_2drINZ (J) and binuclear complexes [Cu_2(bipy)(drINZ)Ac_2] (I1) and [Cu_2(phen)(drINZ)Ac_2] (I2), plate-13: B. megaterium, plate-14: P. vulgaris, plate-15: S. marsescens and plate-16: S. aureus.

parent ion peak at m/z 874.5 with 57.3% relative abundance. Peak corresponding to complex is observed at m/z 712.6 with 22% relative abundance. Consequently, peak corresponding to loss of acetate ions from molecular formulae are observed at 653 and 594 with 17% relative abundance.

Other important fragments $[Cu(drNZ)(bip)]^+$ is observed at m/z = 532.4 (54.3%) which is formed due to loss of a Cu ion from binuclear complex. $[Cu_2(drNZ)]^+$ is appeared at m/z 440.3 with 35% relative abundance. Peak corresponding to binucleating ligand, H_2drNZ is appeared at m/z 313 with 21% relative abundance. The presence of these peaks supported the formation of binuclear complexes. (**Figure 3**).

Biological activity

Biological activity of the ligands and their respective copper complexes were examined against *Staphylococcus aureus* and *Bacillus megaterium* which are gram positive organisms and against *Serratia marsescens*, *Proteus vulgaris*, and *Salmonella typhi* which are gram negative organisms. Biological activity of the above mentioned organisms was also carried out against Cu-acetate monohydrate and

standard antibiotics like ampicillin, chloramphenicol, kanamycin, streptomycin and tetracycline. (**Table** 3, **Figure 4, 5**)

Ligand, H_2drNZ showed biological activity against *Staphylococcus aureus*, *Bacillus megaterium* and *Serratia marsescens* but its complexes (**1a** and **1b**) did not show any biological activity. Ligand, H_2drINZ and its complexes (2a and 2b) showed biological activity only against *Serratia marsescens.* Ligand, H_2drINZ and its complexes (**2a** and **2b**) did not show any biological activity against *Staphylococcus aureus*, *Bacillus megaterium*, *Proteus vulgaris*, and *Salmonella typhi*.

Generally, stating the ligands, H_2drNZ, H_2drINZ and their complexes showed poor or no biological activity against gram positive as well as against gram negative organisms. It has been observed that the ligand molecules are more active than corresponding complexes, in the present studied in fact the copper (II) ion has an inhibitory effect.

Conclusions

We described here the synthesis of binucleating ligands and its corresponding binuclear copper (II) complexes. The characterization of the complexes was achieved through elemental analysis, IR and ESI-MS. Antibacterial studies of binucleating ligands and complexes exhibit that ligands are more effective against the bacterial growth.

Acknowledgement:

Thanks are due the Department of Science and Technology, New Delhi, India for their financial support, Director, SAIF, Central Drug Research Institute, Lucknow for providing ESI-Ms spectra of the complex, Head, Department of Chemistry, Faculty of Science, The Maharaja Sayajirao University of Baroda for recording NMR of ligands, and Head, Department of Microbiology and Biotechnology Centre, Faculty of Science, The Maharaja Sayajirao University of Baroda, Vadodara for screening antibacterial activity.

References

1. S. Rollas, N. Gulerman, H. Erdeniz, Synthesis and antimicrobial activity of some new hydrazones of 4-fluorobenzoic acid hydrazide and 3-acetyl-2,5-disubstituted-1,3,4-oxadiazolines, *Farmaco,* 57(2), 171, **2002**.
2. Ş.G. Küçükgüzel, S. Rollas, I. Küçükgüzel, M. Kiraz, Synthesis and Antimycobacterial activity of some coupling products from 4-aminobenzoic acid hydrazones, *Eur. J. Med. Chem.,* 34, 1093, **1999**.
3. Ş.G. Küçükgüzel, E. E. Oruç, S. Rollas, F. Şahin, A. Özbek, Synthesis, Characterization and biological activity of novel 4-thiazolidinones, 1,3,4-oxadiazoles and some related compounds, *Eur. J. Med. Chem.,* 37, 197, **2002**.
4. K. B. Kaymakçıoğlu, E. E. Oruç, S. Unsalan, F. Kandemirli, N. Shvets, S. Rollas, D. Anatholy, Synthesis and characterization of novel hydrazide–hydrazones and the study of their structure–antituberculosis activity, *Eur. J. Med. Chem,* 41 (11), 1253, **2006**.
5. S. Rollas, Ş.G. Küçükgüzel, Biological Activities of Hydrazone Derivatives. *Molecules,* 12, 1910, **2007.**
6. G. Wu, G. Wang, X. Fu, L Zhu, Synthesis, Crystal Structure, Stacking Effect and Antibacterial Studies of a Novel Quaternary Copper (II) Complex with Quinolone, *Molecules,* 8, 287, **2003**.
7. D. Jayaraju, A. K. Kondapi, Anti-cancer copper salicylaldoxime complex inhibits topoisomerase II catalytic activity, *Current Science*, 81(7), 787, **2001**.
8. K. G. Daniel, P. Gupta, R. Hope Harbach, W. C. Guida, Q. P. Dou, Organic copper complexes as a new class of proteasome inhibitors and apoptosis inducers in human cancer cells, *Biochemical Pharmacology,* 67, 1139, **2004**.
9. E. K. Efthimiadou, H. Thomadaki, Y. Sanakis, C. P. Raptopoulou, N. Katsaros, A. Scorilas, A. Karaliota, G. Psomas, Structure and Biological Properties of the Copper (II) Complex with the Quinolone Antibacterial Drug N-Propyl-Norfloxacin and 2,2'-Bipyridine, *J. Inorg. Biochem.*, 101, 64, **2007**.
10. G. Cerchiaro, A. M. da Costa Ferreira, Oxindoles and Copper Complexes with Oxindole-Derivatives as Potential Pharmacological Agents, *J. Braz. Chem. Soc.,* 17(8), 1473, **2006**.
11. J. P. Henichart, M. J. Waring, J. F. Riou, W. A. Denny, C. Bailly, Copper-dependent oxidative and topoisomerase II-mediated DNA cleavage by a netropsin/4'-(9-acridinylamino) methanesulfon-m-anisidide combilexin, *Molecular Pharmacology,* 51(3), 448, **1997**.
12. M. B. Vasudevachari, A. Antony, Effect of cupric-isonicotinic acid hydrazide complex on normal and avian myeloblastosis virus infected cells cultivated in vitro*, J. of Bioscience*, 7 (1), 33, 1**985**.

13. M. Geraghty, J. F. Cronin, M. Devereux, M. McCann, Synthesis and antimicrobial activity of copper (II) and manganese (II) alpha,omega-dicarboxylate complexes, *Biometals*, 13 (1), 1, **2000**.

14. D. R. McMillin, K. M. McNett, Photo processes of copper complexes that bind to DNA, *Chem. Rev.*, 98, 1201, **1998**.

15. K. E. Erkkila, D. T. Odom, J. K. Barton, Recognition and reaction of metallointercalators with DNA, *Chem. Rev.,* 99, 2777, **1999**.

16. H. Sigel, "Metal Ions in Biological Systems" *(Eds),* Vol. 1-37, Marcel Dekker, New York.

17. C. Dendrinou-Samara, G. Psomas, K. Christophorou, V. Tangoulis, V. P. Raptopoulou, A. Terzis, D. P. Kessissoglou, Structurally Diverse Copper (II) Herbicide Complexes: Mono- and Bi-nuclear Neutral Cationic Complexes, *Dalton Trans.*, 3737, **1996**.

18. G. Psomas, C. Dendrinou-Samara, P. Philippakopoulos, V. Tangoulis, C. P. Raptopoulou, E. Samaras, D. P. Kessissoglou, Cu^{II}-Herbicide Complexes: Structure and Bioactivity, *Inorg. Chim. Acta*, 272, 24, **1998**.

19. G. Psomas, A. Tarushi, E. K. Efthimiadou, Y. Sanakis, C. P. Raptopoulou, N. Katsaros, Synthesis, structure and biological activity of copper (II) complexes with oxolinic acid, *J. Inorg. Biochem.,* 100, 1764, **2006**.

20. L. J. Ming, J. D. Epperson, Metal binding and structure-activity relationship of the metalloantibiotic peptide bacitracin, *Inorg. Biochem.,* 91(1), 46, **2002**.

21. F. Kratz, M. T. Schutte, Anticancer Metal-Complexes and Tumor Targeting strategies, *Cancer J.,* 11(4), 176, **1998**.

22. [22]. S. J. Berners-Price, P. J. Sadler, Coordination chemistry of metallodrugs: insights from NMR spectroscopy, *Coord. Chem. Rev.,* 151, 1, **1996**.

23. B. S. Furniss, A. J. Hannaford, V. Rogers, P. W. G. Smith, A. R. Tatchell, "Vogel's Textbook of Practical Organic Chemistry" *4th ed, ELBS-Longman,* **1978.**

24. A. S. R. Anjaneyulu, A. V. Rama Prasad, D. Siva Kumar Reddy, *Curr. Sci.,* 7(48), 300, **1979**.

25. K, Nakamato, *"Infrared and Raman Spectra of Inorganic and Coordination Compounds"* 5th Edition, **1997** John Wiley and Sons, New York.

Statement about the ownership and other particulars about newspapers
JOURNAL OF THE MAHARAJA SAYAJIRAO UNIVERSITY OF BARODA

(To be published in the first issue every year after the last day of February)

FORM IV

(See Rule 8)

1.	Place of the Publication	:	The The Maharaja Sayajirao University of Baroda M.S. University of Baroda, Vadodara - 390 002.
2.	Periodicity of its Publication	:	Science & Technology at any time during the year.
3.	Printer's Name	:	Shri Jatin H. Somani
	Nationality	:	Indian
	Address	:	Offg. Manager, The M.S.University of Baroda Press, (Sadhana Press), Vadodara - 390 001.
4.	Publisher's Name	:	Prof. P. K. Jha
	Nationality	:	Indian
	Address	:	The M. S. University of Baroda, Vadodara - 390 002.
5.	Editor's Name	:	Prof. P. K. Jha
	Nationality	:	Indian
	Address	:	The M. S. University of Baroda, Vadodara - 390 002.
6.	Names & Addresses of Individuals who own the newspaper and partners or shareholders holding more than one percent of the total capital	:	The M. S. University of Broda, Vadodara - 390 002.

I, C. N. Murthy declare that the particulars given above are true to the best of my knowledge and belief.

Prof. P. K. Jha

JOURNAL OF THE MAHARAJA SAYAJIRAO UNIVERSITY OF BARODA

The Journal is mainly intended to publish original research papers contributed by the teachers and research scholars of the M.S. University of Baroda.

One volume of the Journal is issued every year in three parts. These parts are devoted respectively to topics relating to Humanities, Social Science, Science & Technology, Medicine. All manuscripts, books and publications for review should be addressed to :

The Editor (Science & Technology),
Journal of the M.S. University of Baroda,
A.I.C.S. Training Centre,
Baroda - 390 002.

email: editor.msujst@gmail.com

Contributors are requested to submit manuscripts, by email attachment which should be typed with double spacing and on one side of the paper only. Authors are advised to retain a copy of the paper that they send for publication as the Editors cannot accept responsibility for any loss.

Authors of papers printed in the Journal are entitled to one copy of the issue free of charge.

ADVERTISEMENT

All advertising matters should be send so as to reach the office of the Journal a month before the publication of the Journal. Further information on rates and space can be had on writing to **editor.msujst@gmail.com.**

Printed at : The M.S. University of Baroda Press (Sadhana Press), Palace Road, Vadodara - 390 001.

THE MAHARAJA SAYAJIRAO UNIVERSITY OF BARODA

सत्यं शिवं सुन्दरम्

Estd. 1949

"The full-blown lotus growing out of the lake symbolises the emergence of the mind and its triumph over matter. The flame rising from the center of the lotus is the flame of the human knowledge, spreading light and learning for the coming generations. The motto inscribed below the lotus defines the purpose and existence of life which is love of beauty, goodness and intellectual curiosity."

महाराजा सयाजीराव विश्वविद्यालय गीत

अमे वडोदराना विद्यापीठनां सपनां सारवनारा
अमे ज्योत जलावी सृष्टि नवली सहसा सर्जनहारा.

अमे गगनकुसुम कर धरनारा
अमे मगन मगन थई फरनारा
अगनबाथ अमे भरनारा
अमे दैन्यतिमिरने हरनारा.

श्री सयाजी विद्यापीठना ज्ञानदीपने धरनारा
सत्यं शिवं सुन्दरम् नो मंत्र अनंतर भणनारा.

Printed at: The Maharaja Sayajirao University of Baroda Press (Sadhana Press), Vadodara-390 001